FLIGHT ENVELOPE PROTECTION USING FLAP HINGE MOMENT MEASUREMENT

BY

PHILLIP J. ANSELL

THESIS

Submitted in partial fulfillment of the requirements
for the degree of Master of Science in Aerospace Engineering
in the Graduate College of the
University of Illinois at Urbana-Champaign, 2010

Urbana, Illinois

Adviser:

Professor Michael B. Bragg

Abstract

An experimental investigation of the sensitivity of flap hinge moment to airfoil surface contamination was conducted at the University of Illinois at Urbana-Champaign Aerodynamics Research Lab. Tests were conducted on two airfoil models, an NACA 3415 and an NACA 23012, at Reynolds numbers of 1.8×10^6 and 1.0×10^6. The effects of six different simulated contamination configurations on the performance characteristics of both airfoils were tested. These configurations consisted of glaze ice, rime ice, two severities of distributed leading-edge roughness, three-dimensional leading-edge damage, and three-dimensional upper-surface damage. Additionally, the effects of flap deflection and trim tab deflection on the unsteady hinge moment were studied.

Results from this study found that large increases in $C_{h,StDev}$ often occurred at the same angle of attack as $C_{l,max}$. By correlating regions of separated flow observed in C_p distributions and fluorescent-oil flow visualizations to $C_{h,StDev}$ at discrete angles of attack, it was determined that regions of boundary-layer separation were the primary driver for large increases in unsteadiness in the hinge moment. It was also found that the unsteady hinge moment had negligible dependence on trim tab deflection. The response of $C_{h,StDev}$ was dependent on the stalling characteristics of the airfoil model.

Of all of the contamination configurations tested, the two simulated ice cases had the largest effect on the performance of the airfoils. For the distributed leading-edge roughness cases, the larger roughness elements had a larger effect on the performance than the smaller roughness elements, but the $C_{h,StDev}$ response of both roughness cases were comparable. While the 3D simulated damage cases did not significantly affect the lifting characteristics of either model, the magnitude of the $C_{h,StDev}$ response of the 3D simulated damage case was comparable to the 2D contamination cases. Additionally, the large increase in $C_{h,StDev}$ occurred prior to stall due to localized regions of separated flow that resulted from the simulated damage.

Acknowledgements

First and foremost, I would like to thank my advisor, Professor Michael B. Bragg for providing me the opportunity to work and study in his research group. His guidance over the duration of this project has been invaluable. Many thanks are also due to Dr. Michael F. Kerho for his assistance and patience throughout the course of this project. His extensive knowledge base and willingness to answer my multitude of questions has helped me get the most out of my research experience.

As this work was funded through an STTR, I would like to thank Mark Davis and the people at NASA Dryden Flight Research Center. Finally, I would like to thank my parents, my brother, and my sister for their unconditional love. The strength, support, and encouragement of my family have helped me get through the toughest of times.

Table of Contents

List of Tables

List of Figures

Nomenclature

A	Axial force from balance
A_{ss}	Wind tunnel inlet settling section area
A_{ts}	Wind tunnel test section area
b	Model span
b	Hinge moment intercept
c	Model chord
c_f	Model flap chord
C	Test-section area
C_d	Drag coefficient
C_h	Hinge moment coefficient
$\overline{C}_h$	Hinge moment coefficient sum over total number of samples
$C_{h,StDev}$	Standard deviation of the hinge moment coefficient sample
C_l	Lift coefficient
$C_{l,max}$	Maximum lift coefficient
C_m	Quarter-chord pitching moment coefficient
C_p	Pressure coefficient
D	Drag
D'	Drag per unit span
d_h	Flap hinge moment arm
F_A	Axial force
$F_{A'}$	Axial force per unit span
F_N	Normal force
$F_{N'}$	Normal force per unit span
F_h	Load applied to hinge moment balance
h	Test-section height
H	Hinge moment

H'	Hinge moment per unit span
$(k/c)_{max}$	Maximum feature height, non-dimensionalized by the chord
K_1	Body-shape factor
L	Lift
L'	Lift per unit span
m	Hinge moment conversion slope
M	Pitching moment
$M_{c/4}$	Quarter-chord pitching moment
$M'_{c/4}$	Quarter-chord pitching moment per unit span
n	Number of model pressure taps
n_{flap}	Number of flap pressure taps
n_{rake}	Number of wake rake total pressure measurements
N	Number of samples
N	Normal force from balance
P	Characteristic static pressure
$P_{0,\infty}$	Total pressure in the freestream
$P_{0,w}$	Total pressure in the wake
P_{amb}	Ambient air pressure
P_s	Static pressure at model surface
P_{ss}	Static pressure at wind tunnel inlet settling section
P_{ts}	Static pressure in wind tunnel test section
q_∞	Dynamic pressure
R	Ideal gas constant for air
R	Uncertainty of a general result
Re	Reynolds number based on chord length ($\rho U_\infty c/\mu$)
RR_A	Axial force range ratio
RR_M	Pitching moment range ratio
RR_N	Normal force range ratio
S	Projected model area
S_f	Projected flap area
t	Model thickness

T_{amb}	Ambient air temperature
U	Uncertainty
U	Characteristic velocity
U_{ss}	Inlet settling section velocity
U_{ts}	Test section velocity
U_{∞}	Freestream velocity
V_A	Scaled axial force voltage
V_M	Scaled pitching moment voltage
V_N	Scaled normal force voltage
V_{0A}	Tared axial force voltage
V_{0M}	Tared pitching moment voltage
V_{0N}	Tared normal force voltage
V_h	Hinge moment voltage
W	Test-section width
x	Model coordinate in chordwise direction
x/c	Coordinate parallel to the airfoil model chordline, non-dimensionalized by the chord
x_{offset}	Chordwise displacement of model from balance center
y	Model coordinate in normal direction
y_{offset}	Normal displacement of model from balance center

Greek Symbols

α	Model angle of attack
α_{stall}	Angle of attack of maximum lift
δ_f	Angle of flap deflection
δ_t	Angle of trim tab deflection
ΔP	$P_{ss} - P_{ts}$
ε	Total velocity increment
ε_{sb}	Solid-blockage velocity increment

ε_{wb}	Wake-blockage velocity increment
ρ	Air density
ρ_{amb}	Ambient air density
σ	Wall correction simplifying parameter
μ	Dynamic viscosity

Acronyms

A/D	Analog to Digital
ESP	Electronically Scanned Pressure
GPIB	General Purpose Interface Bus
NACA	National Advisory Committee on Aeronautics
NASA	National Aeronautics ans Space Administration
NTSB	National Transportation Safety Board
PCU	Pressure Calibration Unit
PSI	Pressure Systems Incorporated
PSD	Power Spectral Density
RMS	Root-Mean-Square
RSS	Root-Sum-Square
SLD	Supercooled Large Droplet
UIUC	University of Illinois at Urbana-Champaign

Chapter 1

Introduction

According to the National Transportation Safety Board (NTSB) 2005 Annual Review of Aircraft Accident Data, weather conditions were cited as a cause or factor in 30.6% of all Part 121 aircraft accidents in 2005.[1] Additionally, weather conditions were cited as a cause or factor in 19% of all general aviation accidents in 2005.[2] Since environmental factors seem to play such a large role in contributing to aircraft accidents, it is important to develop methods that can prevent such accidents from occurring.

Aircraft stall causes a loss of lift over a wing, which can have undesirable effects including loss of control, spins, or a deep stall. Stall occurs when the boundary layer over a lifting body separates from that body due to the presence of a strong adverse pressure gradient. This often occurs after a certain angle of attack is exceeded. This critical angle of attack can be reduced by various forms of contamination on a lifting surface.

Contaminants can come from a variety of sources. Some of the more common contaminants that are studied in this investigation include ice accretion, accumulation of roughness from environmental debris, frost, or heavy rain, and localized damage to a wing section. The performance of a lifting surface in a fluid flow is governed by the shape of the lifting surface. As contaminants alter the geometry of a lifting surface, the performance of that lifting surface is affected, oftentimes in an undesirable fashion. These changes in performance

commonly involve a loss of lift, a reduction in stall angle of attack, increase in drag, and change in pitching moment properties. Thus, it is imperative that the effects of any present environmental contamination on the stalling characteristics of aircraft are known in order to maintain safe flight.

1.1 Effects of Contamination on Aerodynamic Characteristics

Ice accretion can occur when an aircraft flies through icing conditions, most commonly between temperatures of +2° C and -20° C, and with a sufficient amount of liquid water in the air, commonly in the form of cloud cover or precipitation.[3] The negative effects of ice accretion on a wing section are relatively well known.[4,5] For example, in Busch et al.,[6] a horn-ice accretion reduced the maximum lift of an NACA 23012 airfoil by 55% and increased its maximum drag by 400%.

When an aircraft flies at lower altitudes, it runs a greater risk of accumulating surface roughness across its lifting surfaces. Surface roughness can come from various environmental contaminants, be it dust, heavy rain, dirt, sand, or collisions with insects. As the contaminants collect on the leading edge of a wing section, the aerodynamic characteristics of that section are changed. Luers and Haines[7] state that roughness or heavy rain can reduce the maximum lift of a wing by 30% or more.

Damage to a wing surface can also change the shape of a section, leading to a change in the aerodynamic behavior of the wing. Damage to a wing can come from in-flight bird strikes, on-ground collisions, battle damage, and/or localized explosions/failures. Unlike ice accretion or roughness accumulation, damage to a wing is usually localized to one section across the span. A simulated damage study performed by Shah[8] noted that while the resulting loss of lift to a wing can be compensated by increasing angle of attack in most cases, damage to a wing can lead to reductions in controllability.

1.2 Current Stall Warning Methods

Most aircraft today are fitted with angle-of-attack sensors that are linked to stall warning systems. The stall angle of attack of a clean aircraft is determined, and the stall warning system alerts a pilot when the current angle of attack of the aircraft is approaching the critical stall angle of attack. While this system has worked well in preventing accidents, it assumes the aircraft is

free of foreign contaminants. In other words, it cannot accurately, using real-time data, take into account the reduction of stall angle of attack from surface contamination.

In order to improve stall sensing, various systems have been suggested using local flow measurement. One such example of this is Stall Warning Plus, which uses the localized turbulence intensity factor in order to identify the onset of separation.[9] Another example is the System for Onboard Lift Analysis, which uses pressure taps on the upper and lower surfaces of a wing, calculates the difference in pressure between the surfaces, and compares this difference to a calibrated quantity for a specific flight condition.[10] A disadvantage of these methods is that their monitoring is limited to the flow area covered by the sensors. Thus, it is difficult to monitor the flow integrity without an array of sensors. Additionally, most systems are only capable of identifying separation when it occurs, and cannot predict separation.

An alternative approach was first proposed by Gurbacki and Bragg.[11,12] This method uses the aerodynamic effects of flow separation, in the form of flap hinge moment measurements, to predict impending stall. Such a system would have the capability of predicting stall under clean and contaminated wing configurations, continuously monitoring all sections of a wing that have a trailing-edge flap or control surface. Implementation would use existing trailing-edge flaps and control surfaces.

1.3 Previous Work Related to Hinge Moment Stall Sensing

A limited number of previous studies have investigated the sensitivity of the hinge moment of a simple flap due to changes in the flowfield over an airfoil. One study by Trunov and Inglelman-Sundberg[13] identified the effects of premature separation due to icing on the hinge moment of a tailplane. The resulting hinge moments of the clean test case increased linearly with negative angle of attack. However, upon stall, the hinge moment sharply increased in a nonlinear fashion. This sudden increase in hinge moment was the result of flow separation across the tailplane lower (suction) surface. As the flow separated, the pressure in the region of the flap lower surface decreased, causing the flap to experience an increase in suction on its lower surface. For a test case with leading-edge ice or roughness, the nonlinear increase in hinge moment occurred at a less-negative angle of attack than the clean case.

In October of 1994, a fatal crash of an ATR-72 occurred in Roselawn, IN.[14] Upon studying the flight recorder data, it was concluded that the crash was likely the result of a

phenomena known as “aileron snatch,” which was a product of ice accretion on the wings of the aircraft. When the ice disturbs the flow over the upper surface of a wing, it is prone to separate, creating a low-pressure region over the upper surface of the aileron. This low-pressure region pulls the aileron towards the region of low pressure, causing aileron snatch. Thus, the proper controllability of the ATR-72 was compromised, causing the crash to occur. This incident led to an increase in efforts to understand the link between the aerodynamic effects of ice accretion and hinge moment.

Gurbacki and Bragg[11] studied this behavior on an NACA 23012 airfoil model with a simple flap. Time-averaged and unsteady hinge moment measurements were taken for both a clean model and a model with a simulated super-cooled large droplet (SLD) ice accretion at increasing angles of attack. The time-averaged hinge moment measurements revealed traits comparable to the Trunov and Inglelman-Sundberg results, where the hinge moment appeared to decrease linearly with increasing angle of attack of the NACA 23012 model, and sharply decrease upon separation. Like the Trunov and Inglelman-Sundberg investigation, the Gurbacki and Bragg results showed that the addition of simulated ice towards the leading edge of the NACA 23012 model decreased the angle of attack where stall occurred. This ice-induced separation then led to a decrease in the slope of the time-averaged hinge moment as well as its mean value. Additionally, Gurbacki and Bragg[11] investigated the effects of separation and ice-induced separation on the unsteady hinge moment. The clean case revealed small changes in the RMS of the hinge moment while the flow across the NACA 23012 model was still fully attached. Upon reaching stall, however, the hinge moment RMS parameter experienced a sharp, nonlinear increase in magnitude. For the iced case, steady increases in the RMS of the hinge moment were noticeable 1°-3° before the airfoil stalled. Thus, it was identified that the unsteady separated flow led to unsteady changes in the hinge moment, giving rise to the idea that unsteady hinge moment measurements could be used in order to predict premature stall.

1.4 Research Motivation

The great involvement of weather conditions and environmental effects in recent aircraft accidents indicates a continued need for a more effective performance monitoring system. While pilots may be aware of certain unfavorable environmental conditions, they may not know the full extent of the effect the conditions have on the aircraft’s aerodynamic characteristics. Thus, the

motivation behind this investigation is to improve understanding of the relationship between the stalling of a wing section and its time-dependent effects on flap hinge moment, before and after stall. This could assist in the development of a method that can be used to warn pilots when the edge of the aircraft's flight envelope is being reached under nominal or adverse conditions, aiding in the reduction of environmental-related aircraft accidents.

1.5 Objectives

Overall, the goal of this research was to improve the understanding of the prior- and post-stall effects of boundary-layer separation on flap hinge moment. Data from this investigation could be used to aid in the development of a system that uses an unsteady hinge-moment parameter to predict stall of a wing section, occurring from exceeding the clean maximum angle of attack or premature stall due to contamination of the lifting surface. This goal was accomplished through the analysis and correlation of the unsteady hinge moment measurements and the aerodynamic characteristics for multiple airfoil configurations. This research was performed in order to identify and understand:

- The relationship between trim tab deflection and unsteady hinge moment
- The effect of boundary-layer separation on steady and unsteady hinge moment
- Changes in airfoil performance parameters due to 2D spanwise simulated contaminants and localized 3D simulated damage
- The feasibility of utilizing the unsteady hinge-moment parameter for predicting stall under clean and contaminated configurations

Chapter 2

Experimental Methodology

This chapter describes the methods and facilities used during the project investigation. It provides descriptions of the test equipment and data acquisition system that were utilized during the aerodynamic testing at the University of Illinois at Urbana-Champaign (UIUC). Details are also provided about the test configurations in the experimental investigation.

2.1 Aerodynamic Testing

The study was conducted in the Subsonic Aerodynamics Research Laboratory at the University of Illinois at Urbana-Champaign. The laboratory is split into a control room, which is the primary location of the data acquisition equipment, and a test high bay, which houses two subsonic wind tunnels. The layout of the Aerodynamics Research Laboratory can be seen in Fig. 2.1.

2.1.1 Wind Tunnel

All aerodynamic testing was performed using a subsonic, low-turbulence, open-return-type wind tunnel. The test section of this wind tunnel was rectangular, measuring 2.8-ft by 4-ft, and running a total downstream length of 8 ft. The inlet settling section of the wind tunnel housed a four-inch thick honeycomb flow straightener, as well as four stainless steel anti-

turbulence screens. These screens effectively reduced the turbulence intensity within the empty test section below 0.1% for all operating speeds. The area ratio between the inlet and the test section was 7.5:1. An illustration of the wind tunnel is shown in Fig. 2.2. In order to account for wall boundary-layer growth through the test section, the downstream end of the test section was 0.5 inches wider than the upstream end.

The tunnel was powered by an ABB ACS 600 Low Voltage AC Drive, which regulated a 125 horsepower AC motor, which was used to drive a five-bladed fan. The maximum fan setting was approximately 1200 rpm, which resulted in a maximum empty test section speed of approximately 165 mph (242 ft/sec). This resulted in a maximum Reynolds number of Re = 1.5 $\times 10^6$ / ft. Reynolds number of an airfoil model was calculated using the equation,

$$\mathrm{Re} = \frac{\rho U_\infty c}{\mu} \tag{2.1}$$

During testing, the Reynolds number was computer-controlled to within 2%. The test section airspeed was determined by calculating the pressure difference (ΔP) between the inlet settling section and test section ($P_{ss} - P_{ts}$). The ΔP was measured using a Setra 239 differential pressure transducer. A set of four pressure taps just downstream of the anti-turbulence screens were connected by a single tube to the pressure transducer to provide an average settling section static pressure, P_{ss}. A set of four pressure taps located just upstream of the test section were also fed through a single tube to the pressure transducer to provide an average test section static pressure, P_{ts}. By assuming a steady, inviscid flow, and using the law of conservation of mass for an incompressible fluid (Eq. 2.2) and Bernoulli's equation (Eq. 2.3), the test section airspeed could be calculated using Eq. 2.4.

$$A_{ss}U_{ss} = A_{ts}U_{ts} \tag{2.2}$$

$$\frac{1}{2}\rho U_{ts}^2 + P_{ts} = \frac{1}{2}\rho U_{ss}^2 + P_{ss} \tag{2.3}$$

$$U_{ts} = \sqrt{\frac{2\left(P_{ss} - P_{ts}\right)}{\rho_{amb}\left(1 - \left(\frac{A_{ts}}{A_{ss}}\right)^2\right)}} \tag{2.4}$$

In Eq. 2.4, A_{ts}/A_{ss} was the reciprocal of the contraction area ratio, and ρ_{amb} was the ambient air density, which was calculated using the ideal gas law,

$$\rho_{amb} = \frac{P_{amb}}{RT_{amb}} \tag{2.5}$$

In Eq. 2.5, R was the ideal gas constant for air. Equation 2.5 also required the ambient pressure (P_{amb}), which was measured using a Setra 270 pressure transducer, and ambient temperature (T_{amb}), which was measured using an Omega thermocouple, located in the tunnel high bay.

2.1.2 Airfoil Models

Two airfoil models were used in this investigation – an NACA 3415 and an NACA 23012. Both airfoil models had an 18-inch chord and a 33.563-inch span. Additionally, both models had a 25% chord trailing-edge simple flap. The models were mounted vertically in the test section, spanning the tunnel floor to ceiling. Upon installation, the ceiling of the test section was removed and the model was lowered into the test section with the assistance of an overhead crane. Mounting brackets were used to secure the model in position and to transfer the aerodynamic loading from the model to the force balance plate, which is described in Section 2.1.4. The three spars of the airfoil model were fed through a cover plate located towards the center of the balance turntable. The holes in the cover plate had been previously machined, allowing minimal clearances of the spars in an effort to minimize air leakage into the test section.

The main spar of the model was located at the quarter-chord location of the airfoil, and was slightly offset from the balance force plate centerline. The NACA 3415 model quarter-chord was 0.25 inches upstream and 0.512 inches below the centerline of the balance plate, and the NACA 23012 model quarter-chord was 0.25 inches upstream and 0.325 inches below the centerline of the balance plate. When the models were mounted in the test section, shims were used to create a gap of approximately 0.02 inches between the model and the test section floor. This ensured that the model would not come into contact with the balance turntable during aerodynamic loading, and thus ensured that the full loads and moments would be transferred to the balance.

After the test section ceiling was replaced, a gap, measuring approximately 0.125 inches, was created between the model and the test section ceiling with the use of an adjustable ceiling stiffener. This was done in an effort to prevent the ceiling from coming into contact with the

model during testing, as the ceiling deflected due to the pressure drop in the test section. Gaps inside and outside the tunnel were covered with Scotch book tape in an effort to minimize leakage into the tunnel during testing. A schematic of the tunnel test setup can be seen in Fig. 2.3.

A series of pressure taps, located on the airfoil model's surface, were used to measure the pressures on the airfoil surface. The NACA 3415 model had 40 chordwise pressure taps on the main element upper surface, and 23 chordwise pressure taps on the main element lower surface. It also had 8 chordwise pressure taps on the flap upper surface and 6 chordwise pressure taps on the flap lower surface. In an effort to prevent interference due to flow transition, the taps between the leading edge and mid chord were aligned at an angle of approximately 15° offset from the flow direction. In addition to the chordwise taps, the flap also had 13 spanwise taps located at 90% chord. The locations of the pressure taps for the NACA 3415 model are illustrated in Fig. 2.4.

The NACA 23012 model had 36 chordwise pressure taps on the main element upper surface and 14 chordwise pressure taps on the main element lower surface. It also had 12 chordwise pressure taps on the flap upper surface and 6 chordwise pressure taps on the flap lower surface. Much like the NACA 3415 model, the chordwise taps of the NACA 23012 model were aligned at an angle of approximately 15° offset from the flow direction. In addition to the chordwise taps, the flap also had 12 spanwise taps located at 90% chord. The locations of the pressure taps for the NACA 23012 model are illustrated in Fig. 2.5.

2.1.3 Data Acquisition System

The software used for the data acquisition of the NACA 3415 was programmed using Lab Windows/CVI. The NACA 23012 data were taken using software programmed using LabView. These programs were run on a Dell Precision T3400 computer with an Intel® Core™ Quad CPU, measuring a clock speed of 2.83 GHz, and having 4 GB RAM. The computer was run using a Windows XP 32-bit operating system. The data acquisition software incorporated a graphical user interface, where actions could be performed by clicking buttons on the user's display. Commands and tasks sent by the data acquisition computer to the three-component balance, tunnel variable frequency drive controller, IDC drive, and Velmex drive were sent via RS-232 communication. Model pressure measurements and wake surveys were acquired

through a National Instruments General Purpose Interface Bus (GPIB) IEEE-488 board. Data from the three-component balance and the hinge moment balance were converted through a National Instruments analog to digital (A/D) conversion board.

2.1.4 Force Balance

A three-component external force and moment balance was used to obtain model lift, drag, and quarter-chord pitching moment measurements. The balance was manufactured by Aerotech ATE Limited, of Heathfield, U.K., and can be seen in Fig. 2.6. An airfoil model was mounted to the force plate with mounting brackets, and measurements were taken using three load cells. The load cells provided forces in the normal and axial direction, as well as the moment about the center of the force plate. The balance was equipped with three different load range settings. Each of the three different measurements taken by the balance had a selection of three load ranges. Thus, changing the load range for a force or moment could be performed in an effort to optimize the measurement. The balance load ranges are provided in Table 2.1. For all tests in this investigation, the high range was used for all measurements.

Table 2.1 Balance Load Ranges.

	HIGH RANGE	MEDIUM RANGE	LOW RANGE
NORMAL FORCE	± 450 lbs.	± 225 lbs.	± 90 lbs.
AXIAL FORCE	± 90 lbs.	± 55 lbs.	± 18 lbs.
PITCHING MOMENT	± 45 ft-lbs.	± 30 ft-lbs.	± 15 ft-lbs.

The load cells had a full-scale output voltage of ± 20 mV, which were low-pass filtered at 1 Hz, then amplified to a full-scale voltage of ± 5 V using a signal conditioning system. The turntable was also used to adjust the angle of attack of the model. The turntable was controllable to within 0.1°. The balance took 200 samples at a rate of 100 Hz, and then the samples were averaged to provide a single voltage for both of the forces and the moment.

2.1.4.1 Force and Moment Calculation

Balance tare voltages were taken periodically for the angle-of-attack range that would be used in the upcoming tests. When experiments were carried out, the balance would take voltage measurements for the three components, and subtract the previously-obtained balance tare

voltages from the corresponding measurements. This difference (V_{0i}) was then multiplied by a range ratio (RR_i), which was dependent on the load range setting, in order to obtain a scaled voltage (V_i), as seen in Eq. 2.6. These balance range ratios are provided in Table 2.2.

$$V_i = V_{0i} \cdot RR_i \tag{2.6}$$

Table 2.2 Force Balance Range Ratios.

	HIGH RANGE	MEDIUM RANGE	LOW RANGE
NORMAL, RR_N	1	0.4944	0.2046
AXIAL, RR_A	1	0.6278	0.2173
MOMENT, RR_M	1	0.6755	0.3413

The resulting voltages (V_N, V_A, V_M) corresponded to the scaled voltage measurements for the forces and moment in each direction (normal-component, axial-component, pitching moment, respectively). These voltages were substituted into the calibration matrix of the force balance,

$$\begin{Bmatrix} F_N \\ F_A \\ M \end{Bmatrix} = \begin{bmatrix} 37.7 & 0.01359 & -0.2095 & 0.01094 & 0 & -0.000865 \\ -0.1607 & 8.3125 & -0.01638 & 0.007084 & 0 & 0.007660 \\ -0.01299 & -0.005521 & 1.247 & -0.002122 & 0 & 0.0001497 \end{bmatrix} \begin{Bmatrix} V_N \\ V_A \\ V_M \\ V_N^2 \\ V_A^2 \\ V_M^2 \end{Bmatrix} \tag{2.7}$$

After substituting the scaled voltages into Eq. 2.7, the calculated normal force (F_N), axial force (F_A), and pitching moment (M) resulted. These measurements were then used to calculate the lift, drag, and quarter-chord pitching moment of the airfoil model using Eqs. 2.8, 2.9, and 2.10 respectively.

$$L = F_N \cos\alpha - F_A \sin\alpha \tag{2.8}$$

$$D = F_N \sin\alpha + F_A \cos\alpha \tag{2.9}$$

$$M_{c/4} = M + x_{offset} F_N + y_{offset} F_A \tag{2.10}$$

In Eq. 2.10, x_{offset} and y_{offset} represent the distance the quarter-chord point of the model is from the center of the force balance plate. The non-dimensional lift coefficient (C_l) and drag coefficient (C_d) were calculated by dividing the force by the freestream dynamic pressure (q_∞) and model reference area (S), as seen in Eqs. 2.11 and 2.12, respectively. The non-dimensional pitching moment coefficient about the quarter-chord (C_m) was calculated by dividing the moment by q_∞, S, and the model chord (c), as in Eq. 2.13. While the force balance was used to measure drag, the drag data obtained from the balance will not be presented in the results section of this paper. The drag data obtained from the force balance include an induced drag component, which typically makes the balance drag data higher than that measured by the wake survey system, which will be described in Section 2.1.7. Thus, the drag data obtained from the force balance were used for comparison purposes only. Airfoil sectional coefficients were then obtained from balance measurements as below:

$$C_l = \frac{L}{q_\infty S} \tag{2.11}$$

$$C_d = \frac{D}{q_\infty S} \tag{2.12}$$

$$C_m = \frac{M_{c/4}}{q_\infty S c} \tag{2.13}$$

2.1.5 Flap Hinge Balance

The flap was regulated by a Velmex VP9000 Controller and an A40-08 single-axis linear traverse, which was connected to the flap spar by a two-arm linkage. This assembly was mounted on the force plate of the three-component balance. The flap two-arm linkage consisted of a clamp arm that was tightly secured to the flap spar, a connecting arm that was able to rotate on ball bearings at the connection to the clamp arm, and an upright support that was fastened to the traverse plate. An Omegadyne LCFD-50 load cell was also integrated into the connecting arm in order to perform hinge moment measurements. The load cell was situated in such a fashion that it would measure the forces acting normal to the flap. A picture and schematic of the flap hinge balance assembly can be seen in Fig. 2.7 and Fig. 2.8, respectively.

The hinge balance was calibrated by applying weights to the flap at a prescribed moment arm from the hinge, inducing a known hinge moment, and measuring the average voltage output of the load cell. This was accomplished by attaching a cable to a padded clamp, which was secured to the trailing-edge of the model flap, and running the cable through a pulley system such that the applied loads were transferred from the vertical plane to the horizontal plane. For the NACA 3415 installation, weights of 0 lbs, 5 lbs, 10 lbs, 15 lbs, and 20 lbs were applied with a moment arm of 6.88 inches at flap deflections of 0°, ± 5°, ± 10°, and ± 15°. For the NACA 23012 installation, weights of 0 lbs, 2 lbs, 4 lbs, 6 lbs, 8 lbs, and 10 lbs were applied with a moment arm of 6.36 inches at flap deflections of 0°, ± 5°, ± 10°, and ± 15°. After testing the NACA 3415, it was determined that the hinge moments used in the calibration were much higher than the resulting hinge moments in testing. Thus, in order to improve the precision of the hinge moment calibration and measurement, the range of hinge moments used for calibration of the NACA 23012 were lower. The induced hinge moments from these calibrations were well above the hinge moments that resulted during testing.

Hinge moment measurements were taken at a frequency of 3 kHz for 10 seconds. The hinge moment signal was low-pass filtered at 10 kHz, and amplified to a full-scale voltage of ± 5 V. Since the low-pass filter cutoff frequency was higher than the Nyquist frequency, small amounts of aliasing of the signal were present in the power spectral density (PSD) of the hinge moment signal. However, the cutoff frequency was set to 10 kHz in an effort to capture peaks in the PSD that could exist at characteristic frequencies above the Nyquist frequency of 1.5 kHz. These peaks would be visible in the PSD as the aliased signal would be projected into the frequency domain between 0 Hz and 1.5 kHz. The calibration hinge moment (H) was calculated using the moment arm (d_h), the applied loads (F_h), and flap angle (δ_f) using the equation,

$$H = F_h d_h \cos\delta_f \tag{2.14}$$

H was then plotted versus the load cell voltage output (V_h) measured during the calibration for each flap setting. A linear trendline was then applied to the data to determine the conversion slope (m) and intercept (b) for each flap angle by using,

$$H = mV_h + b \tag{2.15}$$

A sample calibration curve at a flap setting of 0° for the NACA 23012 can be seen in Fig. 2.9.

2.1.5.1 Hinge Moment Calculation

Much like with the three-component balance, tares of the flap balance were taken periodically. Both mean and unsteady hinge moment data were recorded. When experiments were carried out, the tare voltage would be subtracted from the measured voltage, and this difference would be multiplied by the conversion slope. The hinge moment coefficient (C_h) was calculated using the equation,

$$C_h = \frac{H}{q_\infty S_f \, c_f} \tag{2.16}$$

In Eq. 2.16, c_f represents the flap chord (length aft of the main element), and S_f represents the flap reference area, which was calculated using the equation,

$$S_f = c_f b \tag{2.17}$$

where b is the model span.

2.1.5.2 Time-Dependent Measurements

The time-averaged, or mean, hinge moment coefficient was calculated using the equation,

$$\overline{C}_h = \frac{1}{N}\sum_{i=1}^{N} C_{h_i} \tag{2.18}$$

where N represents the total number of samples in the data set. The unsteady hinge moment measurements were also represented by the standard deviation of the hinge moment coefficient samples. The standard deviation of the sample ($C_{h,StDev}$) quantified the amount and magnitude of fluctuation of the unsteady hinge moment coefficient from the mean value of hinge moment coefficient. $C_{h,StDev}$ was calculated using the equation,

$$C_{h,StDev} = \sqrt{\frac{1}{N}\sum_{i=1}^{N}(C_{h_i} - \overline{C}_h)^2} \tag{2.19}$$

2.1.6 Pressure Measurement System

Pressure measurements on the airfoil model surface were taken using the static pressure taps described in Section 2.1.2. The pressure measurements were taken using a Pressure

Systems Incorporated (PSI) System 8400. This digital pressure acquisition system consisted of a Central Control Module, a 14-bit 8420 Scanner Digitizer Unit, 1.0 and 5.0 psid Pressure Calibration Units (PCU), and a Scanner Interface. Miniature Electronically Scanned Pressure (ESP) units were used to take pressure samples at 50 Hz for two seconds. The scanners were model ESP-32 units, all of which had 32 ports. Each of the 32 ports could be connected to a pressure tap on the model, or a total pressure port on the wake survey system, which is described in Section 2.1.7. Polyurethane or vinyl tubing was used to connect the pressure taps on the model to pressure ports on the scanners. In addition to the 32 individual pressure ports, each scanner had one or two reference ports, a pressure calibration port, and two switch calibration ports, C_1 and C_2.

Three different ranges of scanners were used in this investigation. A ± 5.0 psid scanner (denoted J_1) was connected to the model leading-edge taps where the pressure differentials were the highest, two ± 1.0 psid scanners (denoted J_2 and J_3) were connected to the remaining model pressure taps, and two ± 0.35 psid (± 10.0 inches of water) scanners (denoted J_4 and J_5) were connected to the total pressure tubes in the wake survey system. The scanners were regularly calibrated with the use of the data acquisition computer program. The program was able to switch the PSI system between run mode and calibration mode by applying 100-psi of nitrogen (from a nitrogen tank), for approximately 20 seconds, to the C_1 or C_2 port on the scanners. In order to calibrate the scanners, a vacuum pump was used along with the 5.0 psid PCU to calibrate the ± 5.0 and ± 1.0 psid scanners, and along with the 1.0 psid PCU to calibrate the ± 0.35 psid scanners.

2.1.6.1 Dynamic Pressure and Pressure Coefficient Calculation

In order to calculate the pressure distribution around the airfoil surface, q_∞ was first calculated. q_∞ is defined as,

$$q_\infty = \frac{1}{2}\rho_\infty U_\infty^2 \tag{2.20}$$

By using Bernoulli's equation (Eq. 2.3) and conservation of mass for an incompressible fluid (Eq. 2.2), Eq. 2.20 becomes,

$$q_\infty = \frac{1}{2}\rho_\infty U_{ts}^2 = \frac{P_{ss} - P_{ts}}{1 - \left(\frac{A_{ts}}{A_{ss}}\right)^2} \tag{2.21}$$

where ρ_∞ represents the freestream air density, which was assumed to be the same as ρ_{amb} from Eq. 2.4. The pressure coefficients (C_p) on the airfoil surface were calculated using the conventional definition,

$$C_p = \frac{P_s - P_\infty}{q_\infty} = \frac{P_s - P_{ts}}{P_{ss} - P_{ts}}\left[1 - \left(\frac{A_{ts}}{A_{ss}}\right)^2\right] \tag{2.22}$$

where P_s is the static pressure on the airfoil surface. The model ESP units were referenced to the test section static pressure, so the difference ($P_s - P_{ts}$) is actually the quantity measured by the scanners. The quantity ($P_{ss} - P_{ts}$) was obtained using port number 32 on J_3, which was connected to the settling section of the wind tunnel.

2.1.6.2 Force and Moment Calculation

Using the pressure distribution around the airfoil, it was possible to calculate the lift and pitching moment coefficients for the airfoil. This was accomplished by considering the airfoil surface to be split into a series of panels, each panel running in the chordwise direction between two adjacent pressure taps on the model. The surface pressure of each panel was divided into normal and axial components, as shown in Eqs. 2.23 and 2.24, respectively. A detailed explanation of this calculation process can also be found in Anderson.[15]

$$\Delta F_{N_i'} = \frac{P_i + P_{i+1}}{2}\left(x_{i+1} - x_i\right) \tag{2.23}$$

$$\Delta F_{A_i'} = -\frac{P_i + P_{i+1}}{2}\left(y_{i+1} - y_i\right) \tag{2.24}$$

The net normal and axial forces acting on the airfoil were calculated by summing the forces over all panels, as seen in Eqs. 2.25 and 2.26. Using the normal and axial forces, the lift of an airfoil can be calculated, as seen in Eq. 2.27,

$$F_{N'} = \sum_{i=1}^{n-1} \Delta F_{N'_i} \tag{2.25}$$

$$F_{A'} = \sum_{i=1}^{n-1} \Delta F_{A'_i} \tag{2.26}$$

$$L' = F_{N'} \cos\alpha - F_{A'} \sin\alpha \tag{2.27}$$

where n represents the total number of chordwise pressure taps on the model. The contribution of each panel to quarter-chord pitching moment could be calculated using the force on each panel and its moment arm from the quarter-chord,

$$\Delta M'_{c/4_i} = \Delta F_{N'_i}\left(x_{c/4} - \frac{x_i + x_{i+1}}{2}\right) + \Delta F_{A'_i}\left(\frac{y_i + y_{i+1}}{2}\right) \tag{2.28}$$

The incremental quarter-chord pitching moment per unit span was then summed in order to calculate the net quarter-chord pitching moment for the airfoil section,

$$M'_{c/4} = \sum_{i=1}^{n-1} \Delta M'_{c/4_i} \tag{2.29}$$

The flap hinge moment was calculated in a very similar fashion as the quarter-chord pitching moment. The key differences, however, were that the moment was taken about the location of the flap hinge and only the pressure taps located on the flap were considered in the calculation. The hinge moment coefficient for each flap panel was calculated using,

$$\Delta H'_i = \Delta F_{N'_i}\left(x_h - \frac{x_i + x_{i+1}}{2}\right) + \Delta F_{A'_i}\left(\frac{y_i + y_{i+1}}{2} - y_h\right) \tag{2.30}$$

where x_h and y_h correspond to the x and y chordwise location of the flap hinge. The net hinge moment coefficient over the flap was then calculated by summing the hinge moment coefficient of each panel on the flap,

$$H' = \sum_{i=1}^{n_{flap}-1} \Delta H'_i \tag{2.31}$$

where n_{flap} represents the number of chordwise pressure taps on the flap. Using the calculated lift per unit span, quarter-chord pitching moment per unit span, and hinge moment per unit span,

the lift coefficient, quarter-chord pitching moment coefficient, and hinge moment coefficient were calculated using Eqs. 2.32, 2.33, and 2.34, respectively.

$$C_l = \frac{L'}{q_\infty c} \tag{2.32}$$

$$C_m = \frac{M'}{q_\infty c^2} \tag{2.33}$$

$$C_h = \frac{H'}{q_\infty c_f^2} \tag{2.34}$$

It should be noted that since the pressure taps used in these calculations were located at a section towards the spanwise center of the model, the lift and quarter-chord pitching moment calculated using the pressure measurements are only valid for the center section of the model. The lift and quarter-chord pitching moments that were calculated from the balance measurements, from Section 2.1.4, were averaged across the entire 33.563-inch span of the model.

2.1.7 Wake Survey System

The primary drag measurements were obtained using a traversable wake rake system. The wake rake was comprised of 59 total pressure probes, which were made from straight, thin-walled tubing with outer diameters measuring 0.04 inches. These tubes were horizontally aligned, parallel to the freestream flow direction, in order to capture total pressure deficits in the wake generated by the model. The rake spanned 9.75 inches, with 0.135-inch spacing between probes in the middle of the rake and 0.27-inch spacing between six probes at each end. A picture of the wake rake mounted in the test section can be seen in Fig. 2.10. The wake rake was able to traverse in both the vertical (spanwise) and horizontal directions, using two Lintech traverse axes which were controlled by an IDC S6962 Stepper Motor Drive. A pressure box, sealed to the outside, was installed around the Lintech traverse system in an effort to minimize air leakage into the tunnel. As noted previously, wake pressure measurements were taken using the PSI System 8400 and two ± 0.35 psid ESP units. While the wake rake was also equipped with three static probes, these probes were not used in this investigation.

The span of the wake rake was large enough to capture the entire wake of the model while the flowfield was attached to the model; however, the separated wake was much larger and required additional measurements. The computer program controlled the wake rake and identified the location of the wake by finding the location of minimum pressure across the test section. The program then centered the wake rake at the location of minimum wake pressure. It then moved the wake rake horizontally, if necessary, until a location of constant total pressure was found, indicating the edge of the wake from the model. The program then calculated the total number of rake spans necessary to capture the entire wake, moved in the opposite horizontal direction, and began taking pressure measurements of the entire wake.

2.1.7.1 Drag Calculation

The standard momentum deficit method found in Jones[16] and Schlichting[17] was used to calculate the drag from the wake pressures. This method assumes a plane, denoted by subscript 1, is far downstream of the model where the static pressure in the wake (P_w) is equal to the static pressure in the freestream (P_∞). Using this assumption, the drag per unit span can be calculated,

$$D' = \rho \int u_1 (U_\infty - u_1) dy_1 \tag{2.35}$$

It is then assumed that there exists a second plane, perpendicular to the freestream and closer to the model where the wake rake measurements are taken. Conservation of mass is applied to a streamtube that runs between the two planes, Eq. 2.36, and is substituted into Eq. 2.35, resulting in Eq. 2.37.

$$u_1 dy_1 = u_w dy \tag{2.36}$$

$$D' = \rho \int u_w (U_\infty - u_1) dy \tag{2.37}$$

The total pressures for the freestream, plane 1, and the wake plane can be expressed as Eqs. 2.38, 2.39, and 2.40, respectively.

$$P_\infty + \frac{1}{2} \rho U_\infty^2 = P_{0,\infty} \tag{2.38}$$

$$P_\infty + \frac{1}{2}\rho u_1^2 = P_{0,1} \tag{2.39}$$

$$P_\infty + \frac{1}{2}\rho u_w^2 = P_{0,w} \tag{2.40}$$

Solving Eqs. 2.38, 2.39, and 2.40 for U_∞, u_1, and u_w, and by assuming there are no pressure losses between the wake plane and plane 1 such that $P_{0,1} = P_{0,w}$, and substituting into Eq. 2.37, the drag per unit span was calculated,

$$D' = 2\int \sqrt{P_{0,w} - P_w}\left(\sqrt{P_{0,\infty} - P_\infty} - \sqrt{P_{0,w} - P_\infty}\right)dy \tag{2.41}$$

By assuming that $P_w = P_\infty$ and by combining Eqs. 2.38 and 2.40,

$$q_w = q_\infty - \left(P_{0,\infty} - P_{0,w}\right) \tag{2.42}$$

A suggestion noted in Lee[18] was to rearrange Eq. 2.41 and write it in terms of dynamic pressure. With the additional substitution of Eq. 2.42, the expression for drag per unit span became,

$$D' = 2\int \sqrt{q_\infty - \left(P_{0,\infty} - P_{0,w}\right)}\left(\sqrt{q_\infty} - \sqrt{q_\infty - \left(P_{0,\infty} - P_{0,w}\right)}\right)dy \tag{2.43}$$

The equation for drag per unit span from Eq. 2.43 is very useful, as it is possible to calculate the pressure difference ($P_{0,\infty} - P_{0,w}$) directly from the wake survey measurements. The wake survey system measured the pressure difference ($P_{0,w} - P_{atm}$) in the wake, as the ± 0.35 psid ESP units were referenced to the atmospheric pressure. At the edge of the wake, where the total pressure was assumed to be equivalent to the freestream total pressure, the wake survey measured the pressure difference ($P_{0,\infty} - P_{atm}$). Thus, the pressure difference ($P_{0,\infty} - P_{0,w}$) could be calculated by,

$$P_{0,\infty} - P_{0,w} = \left(P_{0,\infty} - P_{atm}\right) - \left(P_{0,w} - P_{atm}\right) \tag{2.44}$$

The trapezoidal method was used to numerically solve for the integral in Eq. 2.43. The resulting calculation for incremental sectional drag became,

$$\Delta D' = \left[\sqrt{q_\infty - \left(P_{0,\infty} - P_{0,w_i}\right)}\left(\sqrt{q_\infty} - \sqrt{q_\infty - \left(P_{0,\infty} - P_{0,w_i}\right)}\right) + \sqrt{q_\infty - \left(P_{0,\infty} - P_{0,w_{i+1}}\right)}\left(\sqrt{q_\infty} - \sqrt{q_\infty - \left(P_{0,\infty} - P_{0,w_{i+1}}\right)}\right)\right]\left(y_i - y_{i+1}\right) \tag{2.45}$$

In order to find the total sectional drag per unit span, the incremental sectional drag was summed over the total number or probes (n_{rake}) used to measure the wake, as seen in Eq. 2.46. Measurements outside of the wake of the model, where the measured total pressure was equal to the freestream total pressure, were ignored as they did not contribute to the calculation of drag.

$$D' = \sum_{i=1}^{n_{rake}} \Delta D'_i \tag{2.46}$$

Using the sectional drag per unit span, the drag coefficient was calculated using the equation,

$$C_d = \frac{D'}{q_\infty c} \tag{2.47}$$

2.1.8 Wind Tunnel Corrections

Since all wind tunnel tests were performed in a finite domain, the exact conditions of true atmospheric flight could not be perfectly duplicated. The presence of the walls in the tunnel altered the flowfield past the model. Therefore, corrections were made to the measurements taken in all tests. The three most important corrections made in this investigation were for solid blockage, wake blockage, and streamline curvature. The methods used to compensate for these effects are based from those outlined in Barlow, Rae, and Pope.[19]

Solid blockage is the reduction in the test section area due to the presence of a model. Since the mass flow rate across the test section must be constant, as the area of the model perpendicular to the flow becomes larger, the airspeed must be increased. This velocity increase is a function of model angle of attack, thickness (t), thickness distribution, and model size. The correction factor for solid blockage, known as the solid-blockage velocity increment (ε_{sb}), can be estimated using the equation,

$$\varepsilon_{sb} = \frac{K_1(\text{model volume})}{C^{3/2}} \tag{2.48}$$

where K_1 is a factor of 0.52 for a model spanning the wind tunnel height (which can be found in Barlow, Rae, and Pope[19]), and C is the test-section area.

Wake blockage is an increase in flow velocity outside of the wake in a closed wind tunnel. Since the velocity inside of a wake is less than the freestream velocity, in order for the mass flow rate to be conserved, the velocity of the flow outside the wake must be greater than the freestream velocity. The correction factor for wake blockage, known as the wake-blockage velocity increment (ε_{wb}), can be calculated using the equation,

$$\varepsilon_{wb} = \frac{1}{2}\frac{c}{h}C_{d,u} \tag{2.49}$$

where h is the test-section height and $C_{d,u}$ is the uncorrected value for the airfoil drag coefficient. The total velocity increment (ε) was calculated by adding the solid-blockage increment and the wake-blockage increment,

$$\varepsilon = \varepsilon_{sb} + \varepsilon_{wb} \tag{2.50}$$

Streamline curvature is a distortion of the natural streamlines due to the presence of the walls of the tunnel. This causes the airfoil in a closed wind tunnel to appear to have more camber than it actually has, leading to an increase in lift and quarter-chord pitching moment. This effect is accounted for with the use of the variable σ,

$$\sigma = \frac{\pi^2}{48}\left(\frac{c}{h}\right)^2 \tag{2.51}$$

The correction factors calculated in Eqs. 2.48-51 were used to obtain corrected values of angle of attack, lift coefficient, drag coefficient, and quarter-chord pitching moment coefficient. Corrected values were calculated for both the pressure and balance data. The corrected parameters were calculated using Eqs. 2.52-55.

$$\alpha_{cor} = \alpha_u + \frac{57.3\sigma}{2\pi}\left(C_{l,u} + 4C_{m,u}\right) \tag{2.52}$$

$$C_{l,cor} = C_{l,u}\left(1 - \sigma - 2\varepsilon\right) \tag{2.53}$$

$$C_{d,cor} = C_{d,u}\left(1 - 3\varepsilon_{sb} - 2\varepsilon_{wb}\right) \tag{2.54}$$

$$C_{m,cor} = C_{m,u}(1-2\varepsilon) + \frac{1}{4}\sigma C_{l,u} \tag{2.55}$$

2.1.9 Test Matrix

Tests were performed for all model configurations with flap deflections of 0°, ± 5°, and ± 10°. Additionally, for the NACA 3415 model with trim tab configuration, which is described in Section 2.3, further tests were performed with trim tab deflections of 0° and ± 5° for flap settings of ± 5° under the clean and simulated glaze-ice configurations. For all flap and trim tab settings, tests were performed at Reynolds numbers of 1.8×10^6 and 1.0×10^6.

2.2 Contamination Simulations

A significant part of this study was devoted to investigating the effects of various types and degrees of simulated contamination on the performance characteristics of the airfoil models, particularly on the hinge moment coefficient. In this investigation, effects of simulated icing, distributed leading-edge roughness, and simulated three-dimensional damage were tested. This led to a total of six contamination cases tested for each model. Since it was not feasible in this investigation to replicate icing and 3D damage cases exactly, the cases were simulated instead.

2.2.1 Simulated Icing

Icing conditions can be very unforgiving, and accidents related to in-flight icing continue to occur. To obtain a better understanding of the relationship between ice accretion and performance characteristics, two different icing cases were simulated in this investigation – glaze ice and rime ice.

2.2.1.1 Simulated Glaze Ice

The first icing case simulated was that of a glaze-ice accretion. Glaze-ice shapes are characterized by "horn" formations which form on the model upper, and possibly lower surface near the leading edge. The horn formation can be likened to a large protrusion which is orientated at a significant angle to the oncoming flow. This horn typically creates a large separation bubble downstream of the accretion. The glaze-ice case that was simulated in the current experiment was much like the cold hold runback icing case found in Whalen et al.[20] A

tracing and photograph of the cold hold runback icing case on a proprietary business jet-type aircraft airfoil model can be found in Fig. 2.11.

Some glaze-ice accretions can be simulated using a forward facing quarter-round geometry which mimics the glaze horn protrusion. The forward facing quarter-round has been used previously by Lee and Bragg[21] to simulate glaze and other types of ice shapes. A schematic of the glaze-ice simulation used in the current experiment can be seen in Fig. 2.12. The glaze-ice case was simulated using a forward-facing, wooden quarter-round. From Fig. 2.12, the quarter-round had a height of 0.25 in, and was attached to the airfoil upper surface at $x/c = 0.02$, using 0.003-in thick double-sided tape. A photograph of the simulated glaze shape on the NACA 3415 model is shown in Fig. 2.13, and on the NACA 23012 model is shown in Fig. 2.14.

2.2.1.2 Simulated Rime Ice

The second ice case simulated is that of a rime-ice accretion. Rime accretions are generally more conformal to the airfoil leading edge and lack the large horn protrusions observed in the glaze-ice accretions. Due to their more conformal shape, rime accretions are characterized by more localized separation on the scale of the ice shape. The rime-icing case that was tested in the current experiment was much like the EG1125 streamwise rime shape from Broeren et al.[22] A tracing and photograph of the EG1125 ice accretion on an NACA 23012 can be found in Fig. 2.15.

The rime-ice case was simulated using the same simple geometry method outlined in Busch et al.[23] The shape was simulated using two 0.125 × 0.15-in, and one 0.15 × 0.30-in balsa blocks attached to the leading edge of the airfoil model, with roughness attached. The upper-surface roughness was placed from $x/c = -0.008$ to $x/c = 0.019$ and had a maximum height of $(k/c)_{max} = 0.00167$. The lower-surface roughness was placed from $x/c = -0.006$ to $x/c = 0.029$ and had a maximum height of $(k/c)_{max} = 0.00122$. A schematic of the simulated rime shape is shown in Fig. 2.16.

Results from Busch et al. indicate that the simple geometry simulation for the rime-ice case affected the aerodynamic performance in a fashion that was consistent with the rime-ice shape casting. Busch found that the simple geometry simulation of the EG1125 spanwise ice shape on an NACA 23012 model had a $C_{l,max}$ only 4.4% higher than a full-scale rime casting, and stalled at an angle of attack only 0.4 degrees higher than the full-scale casting, which proved to

be a better simulation than a 2D cross-section of the full-scale casting.[23] A photograph of the simulated rime shape on the leading-edge of the NACA 3415 model is shown in Fig. 2.17, and on the NACA 23012 model is shown in Fig. 2.18.

2.2.2 Distributed Leading-Edge Roughness

In addition to the simulated ice accretions, two forms of general leading-edge surface roughness were tested. The two cases used an 80-grit roughness level and a 14-grit roughness level. The two sizes of roughness were tested to simulate different levels of leading-edge contaminants. These roughness cases were intended to simulate heavy rain, foreign debris (insects, dirt, etc.), or other forms of contamination from environmental sources.

2.2.2.1 80-Grit Roughness

In the first roughness contamination case, 80-grit sandpaper was attached to the leading edge of the model. The sandpaper extended from $x/c = 0.0$ to $x/c = 0.07$ on the upper surface, and from x/ c= 0.0 to $x/c = 0.01$ on the lower surface. The roughness height corresponded to a $(k/c)_{max} = 0.00064$. The location and roughness heights were selected in an effort to duplicate the same 80-grit sandpaper test performed in Broeren and Bragg.[24] The 80-grit sandpaper was used by Broeren and Bragg to create a very repeatable simulation of ice roughness to be tested on three different airfoil models. By utilizing the same roughness simulation, the current test can be compared to previous test results by Broeren and Bragg. Much like the referenced test setup, the sandpaper was cut and taped to the model in such a fashion as to avoid the leading-edge pressure taps. A photograph of the resulting contamination test setup on the NACA 3415 model is shown in Fig. 2.19, and on the NACA 23012 model is shown in Fig. 2.20.

2.2.2.2 14-Grit Roughness

The second case of leading-edge roughness covered the same surface of the model as the first case, but was covered with 14-grit roughness instead of 80-grit sandpaper. In order to accomplish this, a length of double-sided tape, with the same dimensions as the sandpaper covering, was created, using the 80-grit sandpaper as a stencil. Next, 14-grit silicon carbide abrasive was sprinkled over the double-sided tape. Compressive force was then applied to the abrasive to ensure abrasive adhesion to the tape, and to minimize the amount of abrasive that would detach from the tape upon installation and testing. The setup produced a $(k/c)_{max} =$

0.0042. A photograph of the large roughness contamination setup on the NACA 3415 model is shown in Fig. 2.21, and on the NACA 23012 model is shown in Fig. 2.22.

2.2.3 3D Simulated Damage

While the previous contamination cases were 2D in nature, the simulated damage cases tested in this investigation were 3D in nature. It was important for 3D cases to be tested to represent this class of contamination that also have adverse effects on the aerodynamic qualities of an aircraft. The purpose for including 3D contamination tests was to indicate whether or not a correlation could be made between the hinge moment characteristics and the flowfield associated with a large, 3D protuberance. The 3D simulated damage contamination cases were simulated using formations of 1.5-inch diameter hemisphere clusters. These hemispheres were used, as they shed distinct hairpin vortex structures that, during their formation, are capable of extracting energy from the boundary layer. The two 3D contamination cases simulated leading-edge damage and upper-surface damage. A schematic of the local flow past a hemisphere can be seen in Fig. 2.23.

2.2.3.1 Simulated Leading-Edge Damage

Leading-edge structural damage was simulated on the airfoil model using a cluster of six hemispheres. These hemispheres were attached to the model in a backward-facing triangular formation using hot glue. The leading edge of the hemisphere cluster was located at $x/c = 0.02$, and the trailing edge of the hemisphere cluster was located at $x/c = 0.26$. The leading-edge damage case is meant to simulate damage to the leading edge of the wing caused by collisions, like an in-flight bird strike on a wing or an on-ground accidental collision. A photograph of the 3D simulated leading-edge damage setup on the NACA 3415 model is shown in Fig. 2.24, and on the NACA 23012 model is shown in Fig. 2.25.

2.2.3.2 Simulated Upper-Surface Damage

The upper-surface damage case was simulated in a similar fashion as the leading-edge damage case. A total of eight hemispheres were adhered in a diamond formation on the upper surface of the model. The leading edge of the hemisphere cluster was located at $x/c = 0.15$, and the trailing edge of the hemisphere cluster was located at $x/c = 0.45$. The upper-surface damage case was designed to mimic a midchord structural perturbation, such as that produced by a

localized outward explosion/failure. A photograph of the 3D simulated surface damage test setup on the NACA 3415 model is shown in Fig. 2.26, and on the NACA 23012 model is shown in Fig. 2.27.

2.3 Trim Tab Installation

Control surfaces of aircraft are commonly outfitted with trim tabs, which are capable of changing the control surface deflection corresponding to zero hinge moment. Effectively, trim tabs are capable of alleviating flap or control surface hinge moments and reducing the amount of manual force required to maintain a control surface setting. For this reason, it is important to observe the impact of the trim tab deflection on unsteady hinge moment properties. In order to provide a more realistic representation of an aircraft wing, the NACA 3415 model with the simple flap was retrofitted with a trim tab.

The trim tab was modeled using a 0.04-inch thick piano hinge that ran the entire span of the model. The piano hinge had a 0.09375-inch pin diameter and a 2-inch open width. It was designed for tight clearances by having the pin placed mid-thickness between the two leaves of the hinge. The piano hinge was dismantled and one leaf of the hinge was attached to the lower surface of the NACA 3415 model using 0.031-inch thick and 0.75-inch wide double-sided polyurethane foam tape. The lower surface was selected to attach the piano hinge to, as any perturbation to the flowfield that could occur due to this addition would be lessened on the upper surface, which is more critical than the lower surface.

Book tape was used to reinforce the bond between the piano hinge leaf and the flap. Portions of the book tape were cut out in order to allow a length of tape to pass between the knuckles in the hinge at all spanwise locations. Thus, the piano hinge leaf was also connected to the flap by having the book tape wrapped around the trailing-edge of the flap, while also encasing the hinge leaf. The piano hinge was then reassembled, and book tape was used to alleviate the step between the flap lower surface and the piano hinge. A thin ramp was constructed from balsa wood and was attached to the trailing-edge leaf of the piano hinge using 0.003-inch removable vinyl double-sided tape. This was done in an attempt to alleviate the step from the pin (which was located just downstream of the trailing edge of the flap) to the trailing-edge leaf of the hinge. The bond was then reinforced with book tape, which also assisted in

streamlining the gaps between the piano hinge pin and the wooden ramp. A view of the trim tab upper surface with the balsa wood ramp can be seen in Fig. 2.28.

Four mounting brackets were manufactured to allow the trim tab to be fixed at set deflections. The brackets were created in pairs, one bracket with a large slot that aligns with a hole in its corresponding bracket, letting the hinge pivot, until bolts on each set of brackets were tightened. Drawings of the trim tab hinge mounting brackets can be seen in Fig. 2.29. The two pairs were placed on the model near the tunnel test section walls. A photograph of the NACA 3415 model with the trim tab installed can be seen in Fig. 2.30.

2.4 Flow Visualization

Since the 2D surface pressure distributions did not provide a representative understanding of the 3D flowfields associated with the 3D simulated damage cases, these flowfields were analyzed using flow visualization. A time-averaged image of the flowfield on the model surface was obtained using fluorescent-oil flow visualization. The fluorescent-oil flow visualization process was repeated for several angles of attack for the clean model and both the simulated leading-edge and simulated upper-surface damage cases. The process revealed regions of laminar, transitional, and turbulent flow, in addition to revealing regions of attached and separated flow.

The flow visualization technique used in this investigation was similar to Busch.[25] Before beginning the fluorescent-oil flow visualization, the model was wrapped with a monokote in order to cover the pressure taps and prevent oil from clogging the pressure lines. The monokote was a glossy black, which provided an optimal contrast between the fluorescence of the oil and the airfoil surface. Care was taken to avoid trapping dust particles or air bubbles beneath the surface of the monokote. Additionally, two strips of yellow electrical tape were applied to the model which were marked with the model chordwise *x/c* coordinates in 5% intervals. This allowed for easy identification of the locations of certain flowfield features. After applying the simulated damage to the monokote-covered model, the floor gap between the model and the turntable was sealed in order to protect the force balance by preventing any oil from flowing through the floor gaps below the model. The model was then rotated to its desired angle of attack and the gaps in the turntable were sealed to prevent any oil flow through to the mechanisms underneath the tunnel test section.

The oil application process started with spreading a coat of 10W-30 motor oil over the surface of the monokote. This filled in any small gaps or imperfections in the monokote and created a smooth surface for the fluorescent oil to flow across. The excess motor oil was then wiped away with a paper towel in the streamwise direction. The fluorescent oil mixture was created by mixing mineral oil and Kent-Moore 28431-1 fluorescent dye. Using Nitrogen gas regulated around 30 psi, a fine spray of the fluorescent oil was applied to the model with the use of an airbrush. An airbrush was necessary, as the spray had to be fine enough not to create individual droplets that could slide down the model due to the effects of gravity. Black lights were used to fluoresce the dye on the model and ensure complete coverage of the model.

After application of the mineral oil mixture, the wind tunnel was ramped up to speed and run for approximately 2 minutes. Upon completion, the tunnel was shut off, and the black lights were placed inside the tunnel test section in such a fashion to prevent causing a glare on the model. The overhead lights were turned off and the black lights were turned on. The ultraviolet wavelength of light excited the ultraviolet dye, causing it to fluoresce a green color. The flow patterns were then photographed using a Nikon model D100 digital SLR camera, using different extended exposure times. The photographs were uploaded to a computer and it was ensured that all important flowfield features were captured. The model was then wiped clean with paper towels and glass cleaner. The surface oil flow visualization procedure was then repeated for the next desired test case.

2.5 Figures

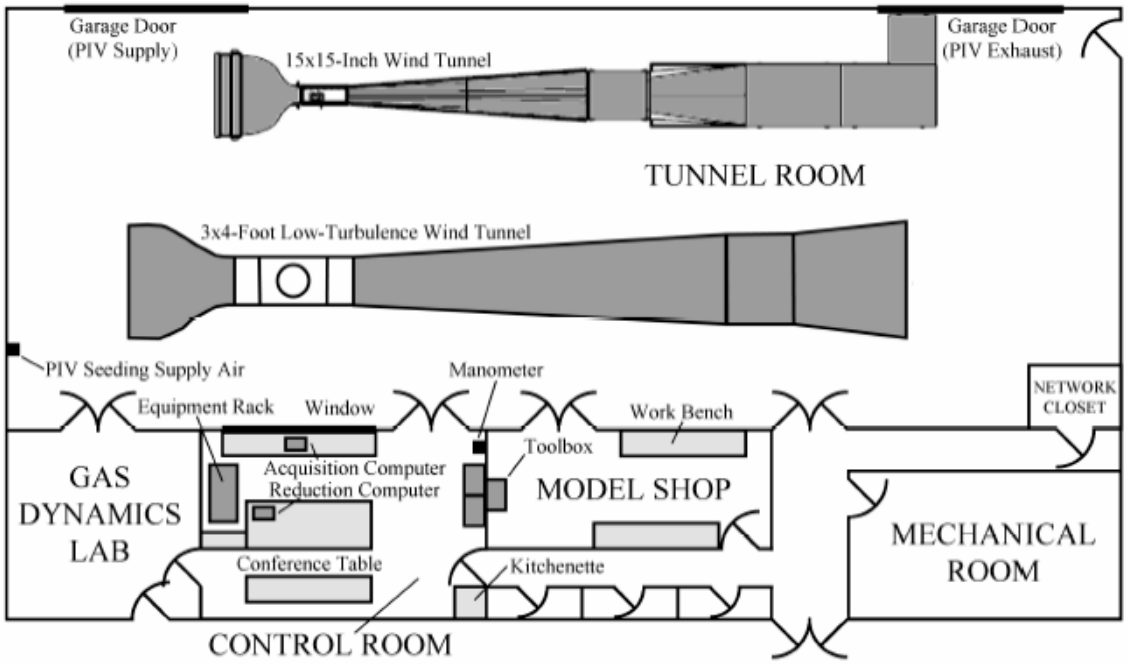

Fig. 2.1 University of Illinois Aerodynamics Research Laboratory (not to scale), after Jacobs.[26]

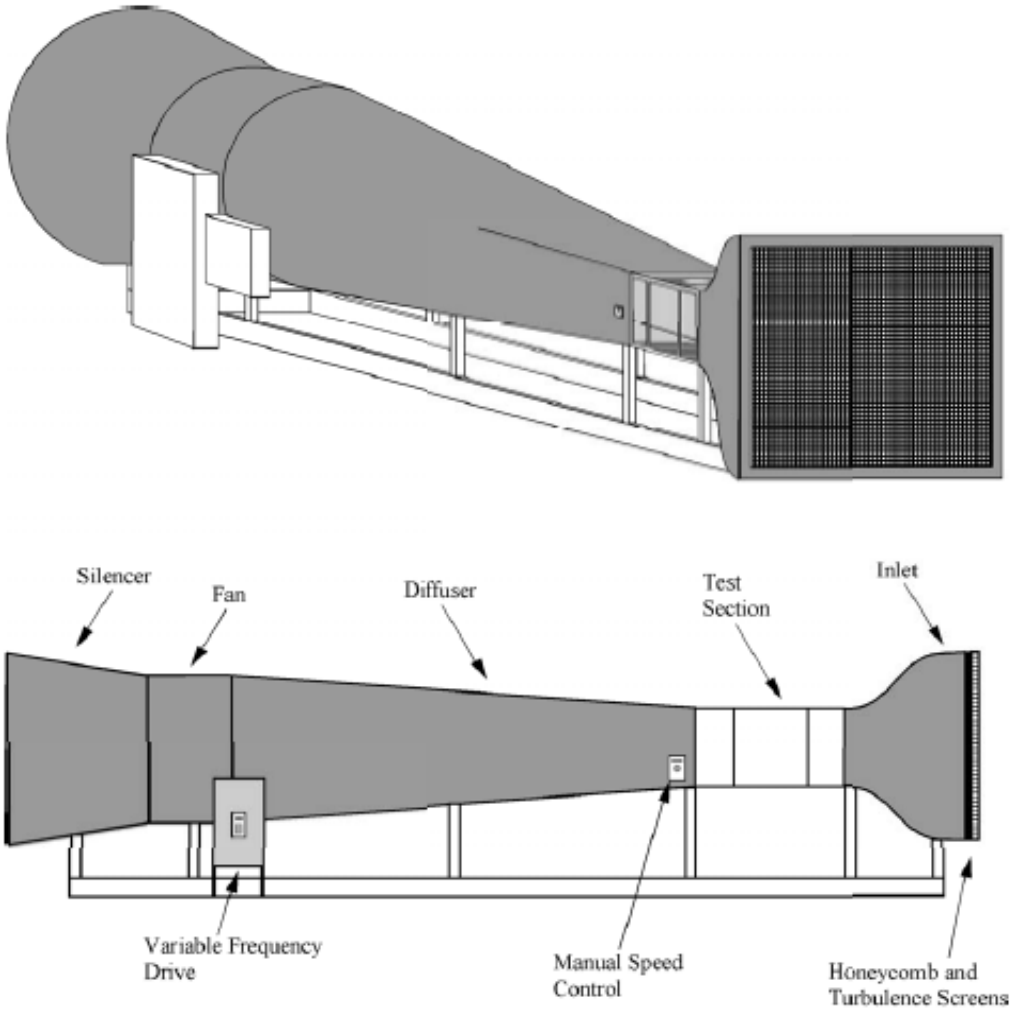

Fig. 2.2 Low-turbulence, subsonic, 3 × 4 wind tunnel, after Lee.[18]

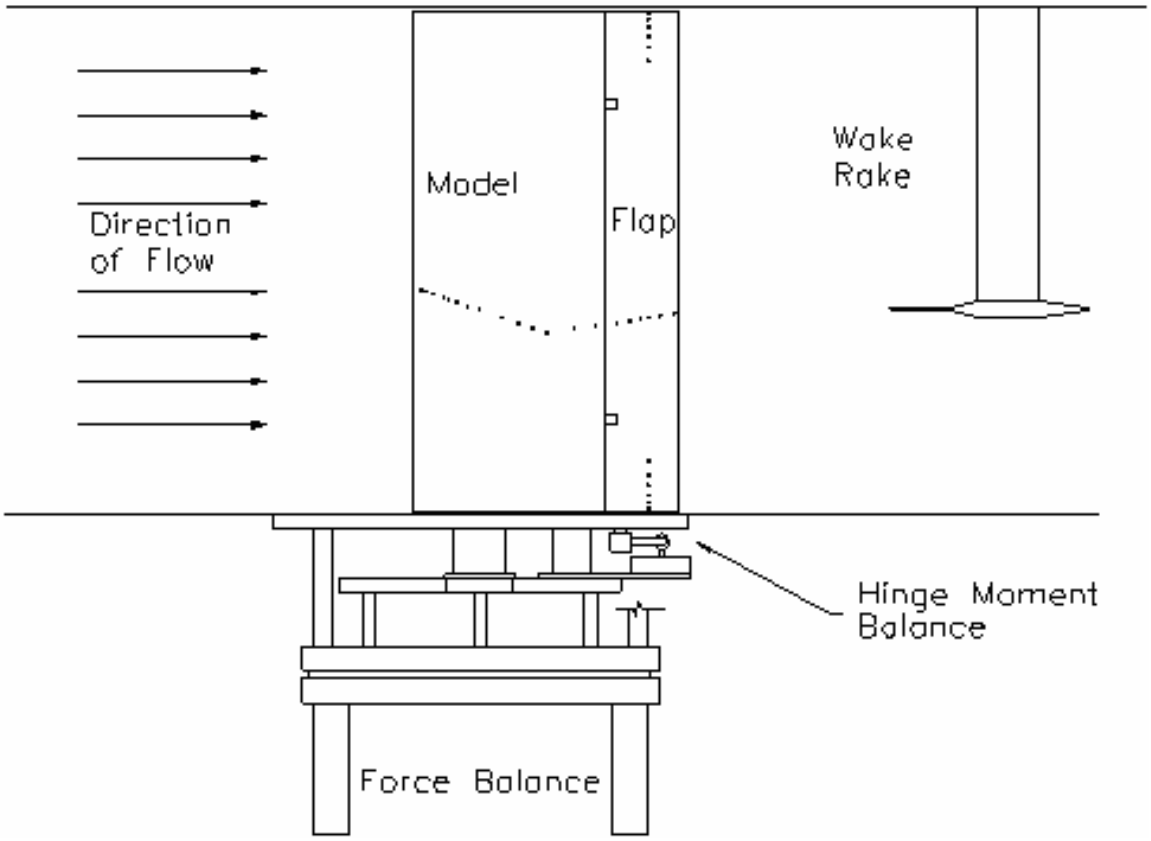

Fig. 2.3 Schematic of experimental setup, adapted from Lee.[18]

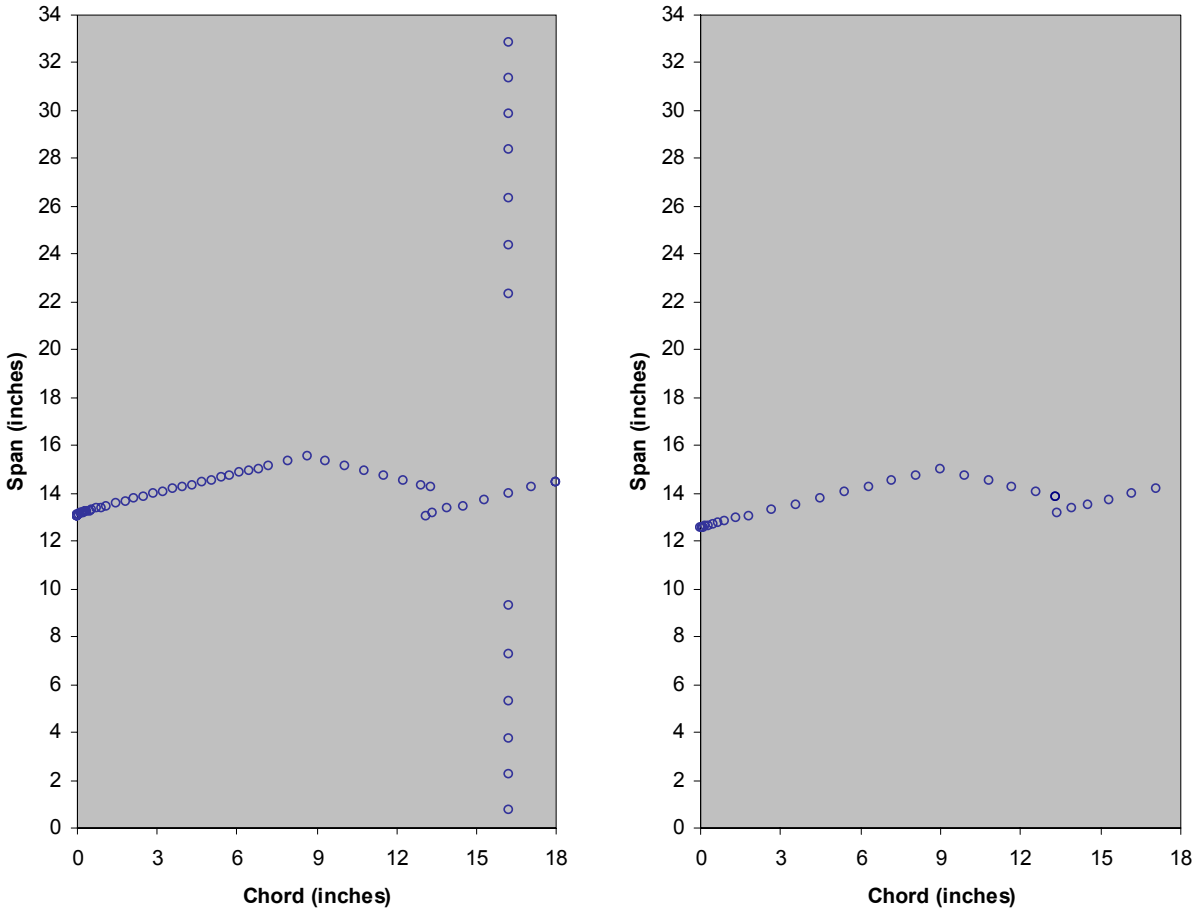

Fig. 2.4 Pressure tap locations of NACA 3415 model.

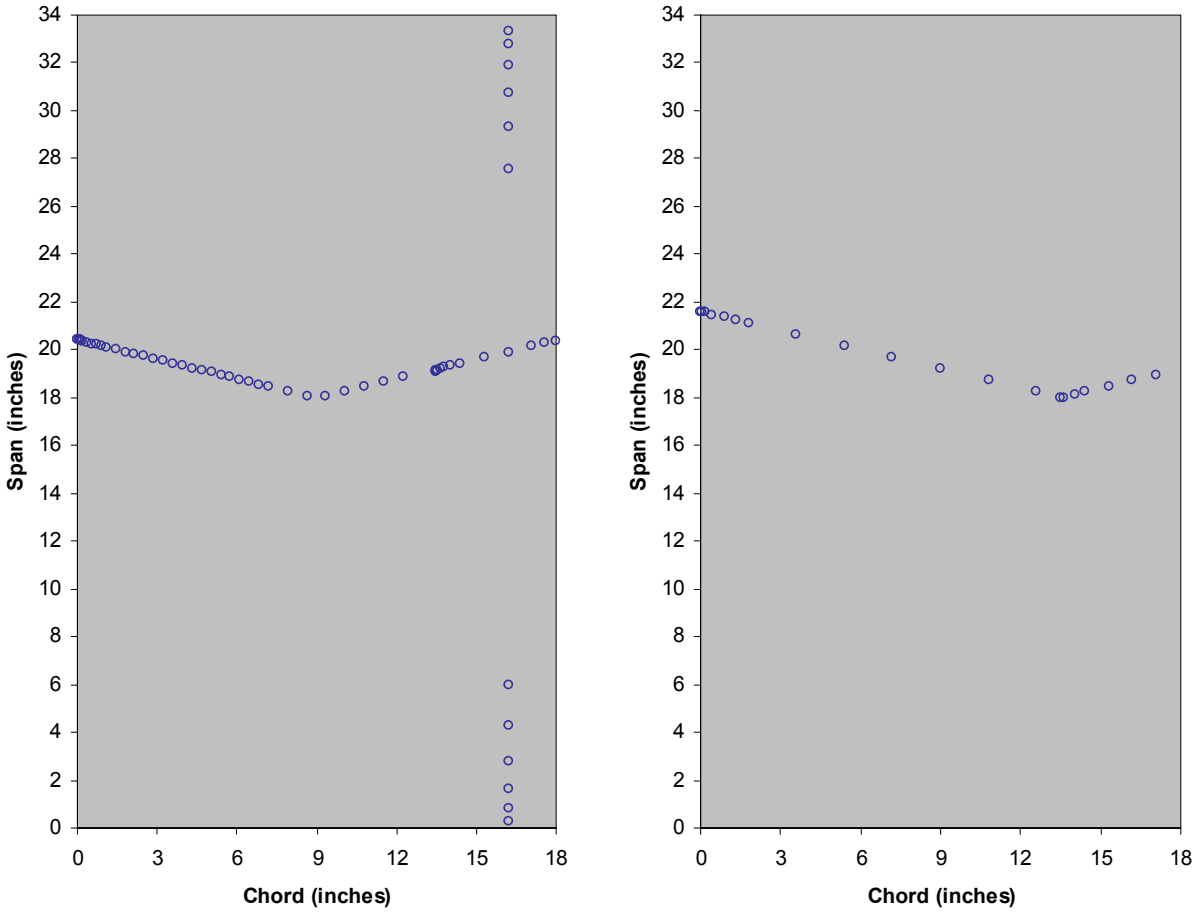

Fig. 2.5 Pressure tap locations of NACA 23012 model.

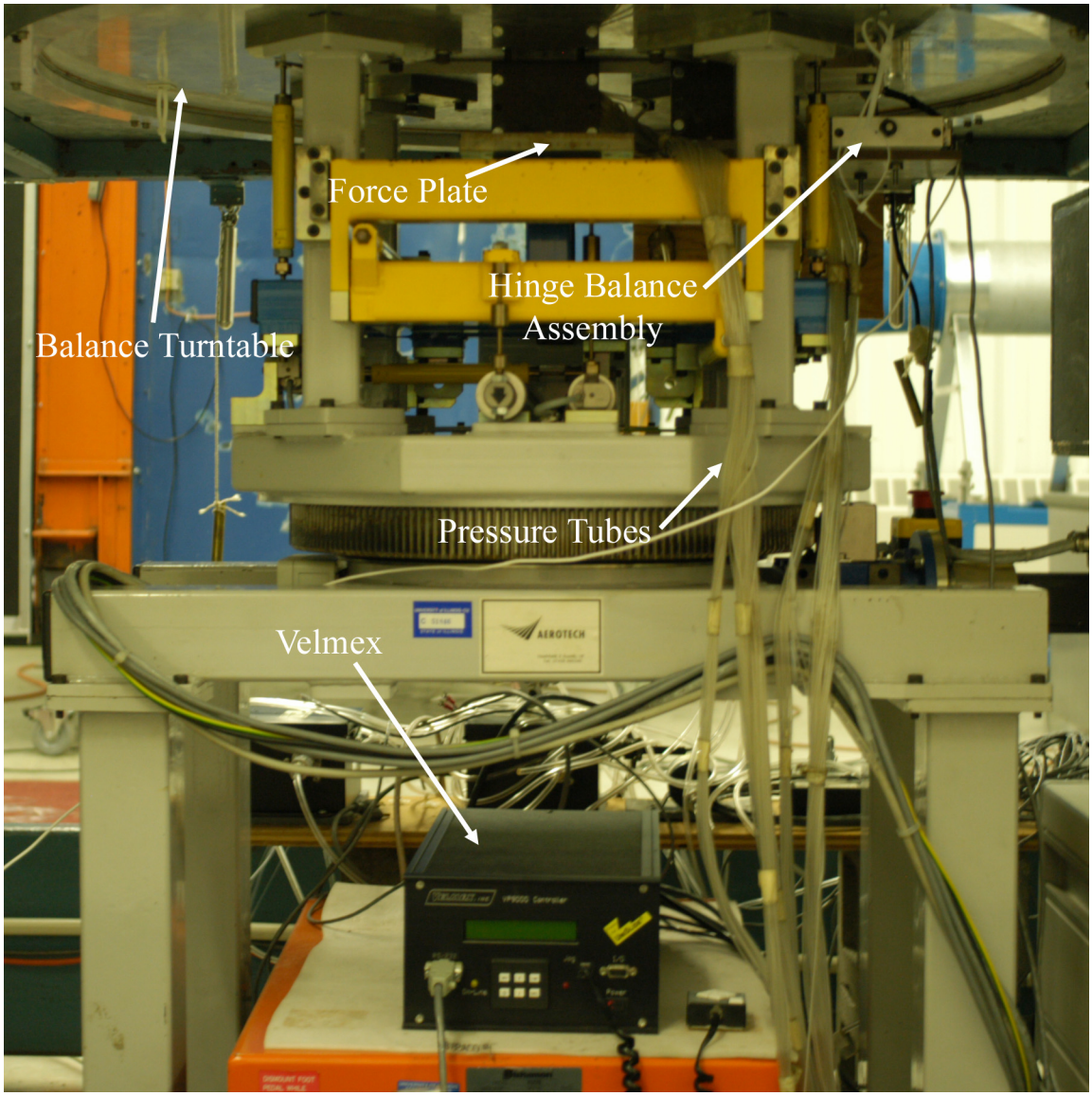

Fig. 2.6 Three-component balance.

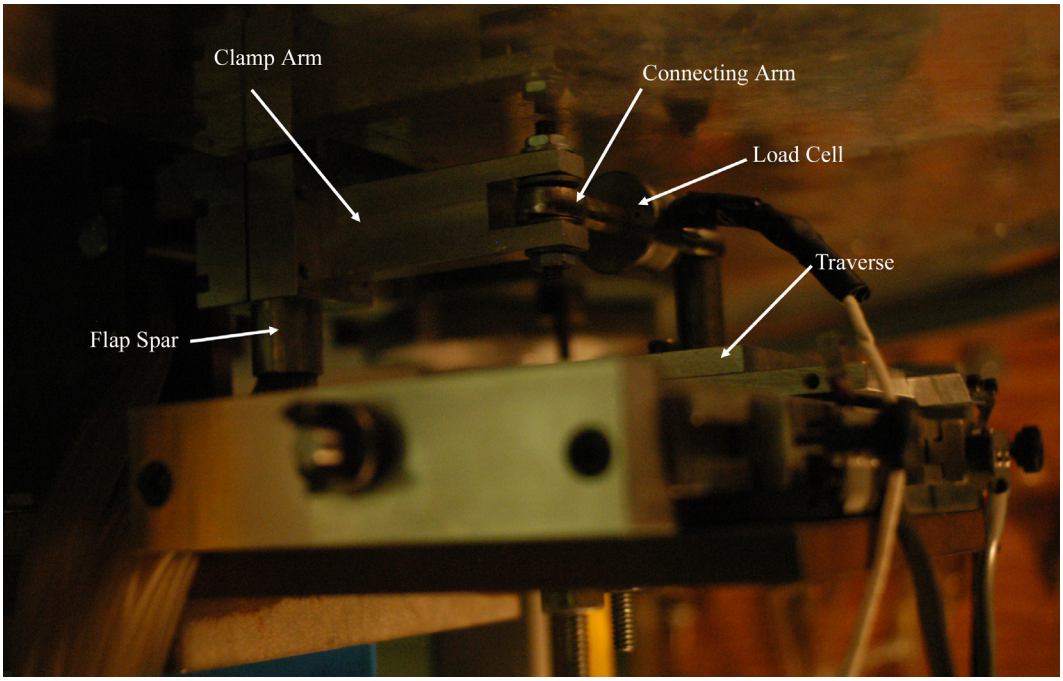

Fig. 2.7 Flap hinge balance assembly.

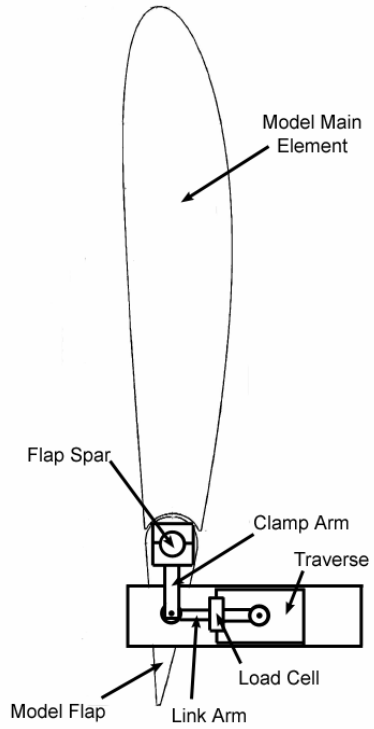

Fig. 2.8 Flap hinge balance assembly schematic.

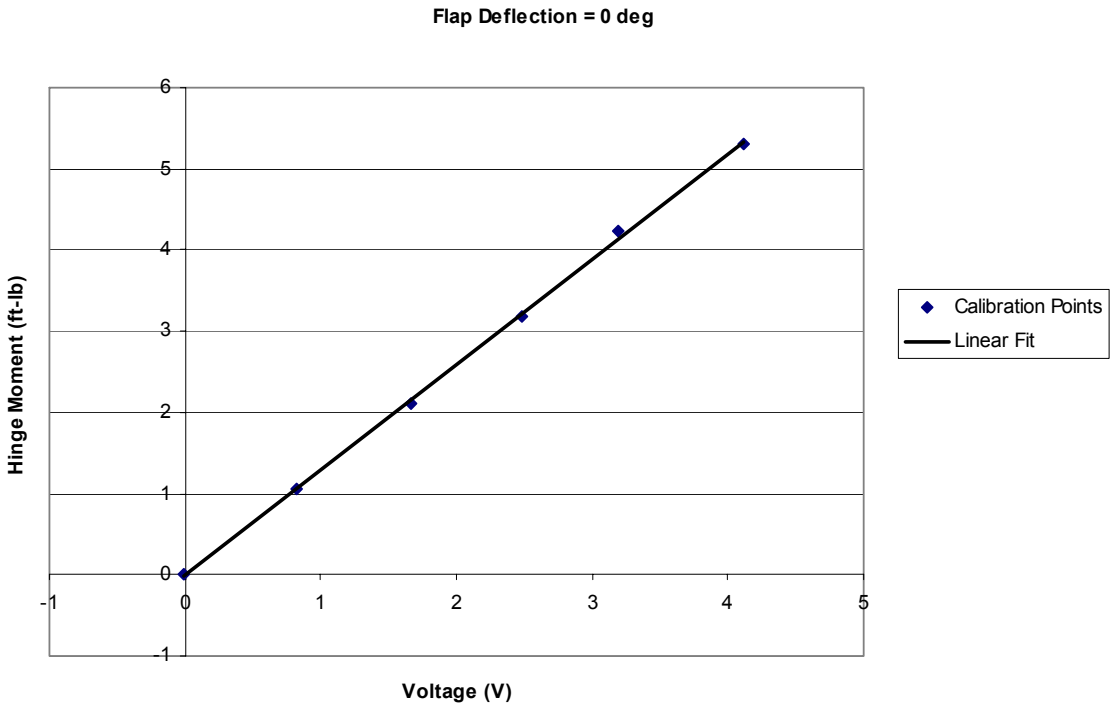

Fig. 2.9 NACA 23012 flap load cell calibration curve for $\delta_f = 0°$.

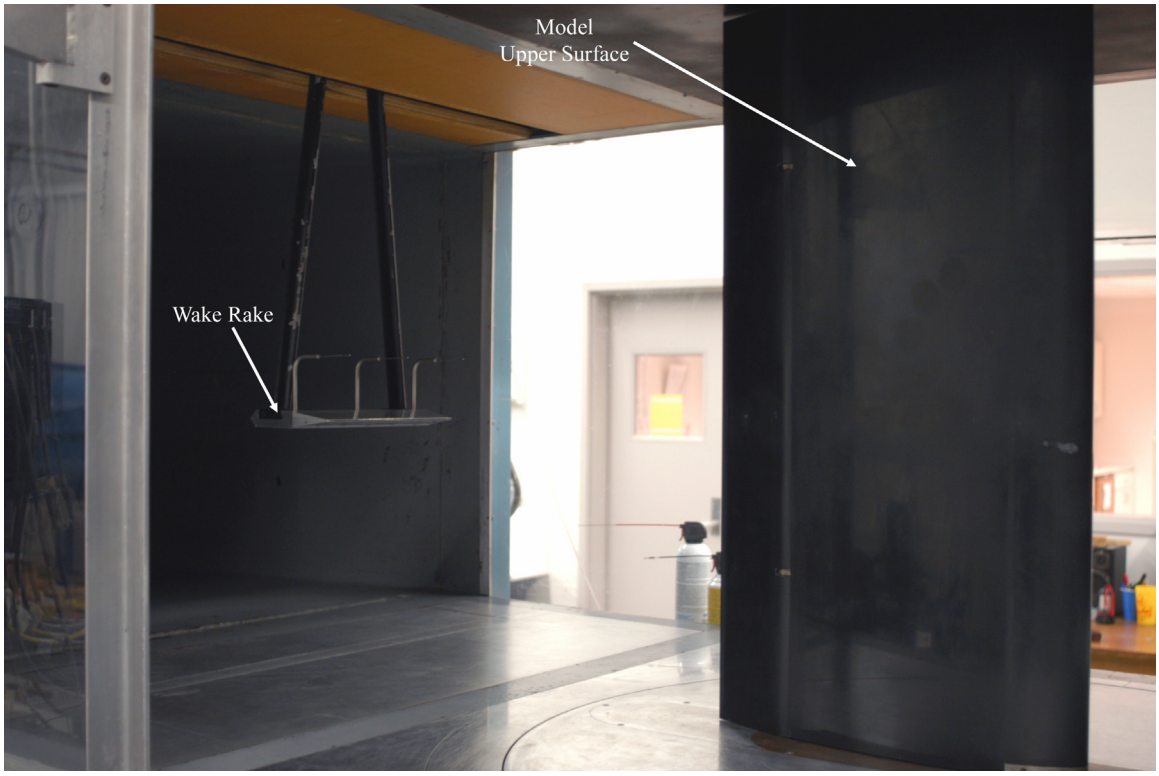

Fig. 2.10 Wake rake and NACA 3415 model upper surface in test section.

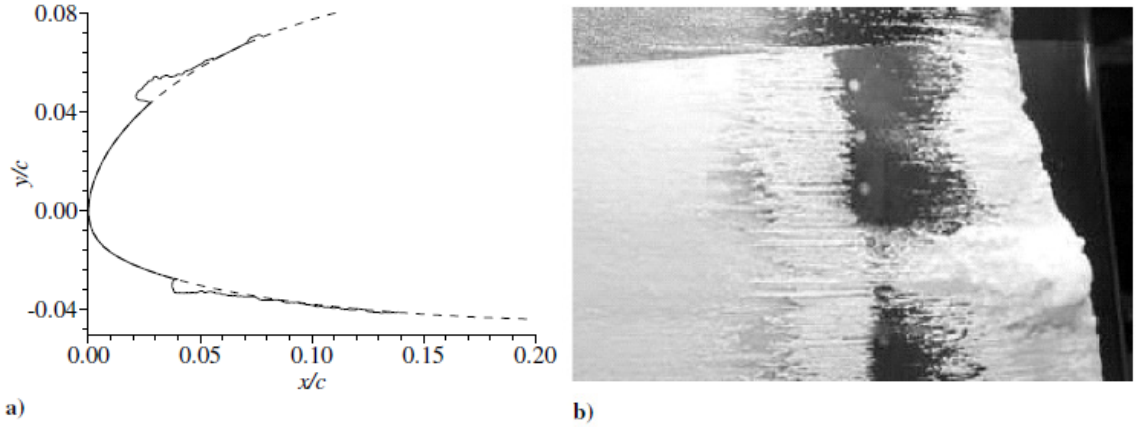

Fig. 2.11 Cold hold runback icing on proprietary business jet-type airfoil, after Whalen et al.[20]

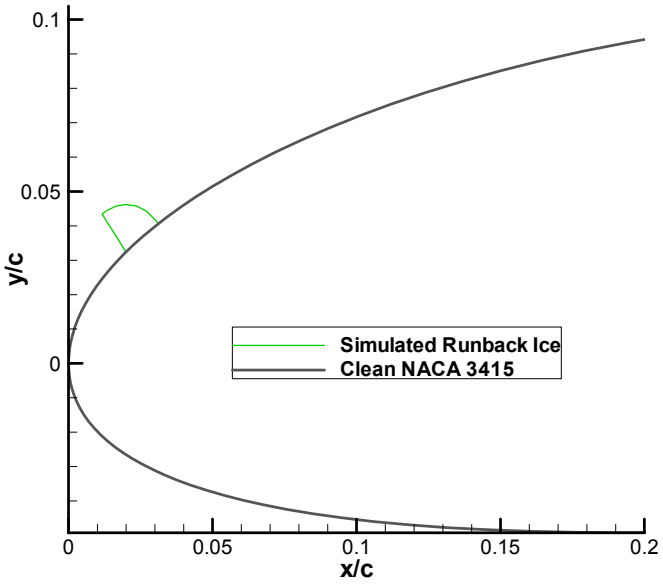

Fig. 2.12 Schematic of quarter-round glaze ice simulation on NACA 3415.

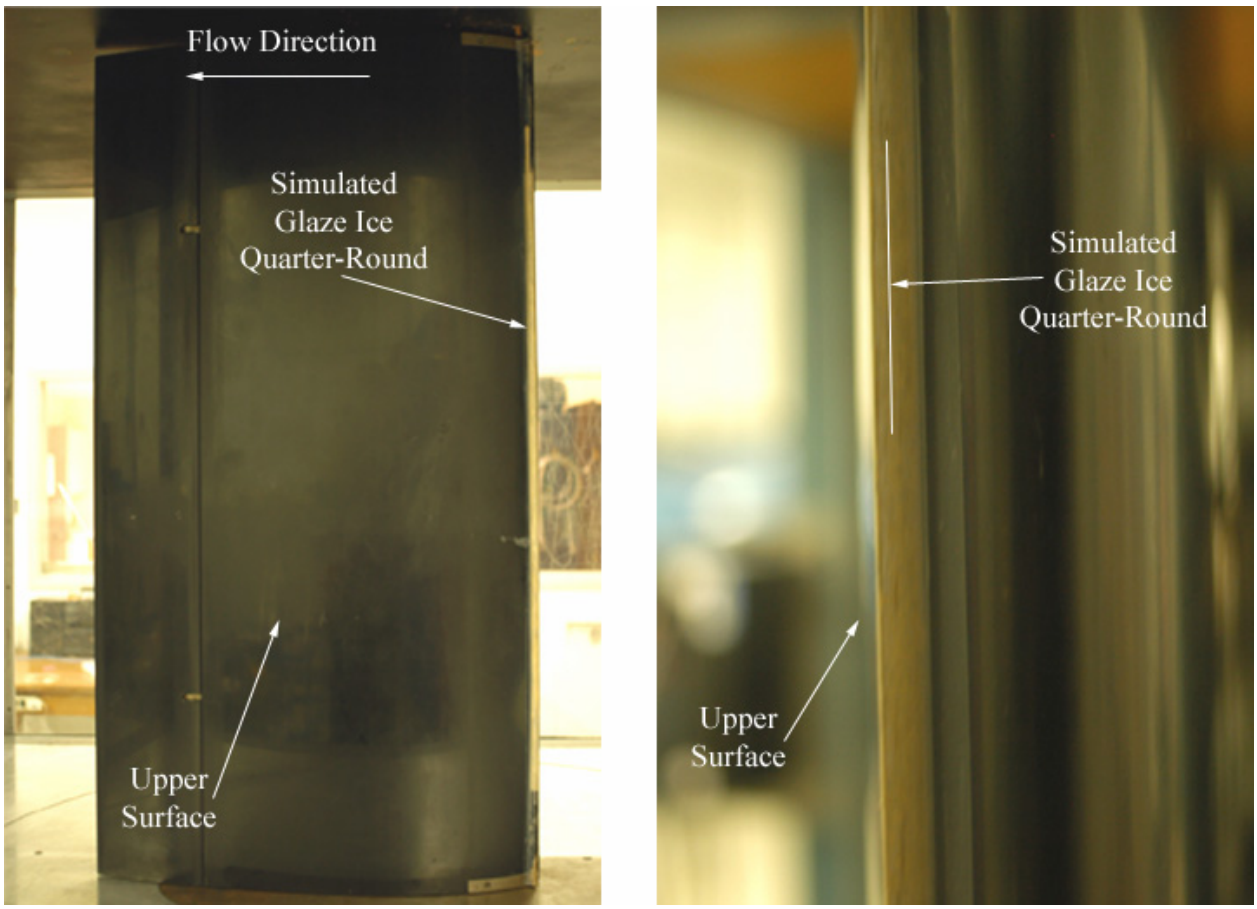

a) b)

Fig. 2.13 Simulated glaze ice on NACA 3415 model, a) full view; b) detail view.

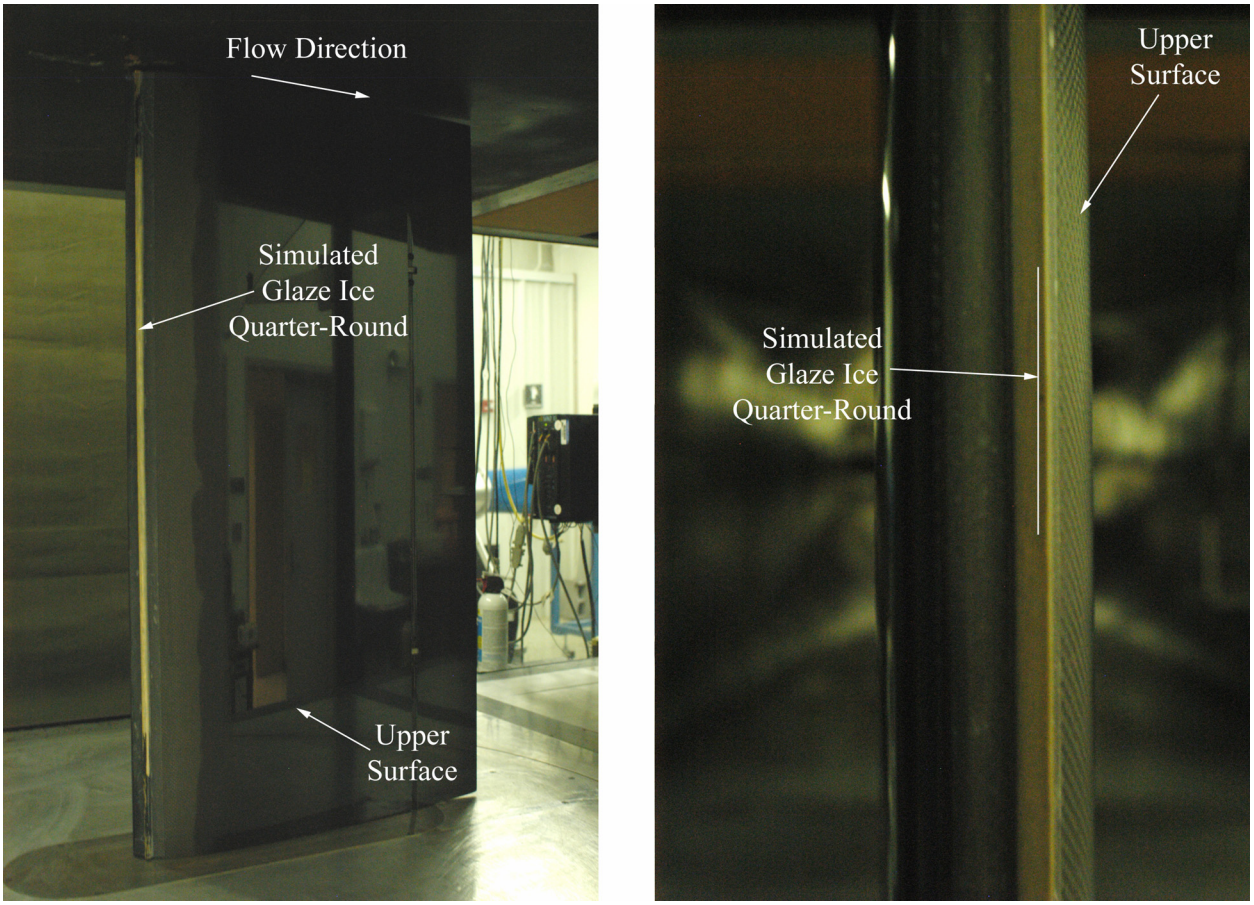

a) b)

Fig. 2.14 Simulated glaze ice on NACA 23012 model, a) full view; b) detail view.

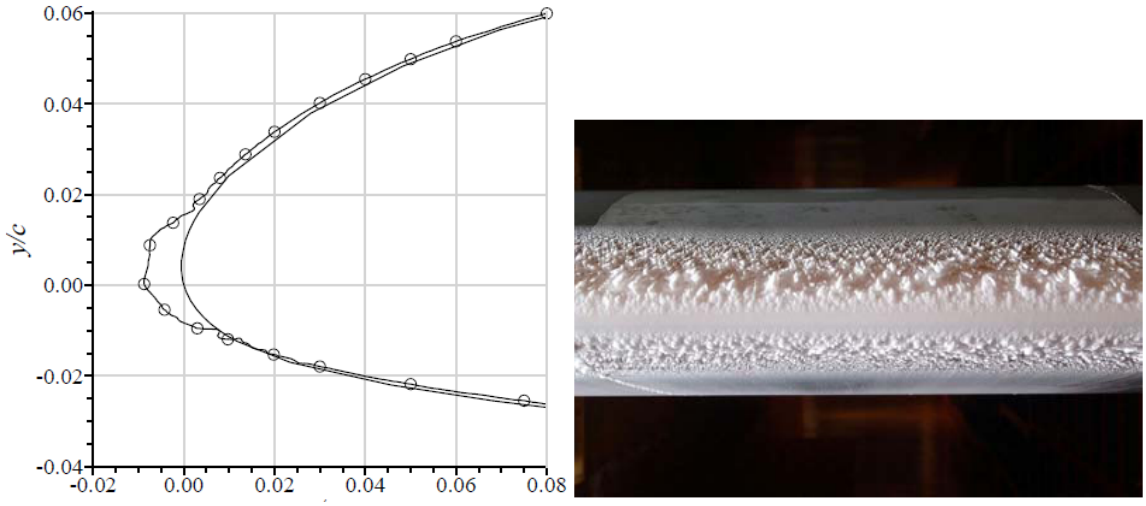

Fig. 2.15 EG1125 rime-ice shape on NACA 23012, after Broeren et al.[22]

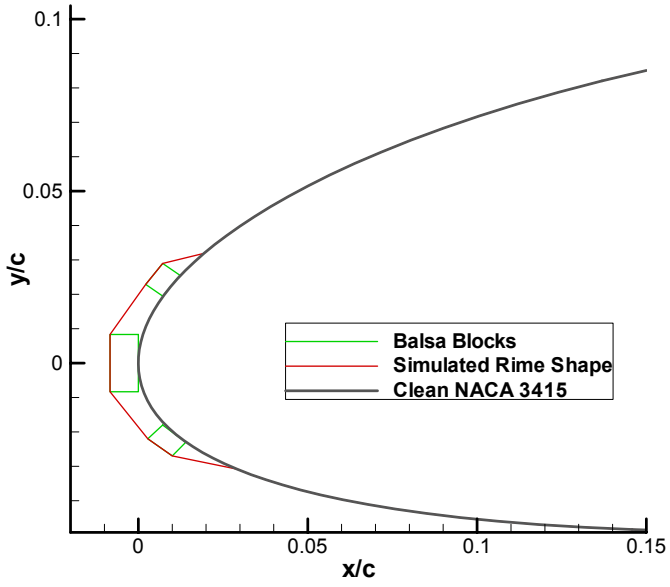

Fig. 2.16 Schematic of rime ice simulation on NACA 3415.

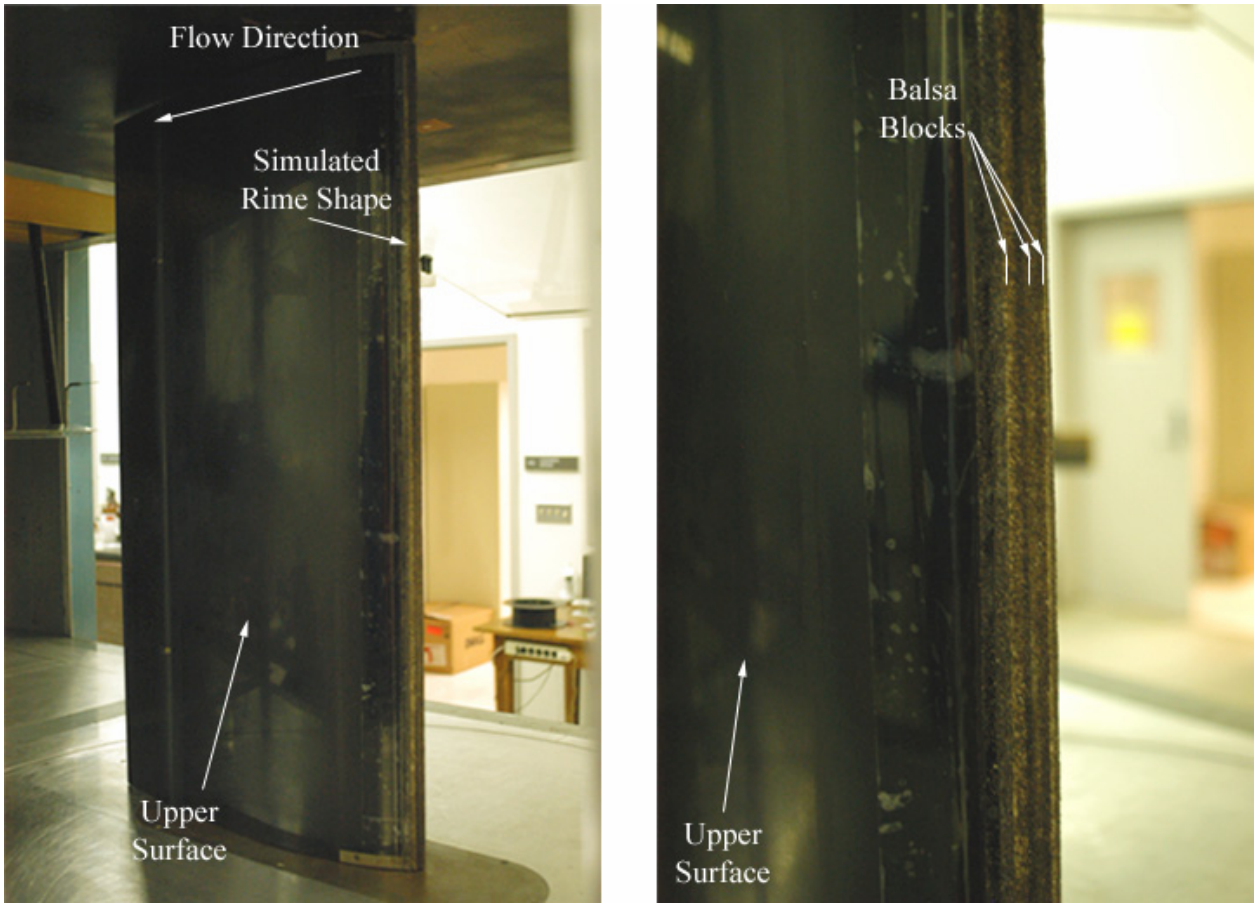

a) b)

Fig. 2.17 Simulated rime ice on NACA 3415 model, a) full view; b) detail view.

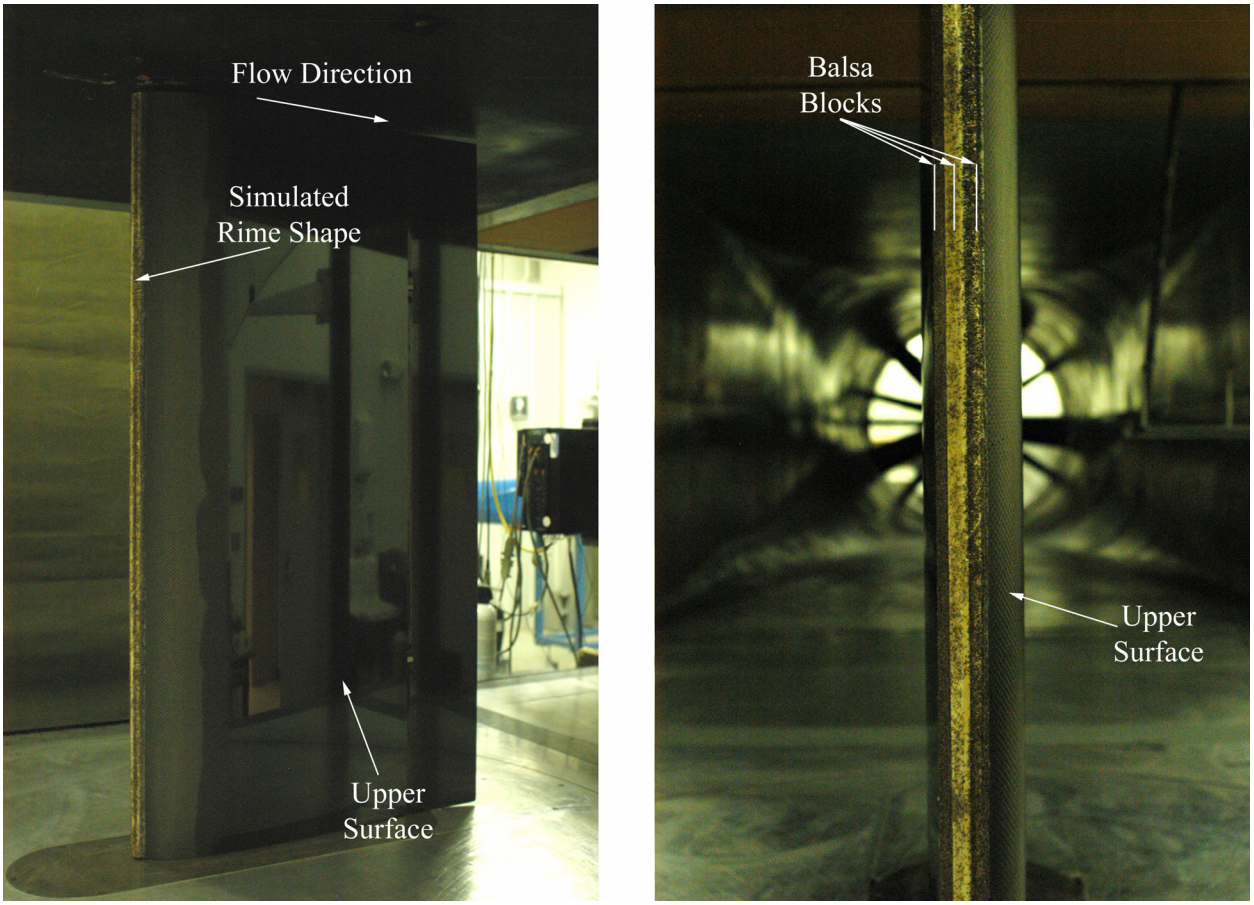

a) b)

Fig. 2.18 Simulated rime ice on NACA 23012 model, a) full view; b) detail view.

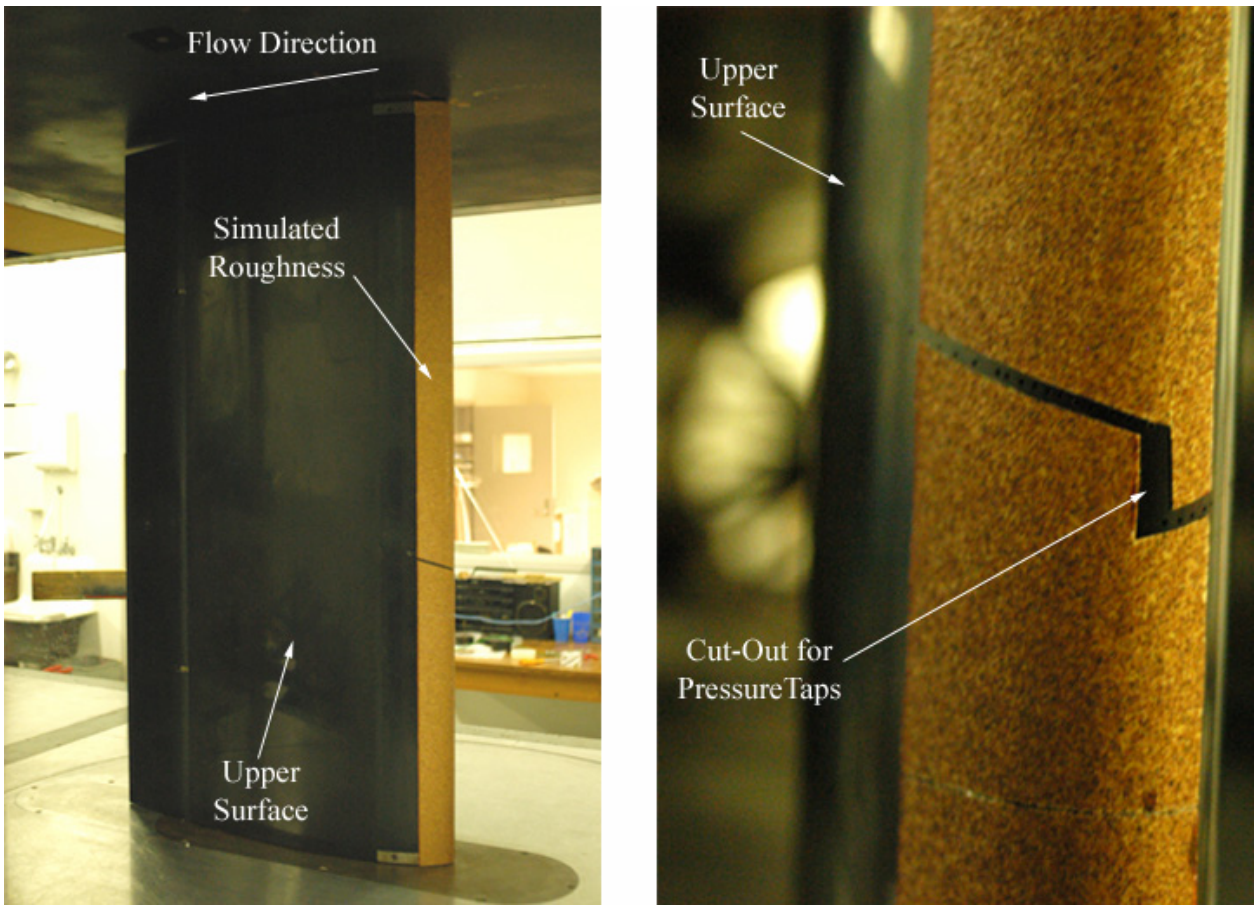

a) b)

Fig. 2.19 80-grit distributed leading-edge roughness on NACA 3415 model, a) full view; b) detail view.

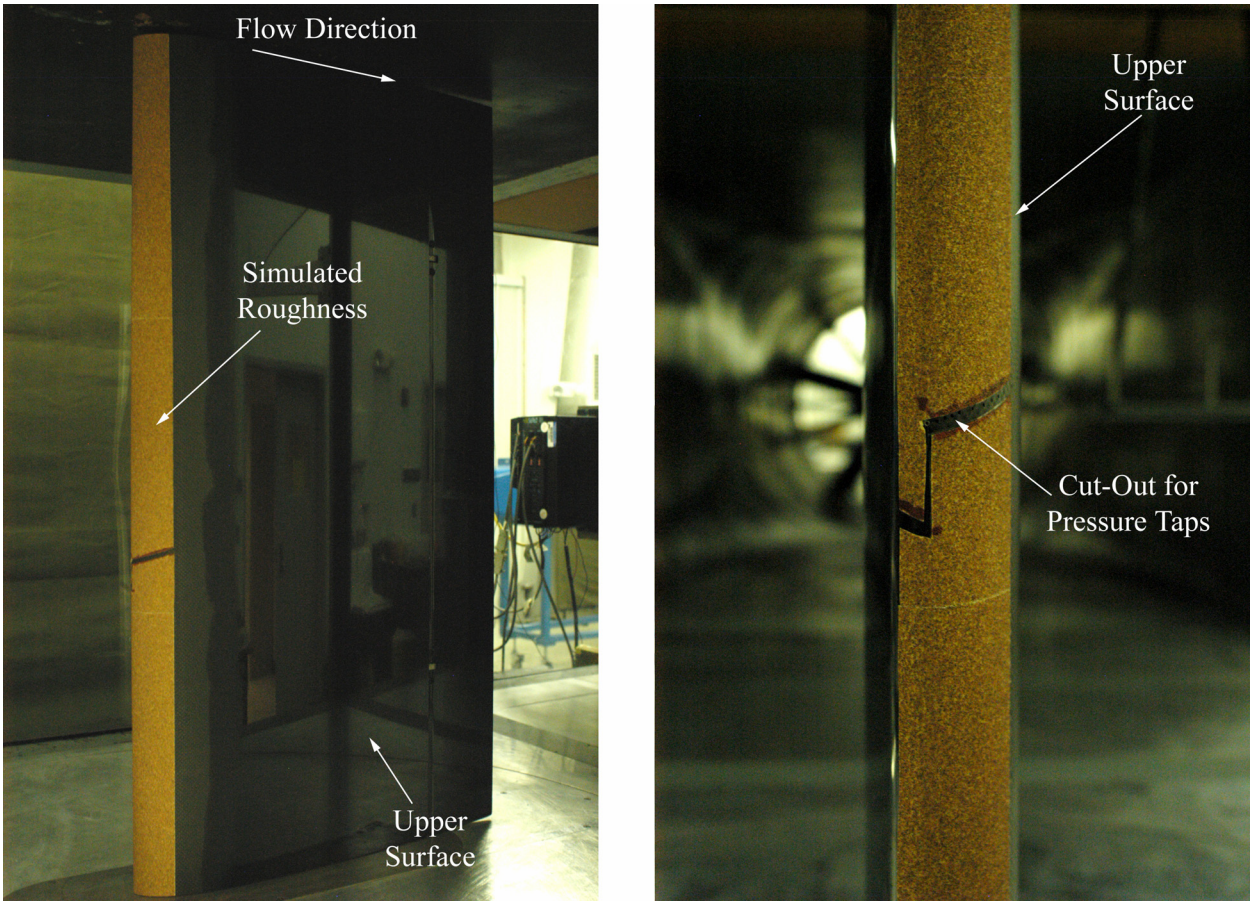

a) b)

Fig. 2.20 80-grit distributed leading-edge roughness on NACA 23012 model, a) full view; b) detail view.

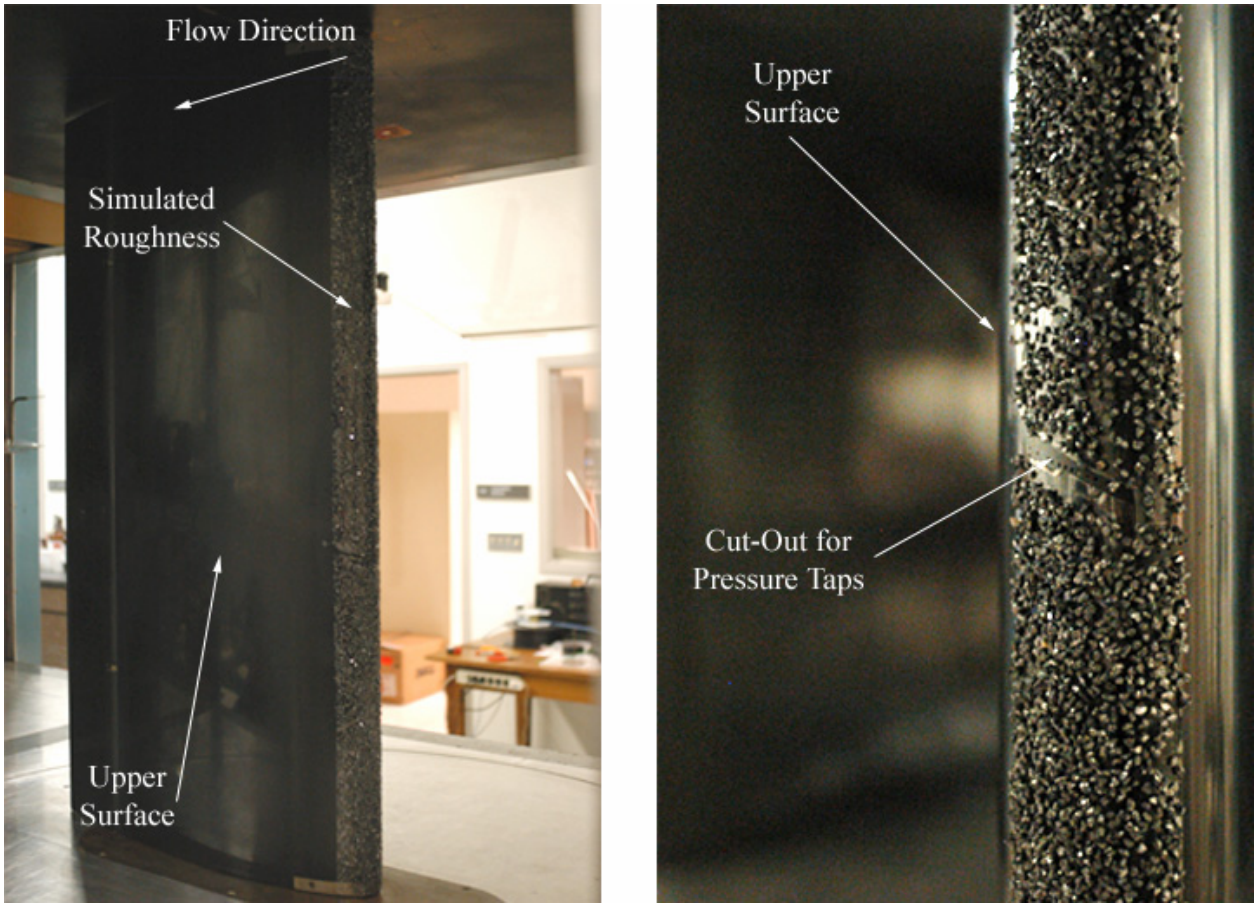

a) b)

Fig. 2.21 14-grit distributed leading-edge roughness on NACA 3415 model, a) full view; b) detail view.

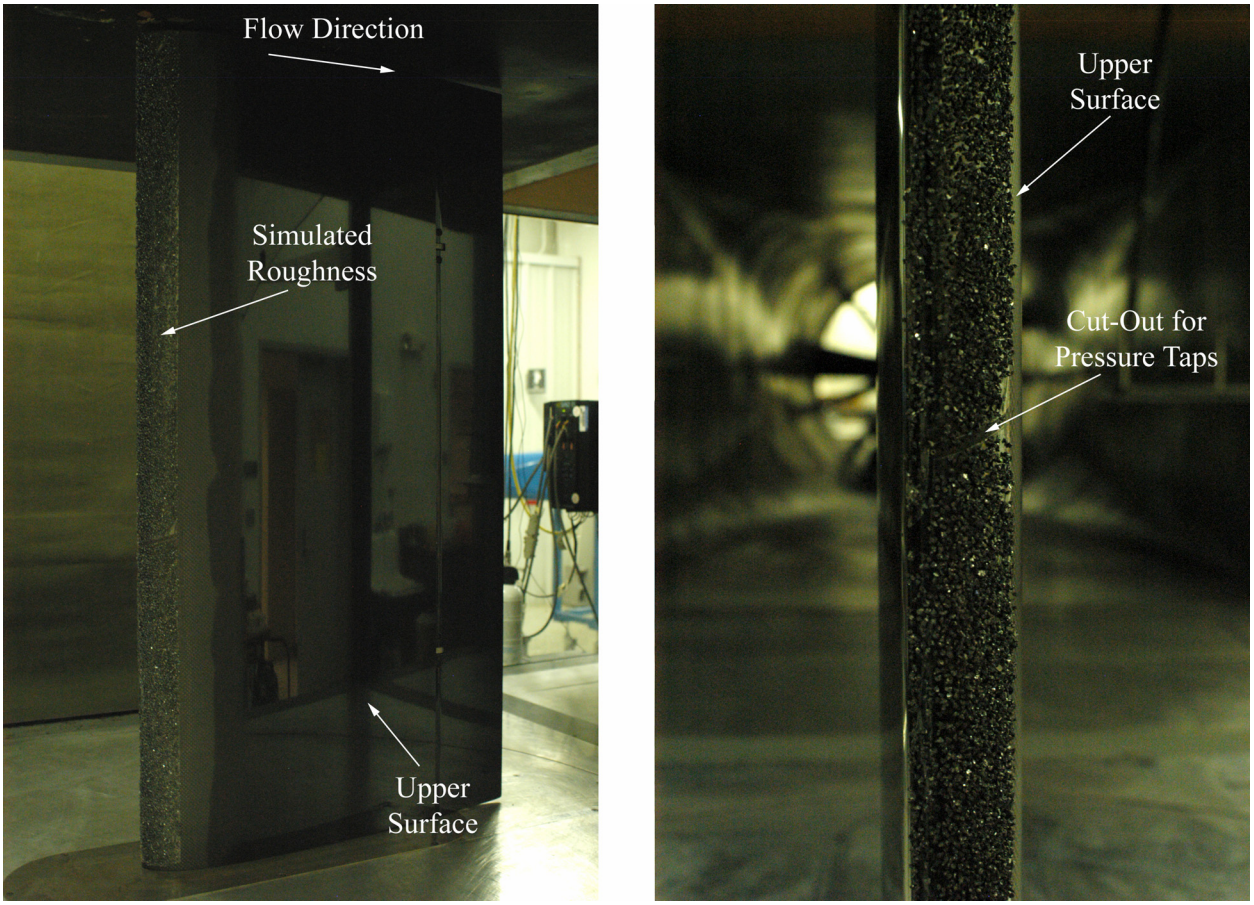

a) b)

Fig. 2.22 14-grit distributed leading-edge roughness on NACA 23012 model, a) full view; b) detail view.

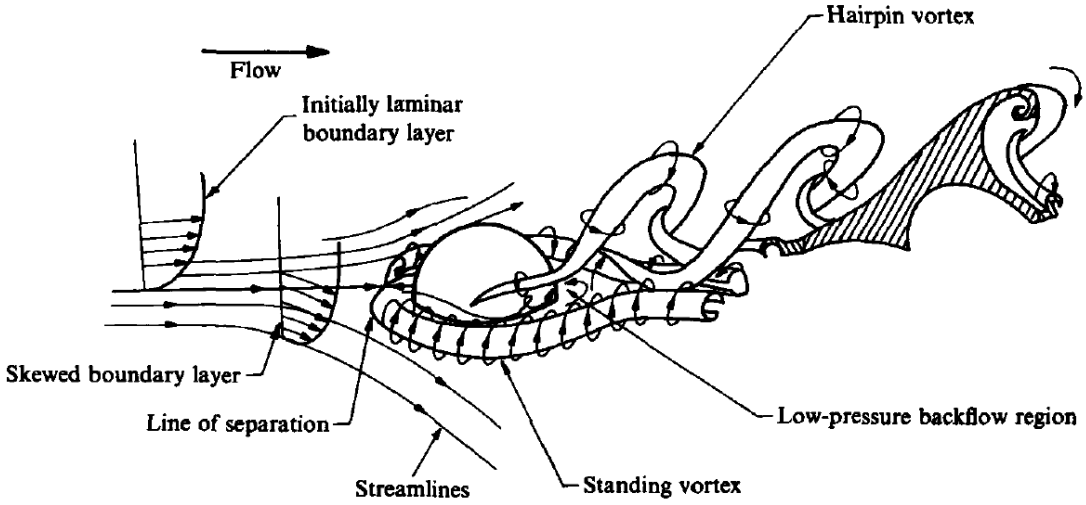

Fig. 2.23 Schematic of flow characteristics past a hemisphere, after Alcar and Smith.[27]

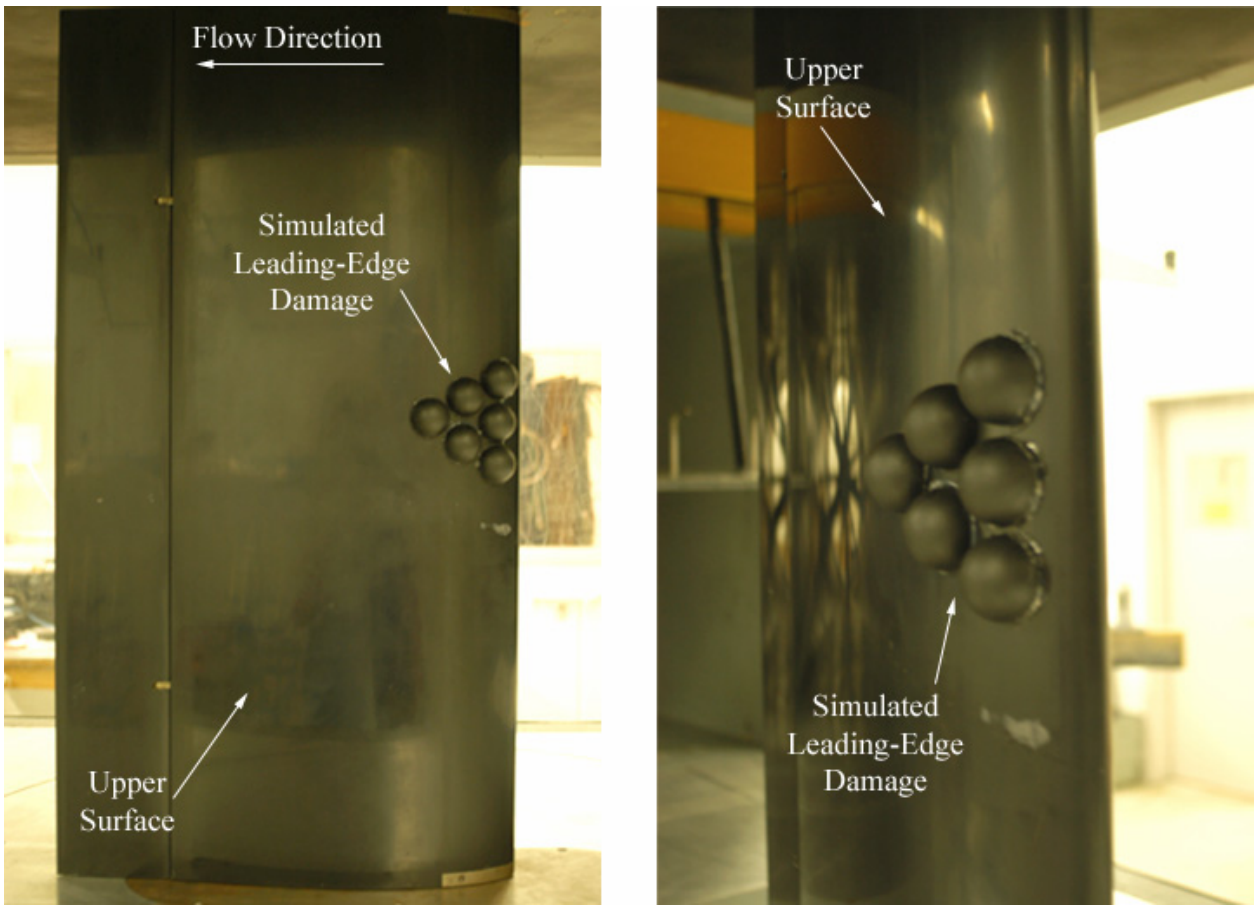

a) b)

Fig. 2.24 Simulated leading-edge damage on NACA 3415 model, a) full view; b) detail view.

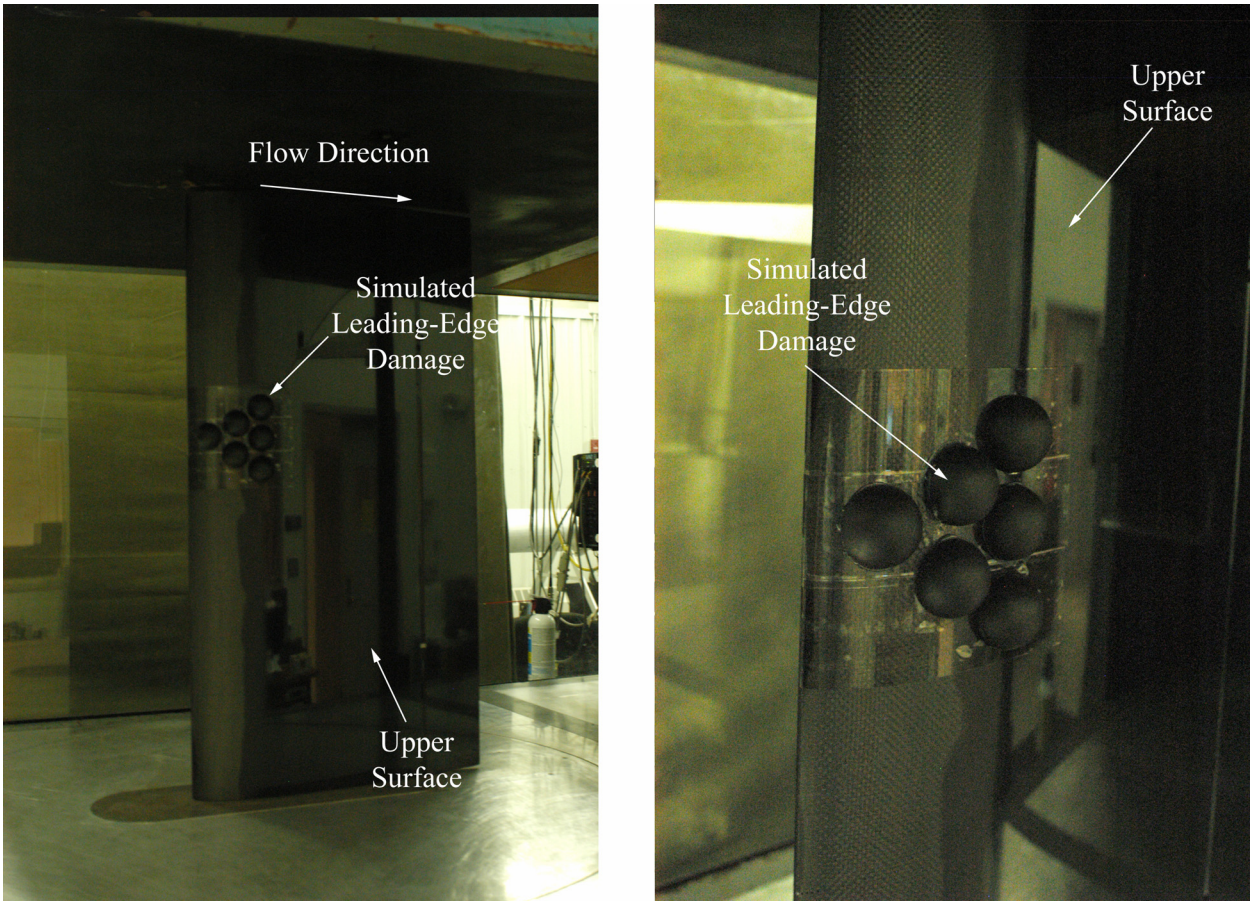

a) b)

Fig. 2.25 Simulated leading-edge damage on NACA 23012 model, a) full view; b) detail view.

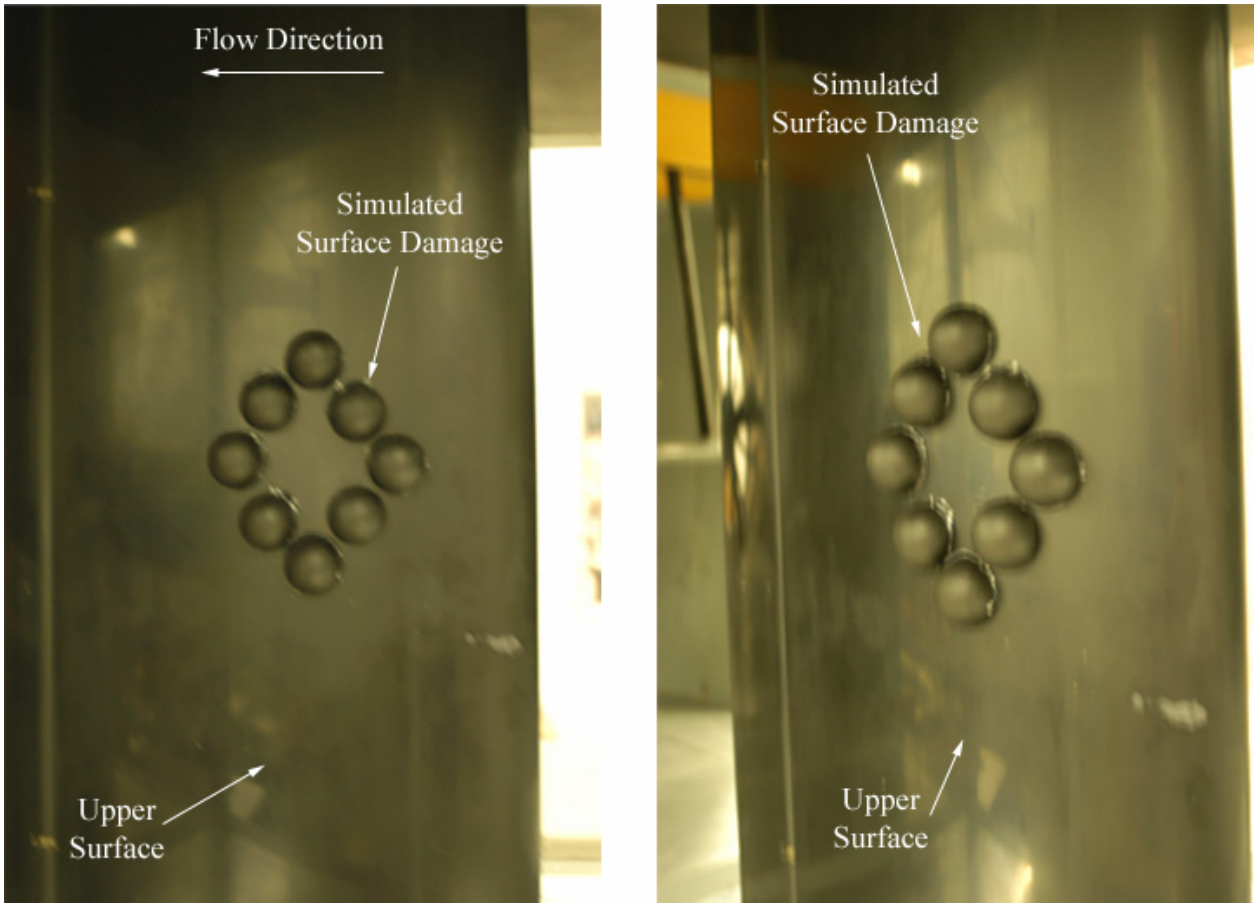

a) b)

Fig. 2.26 Simulated upper-surface damage on NACA 3415 model, a) full view; b) detail view.

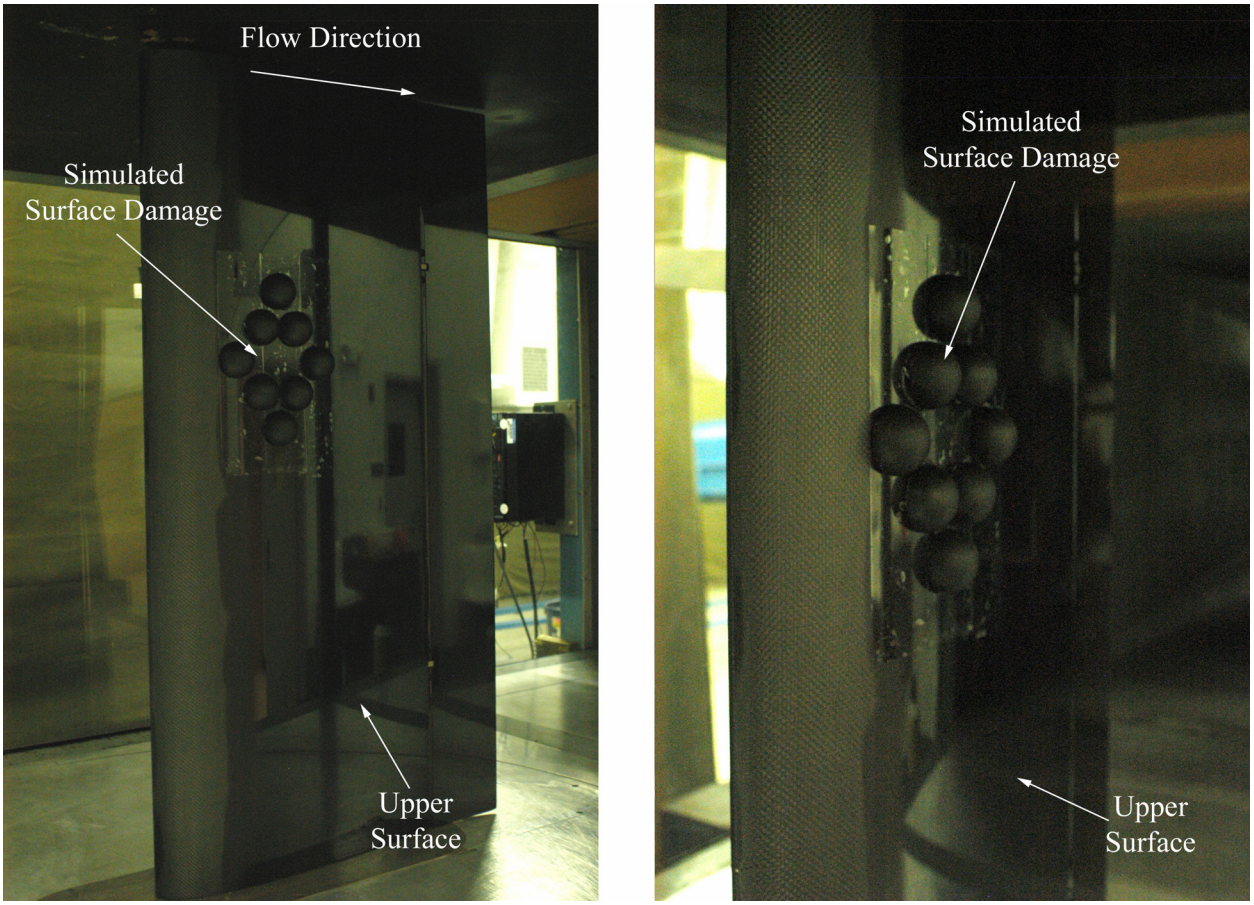

a) b)

Fig. 2.27 Simulated upper-surface damage on NACA 23012 model, a) full view; b) detail view.

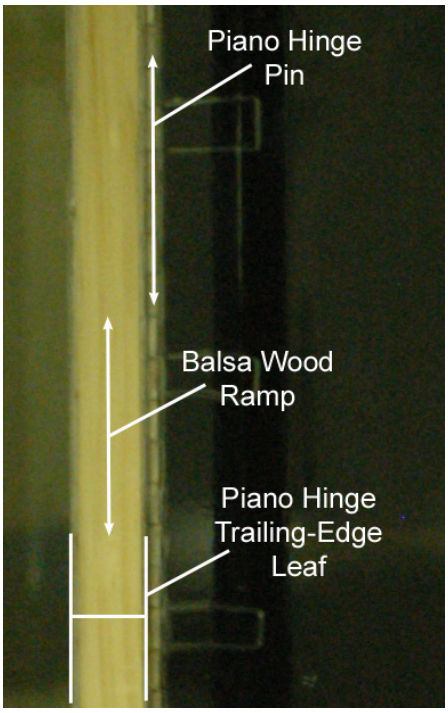

Fig. 2.28 Trim tab upper surface with balsa wood ramp.

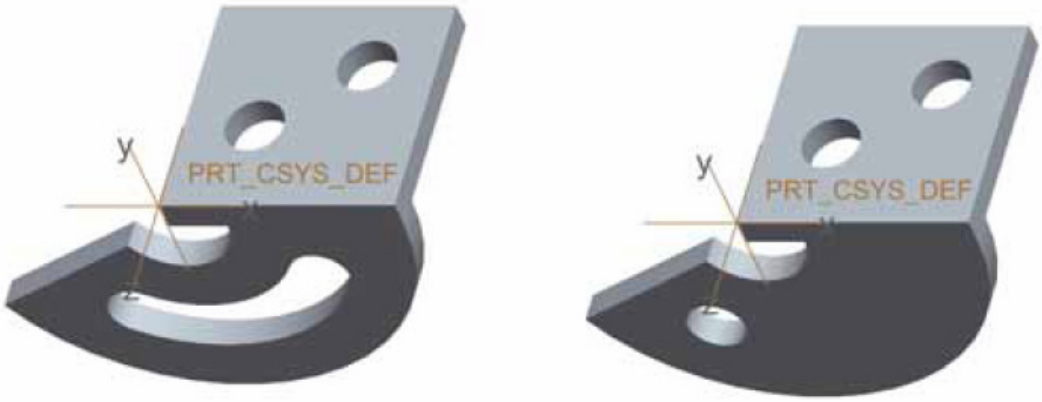

Fig. 2.29 Trim tab hinge mounting brackets.

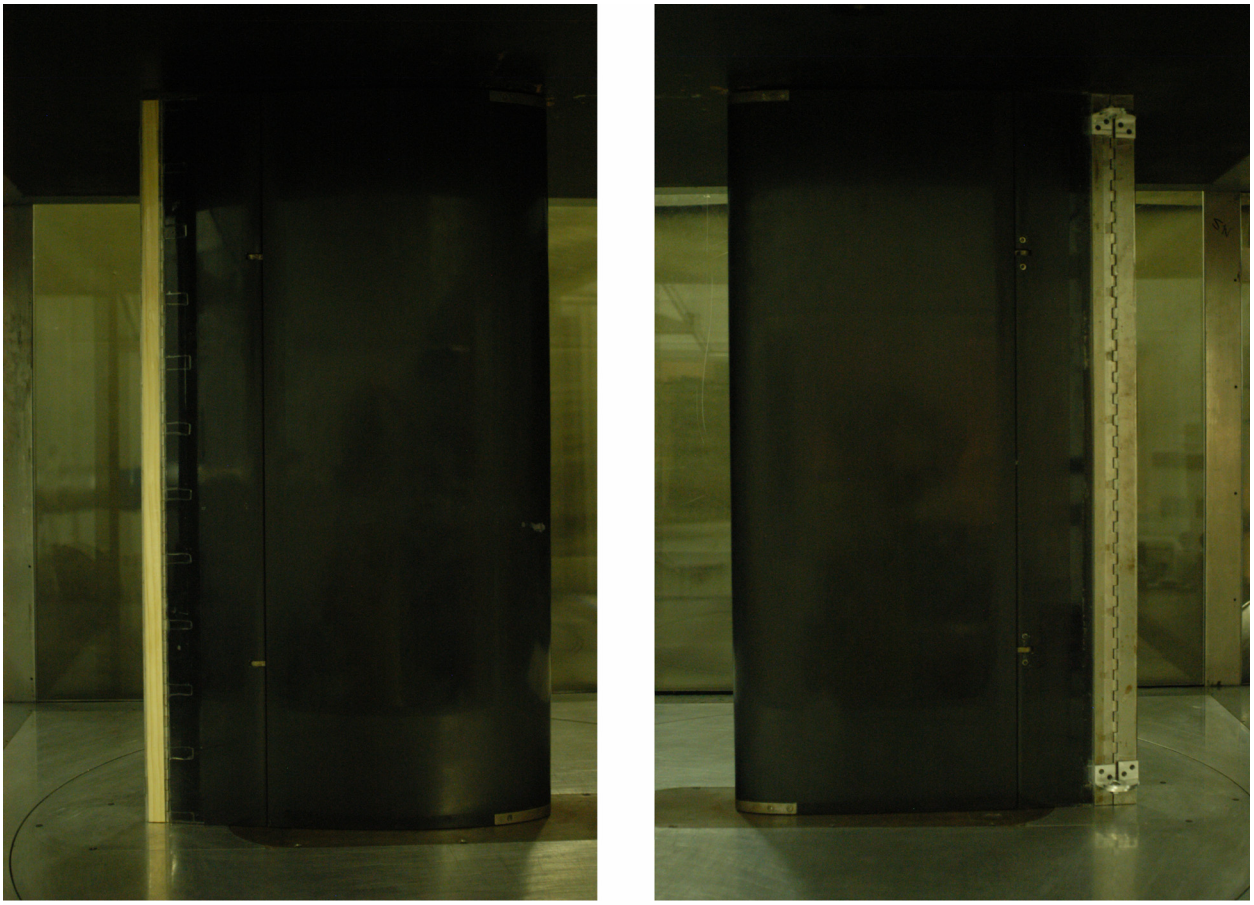

Upper Surface Lower Surface

Fig. 2.30 NACA 3415 model with trim tab installed.

Chapter 3

Results and Discussion

In this section, the clean data of the current investigation are compared to clean data from previous validated model installations in order to provide validation of the current test. Also, the unsteady hinge-moment parameter, $C_{h,StDev}$, obtained from the hinge balance measurement, is presented as a function of trim tab deflection. Using these data, the effects of trim tab deflection on hinge moment unsteadiness are identified. Comparisons of aerodynamic performance parameters for the simulated contamination and clean model configurations are presented.

The C_l and C_m used in these comparisons were calculated from the three-component balance measurements. The C_l and C_m obtained from integrating the surface pressures were used for comparison purposes only. The C_d values presented in these comparisons were calculated from the wake pressure data. The C_h and $C_{h,StDev}$ were calculated from the hinge balance measurements. Various C_p distributions are also presented for flow diagnostic purposes. Surface oil-flow visualization results are also presented for the clean and simulated damage configurations and key flowfield effects are identified.

3.1 NACA 3415 Experimental Validation

Validation of the NACA 3415 model installation was performed by taking measurements of the clean NACA 3415 section and comparing them to a previous installation, which had

already been proven in Whalen et al.[28] to provide reliable measurements for the same NACA 3415 model being used in the current experiment. For the initial validation runs, the flap gap was sealed using book tape. The flap gap was sealed to match the setup used by Whalen, who sealed the flap gap in an effort to minimize leakage. After the initial validation tests were complete, the flap gap seal was removed for the remainder of the test. Inspection of the C_l, C_d, and C_m plots in Fig. 3.1 show that there was no significant difference between the current NACA 3415 model data and the previous data of Whalen et al.[28]

3.2 NACA 23012 Experimental Validation

Validation of the NACA 23012 model installation was performed by taking measurements of the clean NACA 23012 section and comparing them to a previous installation, which had already been proven in Lee[18] to provide reliable measurements for the same NACA 23012 model being used in the current test. Inspection of the C_l, C_d, and C_m plots in Fig. 3.2 shows that there were no significant differences between the performance of the current model installation and the previous installation.

3.3 Clean NACA 3415 Results

Before testing any cases where simulated contamination was present on the model (without the trim tab), the baseline clean case was tested. The clean NACA 3415 performance is shown in Fig. 3.3 and Fig. 3.4 as a function of flap deflection at both Reynolds numbers tested. As seen from the clean data, the large increase in $C_{h,StDev}$ occurs around the same angle of attack as $C_{l,max}$. The rapid rise in the $C_{h,StDev}$ level at $C_{l,max}$ is indicative of flow separation over the flap.

Using the C_p distribution, it is possible to identify chordwise locations of separated flow. Figure 3.5 shows C_p distributions of the clean model with a flap setting of 0° at increasing angles of attack. From Fig. 3.5, at α = 5°, 8°, and 12° the flowfield appears to be fully attached. At α = 15°, just past the angle of attack of $C_{l,max}$, a region of constant, negative pressure downstream of $x/c \approx 0.40$ indicates boundary-layer separation across the upper surface, rapidly moving upstream from the trailing edge with increased angle of attack. The separated flow over the flap also suggests that separation is the cause of the rapid rise in $C_{h,StDev}$ at $C_{l,max}$.

3.3.1 Effect of Flap Deflection

While the effect of high lift devices on performance characteristics of airfoil sections have previously been studied in great depth, it was important to identify the effect of flap deflection on the unsteady hinge-moment parameter, $C_{h,StDev}$. From Fig. 3.3 and Fig. 3.4, as expected, a positive flap deflection resulted in higher values of C_l and a lower stall angle of attack. At a Reynolds number of 1.8×10^6, the clean NACA 3415 model with $\delta_f = 5°$ increased $C_{l,max}$ by 0.176 (12.4%) and reduced the angle of attack at which it occurs by 0.5°. Deflecting the flap to $\delta_f = 10°$ from $\delta_f = 0°$ increased $C_{l,max}$ by 0.315 (22.1%) and reduced the angle of attack at which it occurs by 0.5°. From Fig. 3.3 and Fig. 3.4, a negative flap deflection resulted in decreased values of C_l and a higher stall angle of attack. At a Reynolds number of 1.8×10^6, the clean NACA 3415 model with $\delta_f = -5°$ decreased $C_{l,max}$ by 0.187 (13.2%) and increased the angle of attack at which it occurs by 0.5°. Deflecting the flap to $\delta_f = -10°$ from $\delta_f = 0°$ decreased $C_{l,max}$ by 0.330 (23.2%) and increased the angle of attack at which it occurs by 1.5°.

Inspection of the $C_{h,StDev}$ plots in Fig. 3.3 and Fig. 3.4 reveals that the large increase in $C_{h,StDev}$ occurred at the same angle of attack of $C_{l,max}$ corresponding to the flap setting. From Fig. 3.3, at a Reynolds number of 1.8×10^6 and $\delta_f = 0°$, $C_{l,max}$ occurred at 14.4°, which was the same angle of attack corresponding to the large increase in $C_{h,StDev}$. For $\delta_f = 5°$ and $\delta_f = 10°$, $C_{l,max}$ occurred at an angle of attack of 13.9°, which also corresponded to the angle of attack where the large increase occurred in $C_{h,StDev}$. For $\delta_f = -5°$, the angle of attack of $C_{l,max}$ was 14.8° and for $\delta_f = 10°$, the angle of attack of $C_{l,max}$ was 15.8°, both of which corresponded to the angle of attack where the large increase occurred in $C_{h,StDev}$. Thus, it was shown that the flap hinge moment was sensitive to unsteadiness in the flowfield induced by boundary-layer separation.

3.3.2 Effect of Trim Tab on Unsteady Hinge Moment

While deflection of the trim tab did shift the C_h curve as expected, it did not change the character of the flap $C_{h,StDev}$. Figure 3.6 shows the performance of the clean NACA 3415 model as a function of trim tab deflection and Reynolds number, at a flap setting of 5°. Figure 3.7 shows the performance of the NACA 3415 model with the simulated glaze ice as a function of trim tab deflection and Reynolds number, at a flap setting of 5°. From Fig. 3.6, at a Reynolds number of 1.8×10^6 and $\delta_t = 5°$, the clean NACA 3415 with $\delta_t = 0°$ had a $C_{l,max}$ of 1.66, which occurred at an angle of attack of 13.9°. For $\delta_t = 5°$, $C_{l,max}$ increased by 0.04 (2.4%), and the

angle of attack at which it occurred was reduced by 0.5° from $\delta_t = 0°$. For $\delta_t = -5°$, $C_{l,max}$ decreased by 0.04 (2.6%), and the angle of attack at which it occurred remained unchanged from $\delta_t = 0°$. Thus, the effects of trim tab deflection on the lifting characteristics of the NACA 3415 model were small. Further inspection of Fig. 3.6 and Fig. 3.7 reveals that the effects of trim tab deflection on the drag characteristics of the model were also minimal.

From Fig. 3.6 and Fig. 3.7, however, the deflection of the trim tab caused a shift in C_m and C_h of the NACA 3415 model. This was expected, as the purpose of trim tabs is to shift the zero hinge moment position of a flap or control surface. As a result, the zero pitching moment of the model was also shifted. Despite this shift in magnitude of C_h, the behavior of $C_{h,StDev}$ remained independent of trim tab deflection. Since $C_{h,StDev}$ is a measure of the unsteadiness of the hinge moment, this indicates that the hinge moment deflection did not significantly affect the amount of unsteadiness of the hinge moment. Therefore, it can be concluded that the large increase in magnitude of $C_{h,StDev}$ that occurs at the angle of attack of $C_{l,max}$ is due to the separated boundary layer over the flap. This can be seen in Fig. 3.6 and Fig. 3.7, where the large increases in $C_{h,StDev}$ are consistent for all trim tab deflections. Since trim tab deflection was not observed to significantly alter the unsteadiness of the hinge moment, and in an effort to reduce the size of the test matrix, the remainder of the experiment did not include the use of the trim tab.

3.4 Effect of Simulated Ice on NACA 3415

Glaze and rime ice were simulated on the NACA 3415 model using the methods discussed in Section 2.2.1. The performance of the NACA 3415 model with simulated ice contamination is shown in Fig. 3.8.

3.4.1 Simulated Glaze Ice

As expected, the simulated glaze-ice shape had a significant impact on the aerodynamic characteristics of the model, as seen in Fig. 3.8. At a Reynolds number of 1.8×10^6, the simulated glaze shape reduced $C_{l,max}$ by 0.65 (45.6%), and the angle of attack at which it occurs by 6.5° from the clean case. Perhaps the most notable characteristic change from the clean case, however, was in $C_{h,StDev}$. At the onset of separation for the simulated glaze case, the $C_{h,StDev}$ curve experienced a large, gradual increase up to a much higher magnitude than that of the clean case.

In order to better observe the effect of the simulated glaze ice on the flow separation, surface C_p distributions for the glaze-ice case are shown in Fig. 3.9. However, since the simulated glaze shape was placed at $x/c = 0.02$, a few surface pressure taps around this chordwise location were blocked. At an angle of attack of 4°, the laminar boundary layer separated from the simulated glaze ice. From Fig. 3.9, transition is visible at the end of the constant pressure region around $x/c \approx 0.08$ and boundary-layer reattachment occurs downstream of transition between $x/c \approx 0.10$ and $x/c \approx 0.14$. At $\alpha = 6°$, the chordwise extent of the laminar separation bubble increased. From Fig. 3.9, after the laminar boundary-layer separation at $x/c = 0.02$, the flow transitioned around $x/c = 0.10$ and reattached downstream of transition, between $x/c \approx 0.14$ and $x/c \approx 0.18$.

At $\alpha = 8°$, the chordwise extent of the laminar separation bubble is farther increased. From Fig. 3.9, after the laminar boundary-layer separation at $x/c = 0.02$, the flow transitioned around $x/c \approx 0.12$ and reattached downstream of transition, between $x/c \approx 0.14$ and $x/c \approx 0.32$. Additionally, at $\alpha = 8°$, another region of constant negative pressure, from around $x/c \approx 0.68$ to $x/c = 1.0$, is indicative of boundary-layer separation. In other words, at $\alpha = 8°$, the NACA 3415 model with simulated glaze-ice shape experiences boundary-layer separation that reattaches at chordwise locations that move farther downstream with increased angle of attack, indicating a thin-airfoil-type stall, while also having separation over the trailing edge of the model with the chordwise separation location moving upstream with increased angle of attack, indicating a trailing-edge-type stall. Thus, the NACA 3415 with the simulated glaze-ice contamination exhibits a mixed thin-airfoil-type and trailing-edge-type stall. At $\alpha = 10°$, the flow was unable to reattach after initially separating from the simulated glaze ice and remains separated into the wake.

3.4.2 Simulated Rime Ice

While the changes in aerodynamic characteristics from the clean case to the simulated rime-ice contamination case, as seen in Fig. 3.8, are less severe than the glaze-ice case, the reduction of $C_{l,max}$ and the increase in drag are still significant. At a Reynolds number of 1.8×10^6, the simulated rime shape reduced $C_{l,max}$ by 0.28 (19.7%), and the angle of attack at which it occurred by 1°. As observed in the glaze-ice case, the $C_{h,StDev}$ curve increased to a greater magnitude and at a lower angle of attack for the rime-ice case than the clean case. The angle of

attack corresponding to this increase was also the angle of attack of stall, thus indicating that the unsteady hinge moment is sensitive to the effects of boundary-layer separation.

The effect of the simulated rime shape on the surface C_p distribution can be seen in Fig. 3.10. The geometry of the simulated rime shape blocked many of the leading-edge pressure taps up until about $x/c = 0.02$, leading to a slight distortion of the C_p distribution plots corresponding to these leading-edge surface pressure taps. From Fig. 3.10 around an angle of attack of 9°, evidence of a small separation bubble caused by the simulated rime ice extends to around $x/c \approx 0.08$. The chordwise extent of the separation bubble caused by the simulated rime ice was much smaller than that caused by the simulated glaze ice. At $\alpha = 13°$, after the initial separation downstream of the simulated rime ice, the flow reattached between $x/c \approx 0.08$ and $x/c \approx 0.16$. However, the constant negative pressure region from $x/c \approx 0.64$ to $x/c = 1.0$ indicates a second region of trailing-edge boundary-layer separation. Unlike the simulated glaze-ice case, the extent of the laminar separation bubble at the leading edge of the NACA 3415 model does not significantly increase in chordwise extent to become the primary cause of stall. At $\alpha = 15°$, the small region of separation downstream of the rime shape cannot be distinguished, but trailing-edge separation has moved upstream to $x/c \approx 0.40$. Thus, the NACA 3415 model with the simulated rime-ice shape exhibits a trailing-edge-type stall.[29]

It is interesting to note the difference in C_m and C_h characteristics between Reynolds numbers of 1.8×10^6 and 1.0×10^6 of the simulated rime-ice case on the NACA 3415 that begins to occur at $\alpha = 10°$, as shown in Fig. 3.8. This difference is consistent with separated flow over the model trailing edge beginning at a lower angle of attack for $\mathrm{Re} = 1.0 \times 10^6$ than for $\mathrm{Re} = 1.8 \times 10^6$. This can be seen in Fig. 3.11, where the trailing-edge C_p distributions are shown for both Reynolds numbers at discrete angles of attack. From Fig. 3.11, at $\alpha = 9°$ and $\alpha = 10°$ the pressure recovery over the flap appears to be mostly consistent between $\mathrm{Re} = 1.8 \times 10^6$ and $\mathrm{Re} = 1.0 \times 10^6$. At $\alpha = 11°$, while it is difficult to discern, the decrease in pressure that is associated with separated flow in a pressure recovery region causes the C_p values downstream of $x/c = 0.85$ corresponding to $\mathrm{Re} = 1.0 \times 10^6$ to be slightly more negative than those for $\mathrm{Re} = 1.8 \times 10^6$. At angles of attack lower than $\alpha = 11°$, the C_p values downstream of $x/c = 0.85$ for $\mathrm{Re} = 1.0 \times 10^6$ were mostly less negative than those for $\mathrm{Re} = 1.8 \times 10^6$. Additionally, at $\alpha = 12°$, the location of boundary-layer separation has moved upstream, leading to a reduction in pressure over the trailing edge for $\mathrm{Re} = 1.0 \times 10^6$ that does not appear to occur for $\mathrm{Re} = 1.8 \times 10^6$ at this angle of

attack. This indicates that the full pressure recovery of an attached flow is not occurring on the model trailing-edge surface for Re = 1.0×10^6 at $\alpha = 12°$.

These effects of trailing-edge boundary-layer separation for Re = 1.0×10^6 are particularly difficult to identify, as the pressure recovery over the trailing edge is very small. Therefore, the region of constant pressure that occurs due to boundary-layer separation near the trailing edge of the NACA 3415 can be difficult to recognize, as the C_p values downstream of the location of separation are already close to the C_p values at the location of separation. However, the implications of the trailing-edge separation can be observed in the performance of the rime-ice case at Re = 1.0×10^6 in Fig. 3.8. At $\alpha = 10°$, the break in C_m, C_h, and $C_{h,StDev}$ of the Re = 1.0×10^6 data from that of Re = 1.8×10^6 reveals the effects of the boundary-layer separation identified in Fig. 3.11.

3.5 Effect of Distributed Leading-Edge Roughness on NACA 3415

Two severity levels of distributed leading-edge roughness were tested on the NACA 3415 model using the methods discussed in Section 2.2.2. The performance of the NACA 3415 model with roughness contamination is shown in Fig. 3.12.

3.5.1 80-Grit Roughness

The aerodynamic characteristics of the airfoil with 80-grit roughness behaved as expected. The roughness on the leading-edge creates a thicker, less energetic turbulent boundary layer, generally leading to a decrease in $C_{l,max}$ and the angle of attack at which it occurs. At a Reynolds number of 1.8×10^6, $C_{l,max}$ was reduced by 0.32 (22.3%) for the 80-grit case, and the angle of attack of $C_{l,max}$ was reduced by 2.5°. Additionally, the roughness significantly increases the drag from the clean case. As seen in the simulated ice accretion test cases, the $C_{h,StDev}$ of the 80-grit roughness case experienced a large increase near the angle of attack of $C_{l,max}$. Again, the increase in $C_{h,StDev}$ can be attributed to the sensitivity of the hinge moment to flow separation.

C_p distributions for the 80-grit roughness case are shown in Fig. 3.13. Unlike the simulated icing cases, the roughness does not appear to induce a substantial separation bubble immediately downstream of the contamination location, as the roughness does not produce a strong adverse pressure gradient from a large-scale protuberance, like the simulated ice shapes. However, the roughness led to instabilities within the boundary layer, causing early boundary-

layer transition. Thus, the location of transition was likely located near the leading edge. From Fig. 3.13, at $\alpha = 5°$ and $\alpha = 8°$, the flow on the NACA 3415 model with 80-grit leading-edge roughness appears to be fully attached. At $\alpha = 11°$, however, boundary-layer separation on the flap surface becomes visible, beginning around $x/c \approx 0.80$. At $\alpha = 14°$, the location of boundary-layer separation moved significantly farther upstream from $\alpha = 12°$, with the surface from $x/c \approx 0.24$ to $x/c = 1.0$ completely separated. This is indicative of a trailing-edge-type stall.

3.5.2 14-Grit Roughness

The performance of the NACA 3415 model with 14-grit roughness was very similar to that of the model with 80-grit roughness. Like the 80-grit roughness case, a decrease in $C_{l,max}$ and the angle of attack at which it occurred resulted, most likely due to the creation of a thicker, less energetic turbulent boundary layer from the leading-edge roughness. At a Reynolds number of 1.8×10^6, $C_{l,max}$ was reduced by 0.45 (31.4%) for the 14-grit case, and the angle of attack of $C_{l,max}$ was reduced by 3.5°. Again, the separation across the flap section of the model induced a sudden increase in $C_{h,StDev}$ as the airfoil approached stall.

The effect of the 14-grit roughness on the surface C_p distribution can be seen in Fig. 3.14. The 14-grit roughness surface C_p distributions appear to be very similar to those of the 80-grit roughness case. Like the 80-grit roughness case, the flowfield of the 14-grit case in Fig. 3.14 appears to be fully attached for $\alpha = 5°$ and $\alpha = 8°$. At $\alpha = 11°$ a region of constant negative pressure beginning at approximately $x/c \approx 0.64$ can be observed, indicating a region of boundary-layer separation. In comparison to the 80-grit case at the same angle of attack, the chordwise location of boundary-layer separation was farther upstream for the 14-grit case. Additionally, the suction peak at the leading edge of the NACA 3415 model for the 14-grit case was smaller in magnitude than that of the 80-grit case. These effects can be attributed to the greater roughness height associated with the 14-grit roughness case creating a thicker turbulent boundary layer downstream of the roughness. Similar to the 80-grit roughness case, at $\alpha = 14°$ the boundary layer of the 14-grit roughness case is separated from $x/c \approx 0.20$ to $x/c = 1.0$.

3.6 Effect of 3D Simulated Damage on NACA 3415

Two types of 3D damage were simulated on the NACA 3415 model using the methods discussed in Section 2.2.3. The performance of the NACA 3415 model with simulated damage is shown in Fig. 3.15.

3.6.1 Simulated Leading-Edge Damage

By comparing Fig. 3.15 to Fig. 3.7 and Fig. 3.12, the first distinct difference between the results of the simulated damage case and the 2D test cases is the impact on the lift curve. The simulated damage cases did not have as large of an adverse effect on the angle of attack of $C_{l,max}$. At a Reynolds number of 1.8×10^6, the reduction in $C_{l,max}$ was 0.18 (12.6%) for the simulated leading-edge damage case, and the angle of attack of $C_{l,max}$ was reduced by 1.5°. This can be attributed, in part, to the 3D nature of the simulated damage tests. While premature separation may have occurred in the spanwise region of the protuberances, other spanwise regions of the model would not have experienced the perturbation from the simulated damage, and since the lift calculated from the balance measurements were integrated across the entire model span, the net effect of the 3D contamination was less than that of the previous 2D cases.

From Fig. 3.15, an initial break in $C_{h,StDev}$ for the simulated leading-edge damage case from the clean case is visible at $\alpha = 8°$. Due to the sensitivity of the hinge moment to separated flow, this is suggestive of a region of boundary-layer separation downstream of the simulated leading-edge damage beginning at this angle of attack. For the simulated leading-edge damage case, the large increase in $C_{h,StDev}$ corresponds to the same angle of attack as $C_{l,max}$. As the angle of attack of the model increases, the spanwise influence of the wake increases, causing the flow over the model surface to be deflected away from the wake in the spanwise direction. Thus, it is likely that premature stall occurred due to the growing spanwise region of separated flow downstream of the simulated leading-edge damage, also leading to increased unsteadiness in the hinge moment. This will be seen more clearly from the flow visualization of the simulated leading-edge damage on the NACA 23012 airfoil in Section 3.10.1.

The 3D simulated damage cases are a good test of the sensitivity of a hinge-moment-based protection system for isolated contamination or damage across a given span of the control surface. The wake drag measurements were made at a spanwise station directly downstream of the simulated damage. Therefore, the drag experienced a much larger change from the clean

case due to the contamination than C_l, C_m, and C_h. However, it is likely that if drag measurements were taken across other sections of the span, they would be much smaller than the ones provided here.

3.6.2 Simulated Upper-Surface Damage

From Fig. 3.15, it appears the simulated upper-surface damage did not have as large of an impact on C_l from the clean case as the simulated leading-edge damage. This is likely attributed to the placement of the simulated upper-surface damage farther downstream on the pressure recovery region of the airfoil. Since a large portion of the lift is generated by the leading-edge of the NACA 3415, the upper-surface region where the simulated damage was placed was not as crucial to lift generation as the leading-edge. At a Reynolds number of 1.8×10^6, the simulated upper-surface damage reduced $C_{l,max}$ by 0.08 (5.3%) from the clean case, and increased the angle of attack corresponding to $C_{l,max}$ by 0.5°.

While the leading-edge damage case caused an abrupt stall before the $C_{l,max}$ of the clean case, the simulated upper-surface damage case caused a more gradual stall to occur. The simulated upper-surface damage C_l and C_m curves had a distinct break from the clean C_l and C_m curves at $\alpha = 8°$. At that same angle of attack, the $C_{h,StDev}$ curve corresponding to the simulated upper-surface damage case experienced a distinct increase in slope, rather than a sudden increase in magnitude, like the 2D test cases. The $C_{h,StDev}$ curve corresponding to the simulated upper-surface damage case increased to a significant magnitude at a lower angle of attack than the angle of attack of $C_{l,max}$. These breaks in the performance of the simulated upper-surface damage case from the performance of the clean case can be attributed to regions of separation downstream of the simulated upper-surface damage. As the angle of attack of the model increases, the chordwise and spanwise extent of the separated region downstream of the simulated upper-surface damage increased more gradually than that of the simulated leading-edge damage. This led to a more gradual change in performance and level of unsteadiness in the hinge moment. This will be seen more clearly from the flow visualization of the simulated upper-surface damage on the NACA 23012 airfoil in Section 3.10.2.

3.7 Clean NACA 23012 Results

As with the NACA 3415, the performance of the clean NACA 23012 model was first investigated to generate a set of baseline measurements. The clean NACA 23012 performance is shown in Fig. 3.16 and Fig. 3.17 as a function of flap deflection. From Fig. 3.16, it is clear that the $C_{h,StDev}$ response of the NACA 23012 airfoil to stall is much greater than that of the NACA 3415. This is likely attributed to the leading-edge stall behavior of the NACA 23012, where the NACA 3415 exhibits a trailing-edge stall.[29] Since the area of flow separation during the stall process is much greater for the NACA 23012, it is logical that the unsteady flow in the separated region would cause greater amounts of unsteadiness in the hinge moment. Like the NACA 3415 results, the large increase in $C_{h,StDev}$ occurs at the same angle of attack as $C_{l,max}$.

Trends in the flowfield over the NACA 23012 model were observed using the C_p distribution. Figure 3.18 shows the C_p distribution of the clean NACA 23012 model with a flap setting of 0° for a range of angles of attack. From Fig. 3.18, the pressures at $\alpha = 5°$, 10°, and 15° reveal an attached flowfield, although the $\alpha = 15°$ results show a noticeably lower, constant trailing-edge pressure, suggesting separation over the flap just prior to stall. At $\alpha = 17°$, just past $C_{l,max}$, it is clear from the reduction in magnitude of the suction peak and the large region of constant pressure downstream of $x/c \approx 0.10$, that the airfoil has experienced a leading-edge stall. Downstream of $x/c \approx 0.10$, the constant negative chordwise pressure indicates that the boundary layer is massively separated.

The fluorescent-oil flow visualization for the clean NACA 23012 model can be seen in Fig. 3.19 through Fig. 3.24. Common flowfield features are labeled in Fig. 3.21, which corresponds to $\alpha = 6°$. Since the movement of the oil on the surface of the model is driven by the shear stress at the surface, the flowfield features are recognizable due to the shear stresses they produce on the surface. For example, at the stagnation point near the leading edge of the model, the shear stresses are high, which causes the oil on the surface to be scrubbed away from the stagnation point in the direction of the flow. The boundary-layer flow continues in the streamwise direction over the airfoil surface, causing the oil to move in the streamwise direction. At a point of boundary-layer separation, the shear stress at the surface of the model is zero. This causes the oil to collect at the chordwise location of boundary-layer separation, as the flow is no longer forcing it in the streamwise direction. In some regions of separated flow, the oil remains

unmoved, as the shear stress on the surface is usually low. Thus, regions of separated flow are often noticeable by the speckled pattern of the initial application. If a boundary-layer reattaches, there is a region of high shear stress in the vicinity of the location of reattachment. This causes the oil on the surface to be scrubbed away in both the upstream and downstream directions, similar to the behavior of a stagnation point.

From Fig. 3.19, Fig. 3.20, and Fig. 3.21, a laminar separation bubble on the NACA 23012 model upper surface can be seen at low angles of attack. This separation bubble can be difficult to discern in the C_p distributions, as the pressure recovery downstream of the laminar separation bubble is small. There are areas of high concentration of fluorescent oil in Fig. 3.19 which were the result of poor oil application for this particular angle of attack. Despite this problem, the laminar separation bubble on the upper surface at $\alpha = 0°$ can still be seen in Fig. 3.19. The upper-surface laminar separation bubble is large at $\alpha = 0°$, with initial separation around $x/c \approx 0.18$ and turbulent boundary-layer reattachment around $x/c \approx 0.32$. The chordwise location of separation was identified from a higher-resolution picture than that shown in Fig. 3.19, where around $x/c \approx 0.18$ the oil collected into droplets and was pulled down by gravity, indicating a region of very low shear. Though it is more difficult to see, in Fig. 3.19 a region of low shear stress on the airfoil lower surface is visible at $\alpha = 0°$ from $x/c \approx 0.48$ to $x/c \approx 0.65$, as the oil within this region does not move a significant amount. Downstream of $x/c \approx 0.65$, the shear stress at the surface of the model is high, as larger displacement of the oil is visible in the streamwise direction. This suggests that the boundary layer transitioned within the low-shear region, leading to an increase in the velocity gradient in the surface-normal direction. This transition region on the lower surface of the NACA 23012 at $\alpha = 0°$ is consistent with results obtained using XFOIL, which places boundary-layer transition at $x/c = 0.587$.[30]

As the angle of attack of the NACA 23012 model increased, the size of the upper-surface separation bubble decreased and the chordwise location of initial boundary-layer separation moved upstream. For $\alpha = 3°$, from Fig. 3.20, initial boundary-layer separation on the upper surface occurred around $x/c \approx 0.14$, with turbulent reattachment around $x/c \approx 0.22$. Also at $\alpha = 3°$, the chordwise location of boundary-layer transition on the lower surface moved downstream from $\alpha = 0°$. From Fig. 3.20, a region of low shear stress on the lower surface of the model is visible by the speckled pattern between $x/c \approx 0.68$ and $x/c \approx 0.92$. This is followed by a region of high shear stress at the surface between $x/c \approx 0.92$ and $x/c = 1.0$. This suggests that the boundary

layer transitioned within this low-shear region. This is also consistent with XFOIL, which, at α = 3°, places transition on the lower surface at x/c = 0.947.[30] From Fig. 3.16 for δ_f = 0°, there is a minimum in $C_{h,StDev}$ at α = 4°. This local decrease in $C_{h,StDev}$ is correlated with the decreasing extent of turbulent flow over the airfoil lower surface. For α = 6°, from Fig. 3.21, initial separation occurred on the upper surface around $x/c \approx 0.12$, with turbulent reattachment around $x/c \approx 0.18$. Additionally, the region of low shear stress and transition on the lower surface is no longer visible, indicating that the lower-surface boundary layer is likely fully laminar.

In Fig. 3.22 and Fig. 3.23, at α = 9° and α = 12°, respectively, the location of the separation bubble and its chordwise length shortened with increased angle of attack from α = 6°. From Fig. 3.24, a region of separated turbulent boundary layer over the trailing edge of the NACA 23012 model from $x/c \approx 0.65$ to x/c = 1.0 can be observed. This separated flow over the flap caused an increase in the unsteadiness in the surface pressure over the flap, leading to an increase in $C_{h,StDev}$. Thus, a correlation is observed between large increases in $C_{h,StDev}$ and regions of separated flow over the upper surface.

3.8 Effect of Simulated Ice on NACA 23012

Glaze- and rime-ice accretions were simulated on the NACA 23012 using methods discussed in Section 2.2.1. The performance of the NACA 23012 model with simulated ice contamination is shown in Fig. 3.25.

3.8.1 Simulated Glaze Ice

As also observed for the NACA 3415 in Fig. 3.8, the simulated glaze-ice shape had the most significant impact on the aerodynamic characteristics of the NACA 23012 model, as shown in Fig. 3.25, of all of the contamination configurations tested. At a Reynolds number of 1.8×10^6, the simulated glaze ice reduced $C_{l,max}$ by 0.88 (59.8%), and the angle of attack at which it occurs by 8.5° from the clean case. While the magnitude of $C_{h,StDev}$ after stall of the glaze-ice case was not as large as the clean case at Re = 1.8×10^6 (as it was for the NACA 3415), the increase in $C_{h,StDev}$ occurred at a lower angle of attack and over a longer angle-of-attack range than the clean case. This is indicative of a more gradual, thin-airfoil-type stalling behavior when the simulated glaze ice was present, which is consistent with the C_l plot from Fig. 3.25.

In order to observe the flowfield effects related to the simulated glaze-ice case, the surface C_p distributions are shown in Fig. 3.26. Since the simulated glaze-ice shape was placed at $x/c = 0.02$ a few surface pressure taps around this chordwise location were blocked. For $\alpha = 2°$, laminar boundary-layer separation occurred on the simulated glaze ice. Boundary-layer transition is visible around $x/c \approx 0.08$ with reattachment occurring downstream between $x/c \approx 0.10$ and $x/c \approx 0.14$. For $\alpha = 4°$, the boundary-layer transition remained around $x/c \approx 0.08$, but the chordwise location of reattachment moved downstream between $x/c \approx 0.12$ and $x/c \approx 0.20$. Thus, with increasing angle of attack, the location of boundary-layer reattachment moved farther downstream, which is the typical behavior of a thin-airfoil-type stall. At $\alpha = 6°$, the separated region appears to extend over the main element and onto the flap. At $\alpha = 8°$, the boundary layer is massively separated and the airfoil suction peak is no longer present.

3.8.2 Simulated Rime Ice

Like the results from the NACA 3415 in Fig. 3.8, the reduction in aerodynamic performance of the NACA 23012 model rime-ice case, from Fig. 3.25, was less than that of the glaze-ice case. However, the simulated rime ice caused a significant effect on the aerodynamic characteristics of the NACA 23012. At a Reynolds number of 1.8×10^6, the simulated rime shape reduced $C_{l,max}$ by 0.44 (29.7%) and the angle of attack at which it occurs by 4.0°. Like the glaze-ice case, the rime-ice case had a more gradual increase in $C_{h,StDev}$ and a more gradual stall than the clean case. However, the increase in $C_{h,StDev}$ by the simulated rime ice occurred much closer to the angle of attack of stall than the glaze-ice case.

The surface C_p distributions for the rime-ice case are shown in Fig. 3.27. Since the simulated rime-ice shape was placed at the leading edge of the model up to around $x/c = 0.02$, there was a slight distortion in some of the pressure readings due to blockage in this leading-edge region. From Fig. 3.27, at $\alpha = 3°$, a small separation bubble is visible at the leading edge of the model, from $x/c \approx 0.02$ to $x/c \approx 0.04$. Similar flowfield effects were also observed for $\alpha = 7°$, where a small separation bubble formed from the simulated rime ice, and reattached downstream of the simulated rime ice, between $x/c \approx 0.03$ and $x/c \approx 0.05$, in a region of favorable pressure gradient. These separation bubbles at $\alpha = 3°$ and $\alpha = 7°$ caused by the simulated rime ice were much smaller in size than that created by the simulated glaze ice. At $\alpha = 11°$, the flow reattaches downstream of the simulated rime ice, but separation over the flap region is apparent, due to the

distribution of constant, negative pressure beginning around $x/c \approx 0.80$. This is indicative of a trailing-edge-type stall, as the primary cause of stall is the separated boundary layer over the trailing edge of the airfoil with an initial boundary-layer separation point that moves upstream with increasing angle of attack. At $\alpha = 13°$, the separation bubble downstream of the simulated rime shape becomes difficult to distinguish, and the boundary layer is massively separated downstream of $x/c \approx 0.34$.

3.9 Effect of Distributed Leading-Edge Roughness on NACA 23012

Two severity levels of distributed leading-edge roughness were simulated on the NACA 23012 model using the methods discussed in Section 2.2.2. The performance of the NACA 23012 model with roughness contamination is shown in Fig. 3.28.

3.9.1 80-Grit Roughness

As seen in Fig. 3.28, the 80-grit roughness case exhibited the same sudden leading-edge stall behavior as the clean case. This leading-edge-type stall behavior was more pronounced for $\mathrm{Re} = 1.8 \times 10^6$ than it was for 1.0×10^6. However, the leading-edge roughness produced premature stall at a reduced $C_{l,max}$ due to the roughness elements extracting energy from the boundary layer at the leading edge of the NACA 23012 model. At a Reynolds number of 1.8×10^6, the 80-grit roughness reduced $C_{l,max}$ by 0.40 (27.2%) and the angle of attack at which it occurs by 4.5°. As also observed in the NACA 3415 results in Fig. 3.12, the roughness significantly increased the drag from the clean case. Unlike the simulated ice accretion tests, the leading-edge roughness did not lead to a more gradual stalling characteristic, meaning that the sharp increase in $C_{h,StDev}$ occurred at the angle of attack of $C_{l,max}$.

Surface pressure distributions for the 80-grit roughness case are shown in Fig. 3.29. Unlike the simulated ice cases, the roughness cases did not produce a separation bubble associated with the contamination, as transition of the boundary layer likely occurred close to the leading edge due to the boundary-layer disturbances created by the distributed roughness. This can be seen in Fig. 3.29 for $\alpha = 2°$ and $\alpha = 6°$, where there is no laminar separation bubble. Comparing the pressure distributions of the 80-grit case at $\alpha = 10°$, in Fig. 3.29, to distributions at $\alpha = 10°$ for the clean case in Fig. 3.18, it is apparent that the roughness slightly decreased the magnitude of the suction peak of the airfoil prior to stall. As the angle of attack exceeds that of

$C_{l,max}$, the airfoil experiences a leading-edge-type stall as observed from the pressure distribution corresponding to $\alpha = 12°$ where the flow separates at the airfoil leading edge. From Fig. 3.29, at $\alpha = 12°$ the suction peak at the leading edge of the airfoil has decreased in magnitude and the boundary layer is massively separated downstream of $x/c \approx 0.12$, indicating a leading-edge-type stall, similar to that seen for the clean case in Fig. 3.18 at $\alpha = 17°$.

3.9.2 14-Grit Roughness

From Fig. 3.28, the effect of the 14-grit roughness on the NACA 23012 behaved in a similar fashion as the 80-grit roughness, with an increase in severity. This is also consistent with the results obtained from the NACA 3415 model, as shown in Fig. 3.12. Like the 80-grit roughness, the 14-grit roughness did not change the leading-edge-type stall behavior of the NACA 23012 and produced premature stall at a reduced $C_{l,max}$ due to the roughness elements extracting energy from the boundary layer at the leading edge of the NACA 23012 model. At a Reynolds number of 1.8×10^6, the 14-grit roughness reduced $C_{l,max}$ by 0.63 (42.4%) and the angle of attack at which it occurs by 6.5°. Like the 80-grit case, the $C_{h,StDev}$ for the 14-grit case experiences a sharp increase at the angle of attack of $C_{l,max}$. As found with the NACA 3415 results, a larger size of roughness leads to more significant changes to the aerodynamic characteristics of the airfoil model.

The effect of the 14-grit roughness on the airfoil surface pressure distributions are shown in Fig. 3.30. Like the 80-grit roughness case, boundary-layer transition would likely be located near the airfoil leading edge, before the formation of the laminar separation bubble. As a result, the laminar separation bubble identified from the clean flowfield data is not observed in Fig. 3.18. The pressure distributions for the 14-grit roughness case at $\alpha = 2°$ and $\alpha = 6°$, as seen in Fig. 3.30, are similar to those of the 80-grit roughness case at the same angles of attack. However, much like the results from the NACA 3415 tests, the stall angle of attack is lower for the 14-grit case than for the 80-grit case. This can be observed by comparing the pressure distribution of the 14-grit roughness case at $\alpha = 10°$, in Fig. 3.30, with that of the 80-grit roughness case at $\alpha = 10°$, in Fig. 3.29. While the 80-grit roughness case boundary layer remained attached over the leading edge of the model at $\alpha = 10°$, the 14-grit roughness case boundary-layer separated at the leading edge due the increase in the amount of momentum extracted from the boundary layer from the increased size of roughness elements. Like the 80-

grit roughness case, at $\alpha = 12°$ the decrease in the suction peak and massively separated boundary layer downstream of $x/c \approx 0.12$ of the 14-grit roughness case indicates a leading-edge-type stall. Thus, the addition of the roughness elements did not change the primary stall classification of the NACA 23012 model.

3.10 Effect of 3D Simulated Damage on NACA 23012

Two types of 3D damage were simulated on the NACA 23012 model using the methods discussed in Section 2.2.3. The performance of the NACA 23012 model with simulated damage is shown in Fig. 3.31.

3.10.1 Simulated Leading-Edge Damage

By comparing Fig. 3.25 and Fig. 3.28 to Fig. 3.31, the first major difference between the 2D contamination results and the 3D damage results is its effect on the performance of the NACA 23012. While the drag of the simulated leading-edge damage case was substantially higher than that of the clean case, the simulated leading-edge damage case did not have a large adverse effect on the angle of attack and magnitude of $C_{l,max}$. At a Reynolds number of 1.8×10^6, the reduction in $C_{l,max}$ was 0.16 (11.1%) for the simulated leading-edge damage case, and the angle of attack of $C_{l,max}$ was reduced by 2.0°. This can be attributed to the 3D effects of the contamination setup, since the contamination was placed in a localized area of the model surface and the aerodynamic characteristics were integrated across the entire surface. While the premature separation in the localized region of the simulated damage may have significantly altered the performance characteristics of that particular section, since the measured characteristics were integrated over the entire span, the isolated separation effects of these localized regions did not significantly reduce the total performance of the entire model.

Unlike some of the 2D contamination test results, $C_{h,StDev}$ steadily increases in magnitude before the angle of attack of airfoil stall for the simulated leading-edge damage case. This is attributed to the sensitivity of the hinge moment to unsteadiness in the localized separated wake generated by the simulated damage. While the region of premature separation may not span the entire model upper surface, the small region of separation immediately downstream of the simulated damage produces the same unsteadiness in the hinge moment due to regions of separation as previously observed.

In order to understand the effects of simulated leading-edge damage on the aerodynamic performance of the NACA 23012 model, the results of the fluorescent-oil flow visualization with the simulated leading-edge damage on the NACA 23012 model are shown in Fig. 3.32 through Fig. 3.37. From Fig. 3.32, the effects of the simulated leading-edge damage on the local flowfield can be observed. Five streaks of oil directly downstream of the hemispheres located at the trailing edge of the cluster can be seen in these fluorescent-oil flow visualization pictures. These streaks are created as a result of the counter-rotating vortices that are created by the hemispheres, which scrub the oil inward to form a line of low shear stress on the airfoil surface. This is consistent with the flow structures shown in the hemisphere cross-sectional schematic in Fig. 3.38. Additionally, the deflection of the flow, away from the wake of the hemispheres, can be seen downstream of the simulated leading-edge damage. These flow characteristics are consistent with the structure of the wake shown in Fig. 2.23. Additional flowfield features created by hemispheres can be seen in Fig. 3.39. Included in Fig. 3.39 is a region of inrushing flow. The flow in these regions, located immediately downstream of the hemispheres, is initially in the downstream direction towards the airfoil surface, and then curls inward and around the legs of the hairpin vortices. This process is explained in more detail in Alcar and Smith.[27] The inrush of flow can be seen in the fluorescent-oil flow visualization in Fig. 3.32 as the black region directly downstream of the simulated leading-edge damage, where the oil has been scrubbed away.

By comparing Fig. 3.32 to Fig. 3.19, it is apparent that the flowfield over the flap of the NACA 23012 model is similar for the clean model and the model with the simulated leading-edge damage. The boundary layer over the flap is turbulent and completely attached for both cases. The unsteadiness in the flowfield over the flap is comparable between the clean case and the simulated leading-edge damage case for $\alpha = 0°$, as shown in Fig. 3.31. Thus, at $\alpha = 0°$, the effect of the simulated leading-edge damage on $C_{h,StDev}$ is negligible. Similarly, by comparing Fig. 3.33 to Fig. 3.20 for $\alpha = 3°$, and by comparing Fig. 3.34 to Fig. 3.21 $\alpha = 6°$, it is clear that consistent values of $C_{h,StDev}$ were achieved between the clean case and the simulated leading-edge damage case due to the boundary layer over the flap being fully turbulent and attached. Thus, at low angles of attack, the simulated leading-edge damage had little effect on $C_{h,StDev}$.

From Fig. 3.31, the deviation of $C_{h,StDev}$ for the simulated leading-edge damage case from that of the clean case begins to be noticeable around $\alpha = 9°$. From Fig. 3.35, regions of

boundary-layer separation over the trailing edge of the flap can be observed that are not present in the flowfield of the clean case at $\alpha = 9°$, as seen in Fig. 3.22. These locations can be difficult to discern, so they are labeled in Fig. 3.35. These local regions of separated flow over the flap increase the unsteadiness in the flowfield, causing an increase in $C_{h,StDev}$ for the simulated leading-edge damage case, as compared to the clean case. Additionally, it can be seen in Fig. 3.35 that the spanwise deflection of the flow on the surface away from the wake, as well as the spanwise influence of the wake, of the simulated leading-edge damage increases with angle of attack.

The difference in $C_{h,StDev}$ between the simulated leading-edge damage case and the clean case becomes even larger for $\alpha = 12°$. From Fig. 3.36, a large region of separated flow is noticeable downstream of the simulated leading-edge damage. This region of separated flow is initially confined to a small spanwise region directly downstream of the simulated leading-edge damage. The spanwise influence of the separated region, however, increases further downstream. This region of separated flow is much larger than that observed in Fig. 3.23 for the clean case at $\alpha = 12°$, leading to an increased amount of unsteadiness in the flowfield over the flap, and in turn, elevated levels of $C_{h,StDev}$ from the clean case.

From Fig. 3.31, there was a large increase in the value of $C_{h,StDev}$ at $\alpha = 15°$ for the simulated leading-edge damage case from that observed at $\alpha = 12°$. Moreover, the value of $C_{h,StDev}$ of the simulated leading-edge damage case at $\alpha = 15°$ is much higher than that of the clean case at the same angle of attack, as seen in Fig. 3.31. By comparing Fig. 3.37 to Fig. 3.24, at $\alpha = 15°$ the separated region for the simulated leading-edge damage case begins immediately downstream of the simulated damage, where for the clean case at $\alpha = 15°$, the separated region begins around $x/c \approx 0.65$. Thus, the chordwise extent of the separated flow downstream of the simulated leading-edge damage at $\alpha = 15°$ is much greater than that of the clean case at the same angle of attack. The increased extent of separation for the simulated leading-edge damage case from the clean case leads to a greater amount of unsteadiness in the flow over the flap, leading to larger levels in $C_{h,StDev}$ for the simulated leading-edge damage case. From Fig. 3.37 and Fig. 3.36, the spanwise deflection of the flow at the model surface in the vicinity of the simulated leading-edge damage and its separated wake downstream is greater for $\alpha = 15°$ than for $\alpha = 12°$. Also, for the simulated leading-edge damage case at $\alpha = 15°$, there exists a region of reverse flow at the NACA 23012 model surface in the wake of the simulated leading-edge damage that was

not noticeable at $\alpha = 12°$. These factors led to the large increase in $C_{h,StDev}$ for the simulated leading-edge damage case from $\alpha = 12°$ to $\alpha = 15°$.

3.10.2 Simulated Upper-Surface Damage

Like the simulated leading-edge damage case, the simulated upper-surface damage did not have a significant impact on the lifting performance of the NACA 23012 model, as shown in Fig. 3.31. The lifting characteristics of the NACA 23012 model were also slightly less affected for the simulated upper-surface damage case than they were for the simulated leading-edge damage case. The increase in drag was lower for the simulated upper-surface damage case than that of the simulated leading-edge damage case. At a Reynolds number of 1.8×10^6, the reduction in $C_{l,max}$ was 0.09 (5.9%) for the simulated upper-surface damage case, and the angle of attack of $C_{l,max}$ was reduced by 0.5°.

Like the simulated leading-edge case, the simulated upper-surface damage had a smaller effect on the aerodynamic characteristics of the NACA 23012 model than the 2D contaminants due to the 3D effects of the contamination setup. Since the simulated upper-surface damage was placed further downstream than the simulated leading-edge damage, this is likely the reason why the simulated upper-surface damage had less of an impact on the performance of the NACA 23012 than the simulated leading-edge damage case, as the region of separated flow was much further downstream in the recovery region of the airfoil and the separated region was smaller. The effects of the simulated upper-surface damage on the NACA 23012 were consistent with those observed for the NACA 3415 simulated upper-surface damage case, where the performance of the airfoil with the simulated upper-surface damage experienced a distinct break from the clean case at an angle of attack corresponding to that where separation was present downstream of the simulated upper-surface damage.

Also, like the simulated leading-edge damage case, the simulated upper-surface damage case exhibited a steady increase in $C_{h,StDev}$ before the angle of attack of $C_{l,max}$. Again, this can be attributed to the sensitivity of the hinge moment to unsteadiness associated with regions of separated flow. Like the simulated leading-edge damage case, the simulated upper-surface damage case had a region of localized separated flow on the upper surface of the NACA 23012 model. Thus, the unsteadiness within this separated region caused an increase in $C_{h,StDev}$ before separation occurred over the NACA 23012 spanwise sections far from the simulated damage.

In order to better understand the effects of the simulated upper-surface damage on the aerodynamic performance of the NACA 23012 model, the results of the fluorescent-oil flow visualization with the simulated upper-surface damage on the NACA 23012 model are shown in Fig. 3.40 through Fig. 3.45. From Fig. 3.40, the effects of the simulated upper-surface damage on the local flowfield can be observed. Unlike the simulated leading-edge damage case, the influence of the hemispheres on the boundary layer upstream of the simulated damage can be seen in the simulated upper-surface damage case. Observation of the flowfield upstream of the six leading-edge hemispheres in the contamination cluster indicates the existence of two vortices in the horseshoe vortex system of the simulated damage. This observation is consistent with the distributed roughness elements from Winkler and Bragg,[31] as shown in Fig. 3.46. Like the simulated leading-edge damage flowfields, the simulated upper-surface damage flow visualization in Fig. 3.40 revealed oil streaks that were created due to counter-rotating flow downstream of the hemispheres, which were consistent with the structures in the hemisphere cross-section schematic in Fig. 3.38. Also from Fig. 3.40, an inrush of flow can be seen in fluorescent-oil flow visualization in the black region directly downstream of the simulated leading-edge damage, where the oil has been scrubbed away. This is consistent with the inrush of outer flow, as seen in the schematic in Fig. 3.39. These flow characteristics are also consistent with the structure of the wake shown in Fig. 2.23.

Like the clean and simulated leading-edge damage cases, the boundary layer over the flap at $\alpha = 0°$, 3°, and 6° was attached and turbulent, as shown in Fig. 3.40, Fig. 3.41, and Fig. 3.42. This led to comparable values of $C_{h,StDev}$ between the clean case, simulated leading-edge damage case, and simulated upper-surface damage case at these angles of attack. Also, like the simulated leading-edge damage case, the flow visualization of the simulated upper-surface damage case at $\alpha = 9°$, as shown in Fig. 3.43, reveals a region of separated flow downstream of the simulated damage that is not present for the clean case at $\alpha = 9°$, as shown in Fig. 3.22. Moreover, from Fig. 3.31, it can be observed that $C_{h,StDev}$ corresponding to the simulated upper-surface damage case begins to deviate from the clean case around $\alpha = 9°$. This unsteadiness in the hinge moment can be attributed to the unsteadiness in the separated region downstream of the simulated upper-surface damage.

From Fig. 3.43 and Fig. 3.44, the region of separated flow for the simulated upper-surface damage case increased in size from $\alpha = 9°$ to $\alpha = 12°$. Due to this increased region of

separated flow, the unsteadiness in the hinge moment, measured through $C_{h,StDev}$, increased from $\alpha = 9°$ to $\alpha = 12°$ as seen in Fig. 3.31. Like the simulated leading-edge damage case, the effects of the spanwise flow at the airfoil surface away from the wake of the simulated damage begins to become noticeable in Fig. 3.44 for the simulated upper-surface damage case at $\alpha = 12°$. At $\alpha = 15°$, the region of separation downstream of the simulated upper-surface damage, from Fig. 3.45, increased in size from $\alpha = 12°$. The spanwise deflection of the flow at the surface away from the wake of the simulated damage also increased from $\alpha = 12°$ to $\alpha = 15°$. Additionally, regions of reversed flow can be observed in the region of the wake downstream of the spanwise center of the simulated upper-surface damage. As a result of the increased extent of separation over the NACA 23012 model, the value of $C_{h,StDev}$ corresponding to the simulated upper-surface damage case increased from $\alpha = 12°$ to $\alpha = 15°$, as shown in Fig. 3.31. However, the magnitude of $C_{h,StDev}$ corresponding to $\alpha = 15°$ for the simulated upper-surface damage case is less than that of the simulated leading-edge damage case at the same angle of attack. This can be attributed to the larger chordwise extent of the separated region of the simulated leading-edge damage, as shown in Fig. 3.37, as compared to that of the simulated upper-surface damage, as shown in Fig. 3.45.

3.11 Figures

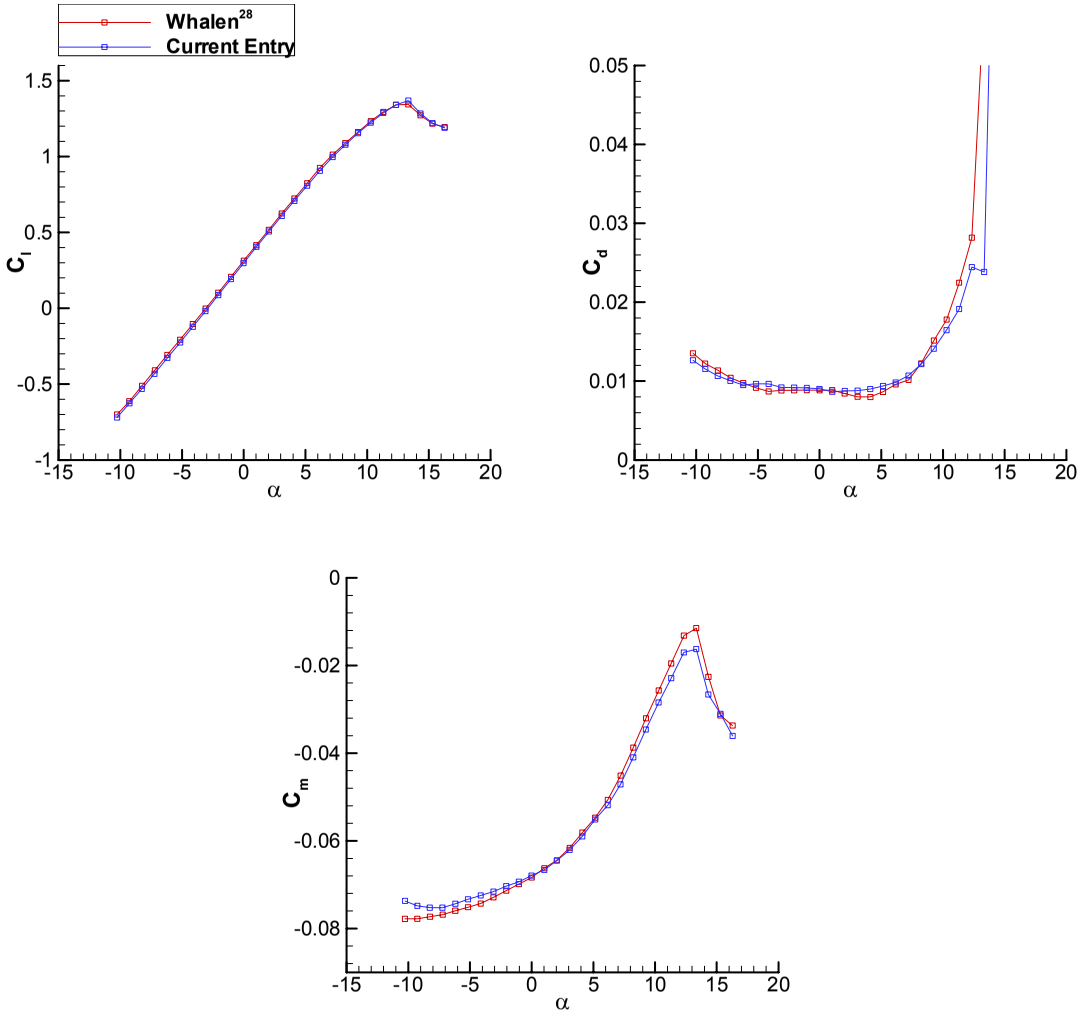

Fig. 3.1 NACA 3415 validation test result.

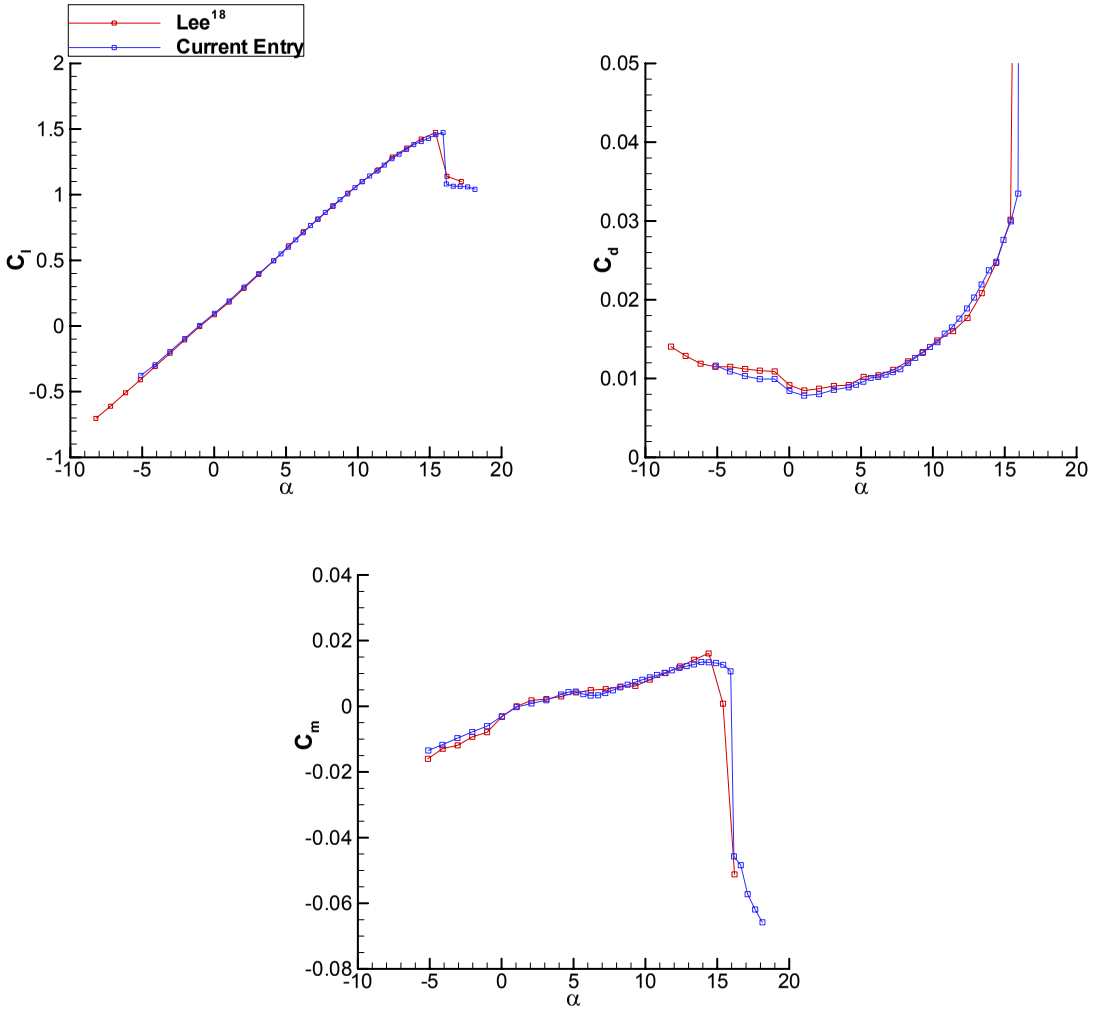

Fig. 3.2 NACA 23012 validation test result.

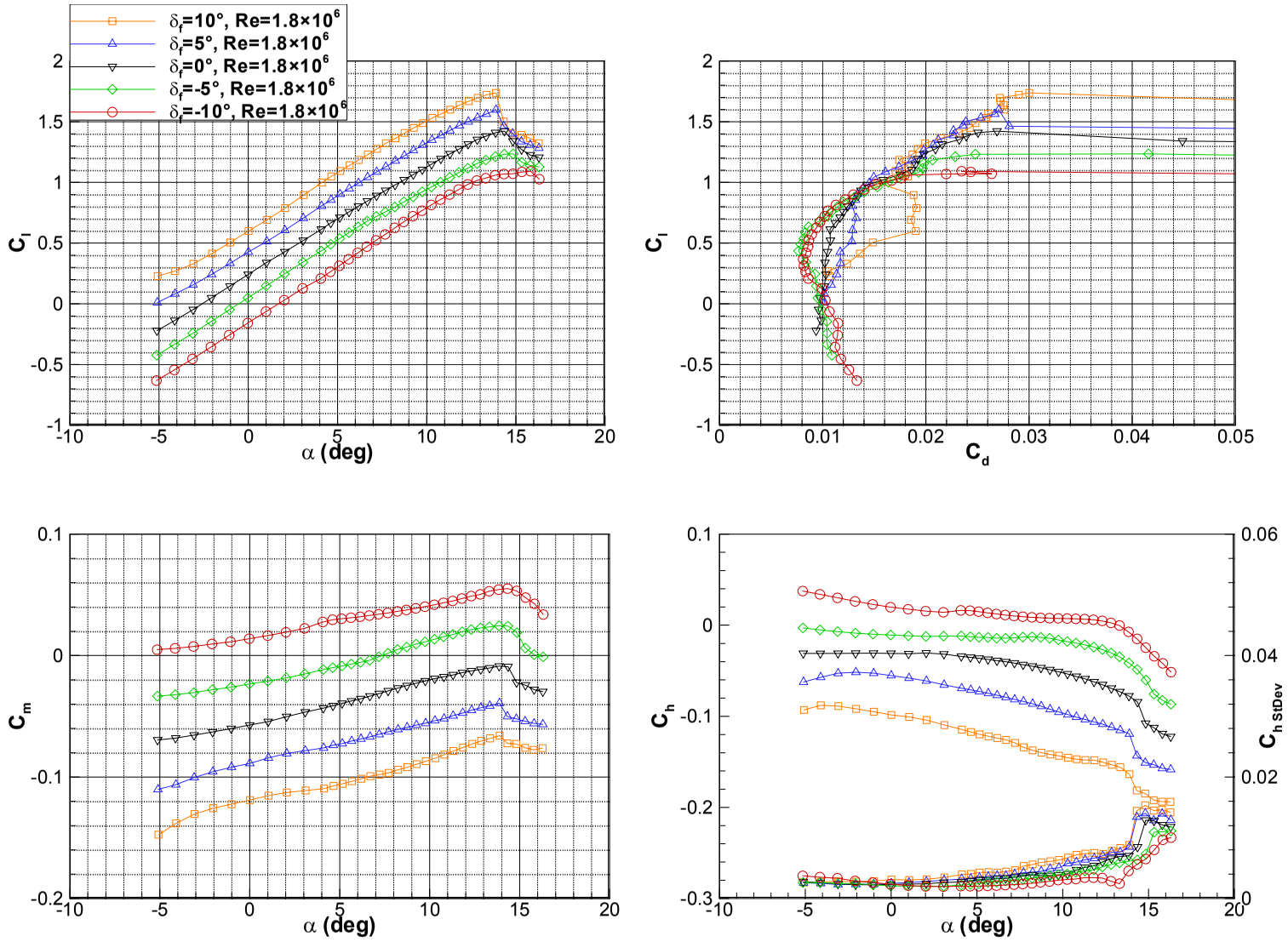

Fig. 3.3 Clean NACA 3415 performance with flap deflections at Re = 1.8 × 10^6.

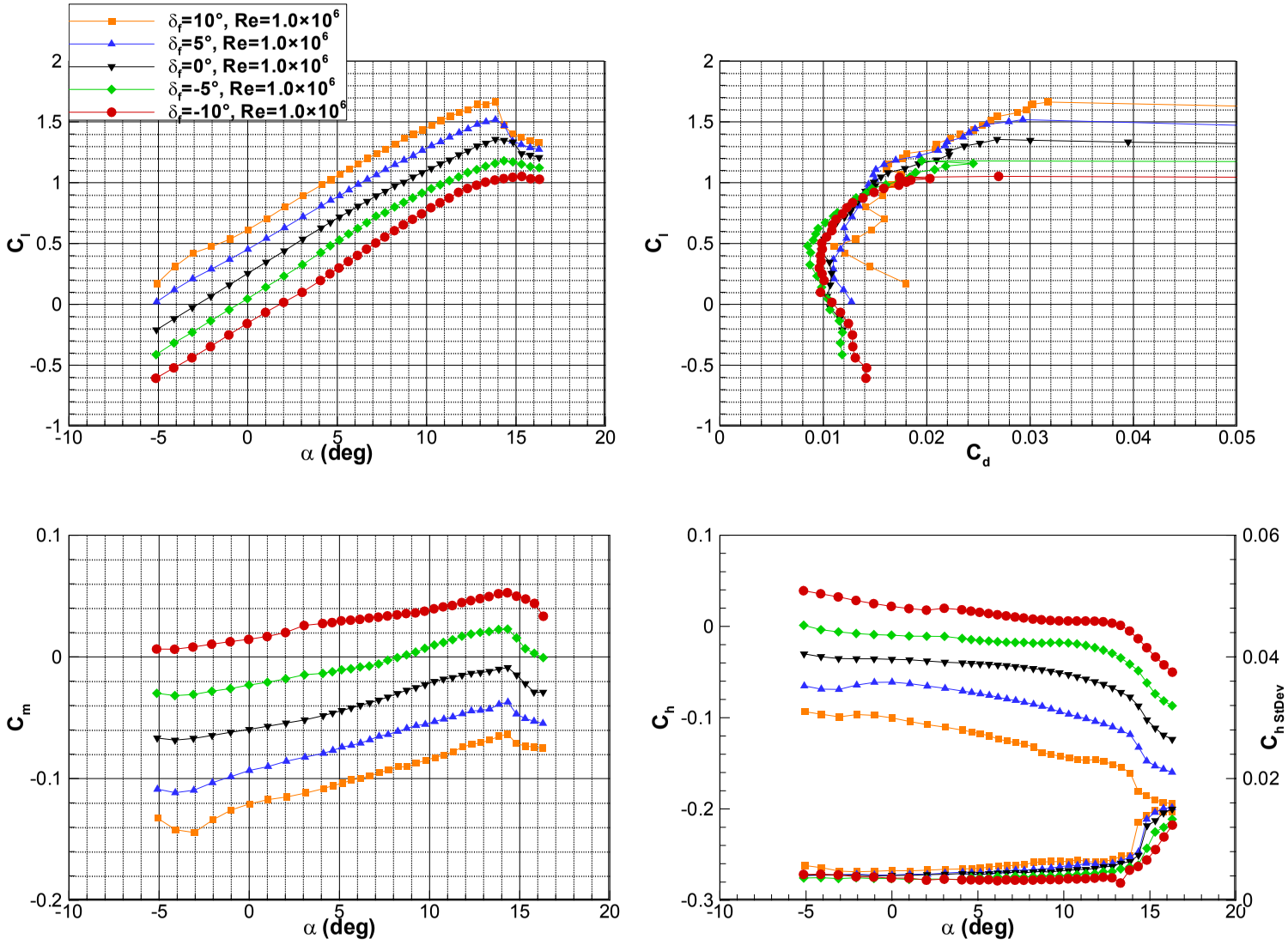

Fig. 3.4 Clean NACA 3415 performance with flap deflections at Re = 1.0 × 10^6.

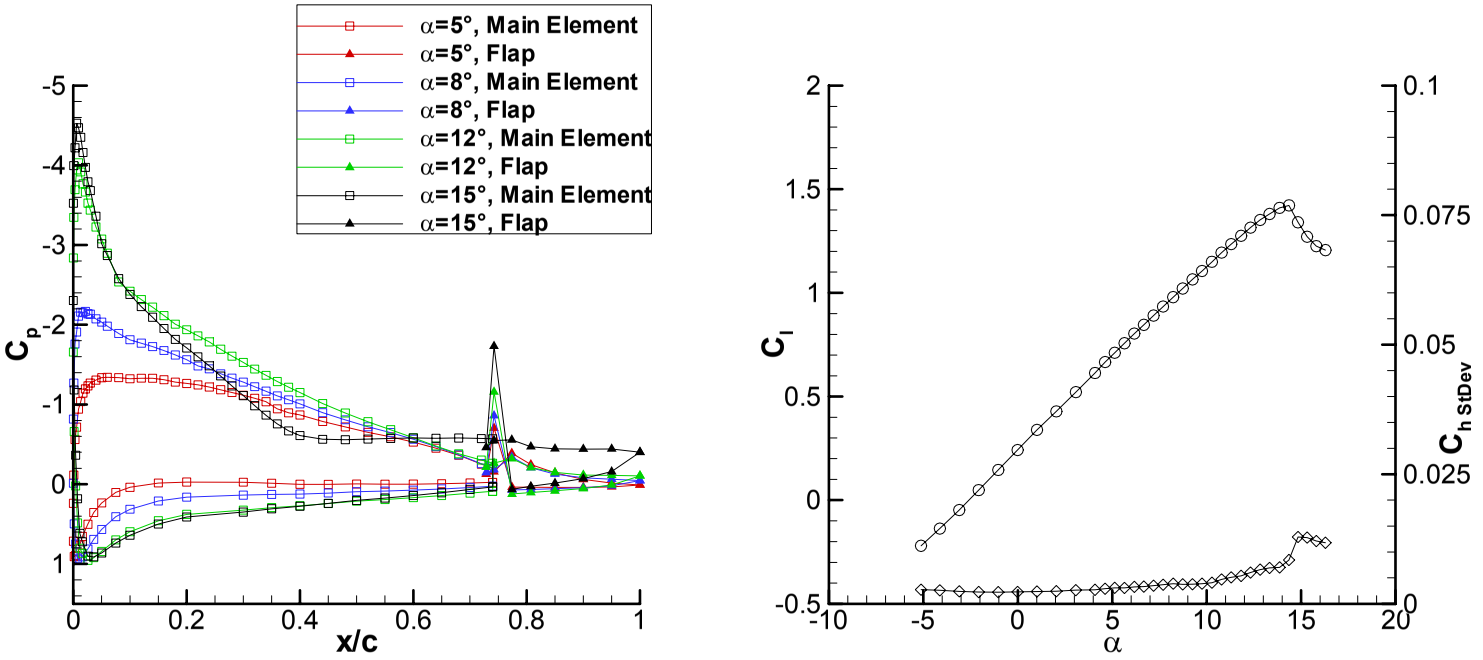

Fig. 3.5 Clean NACA 3415 surface C_p distributions with C_l and $C_{h,StDev}$ comparison for Re = 1.8 × 10^6 and $\delta_f = 0°$.

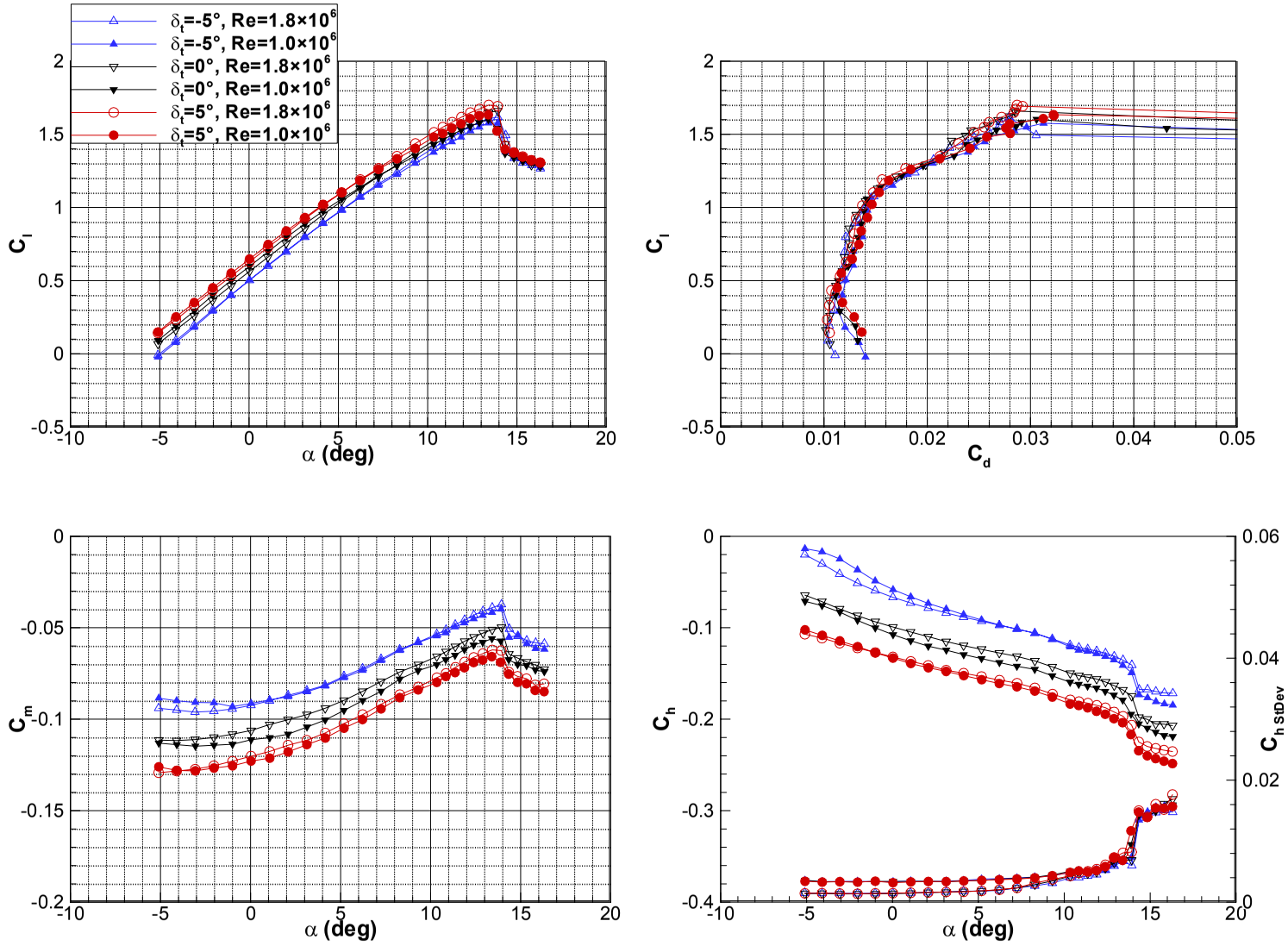

Fig. 3.6 Clean NACA 3415 performance with trim tab deflections at $\delta_f = 5°$.

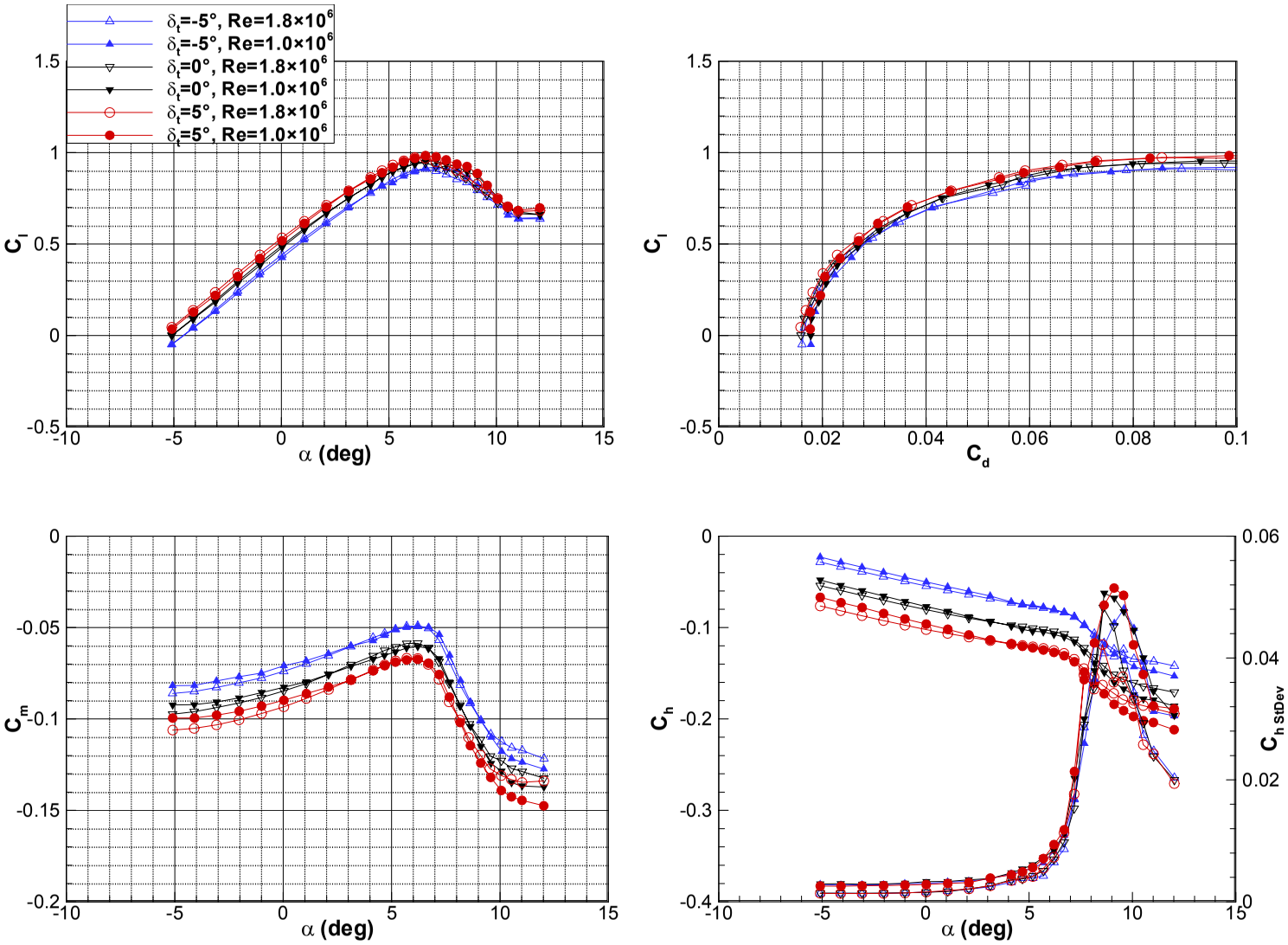

Fig. 3.7 NACA 3415 with simulated glaze ice performance with trim tab deflections at $\delta_f = 5°$.

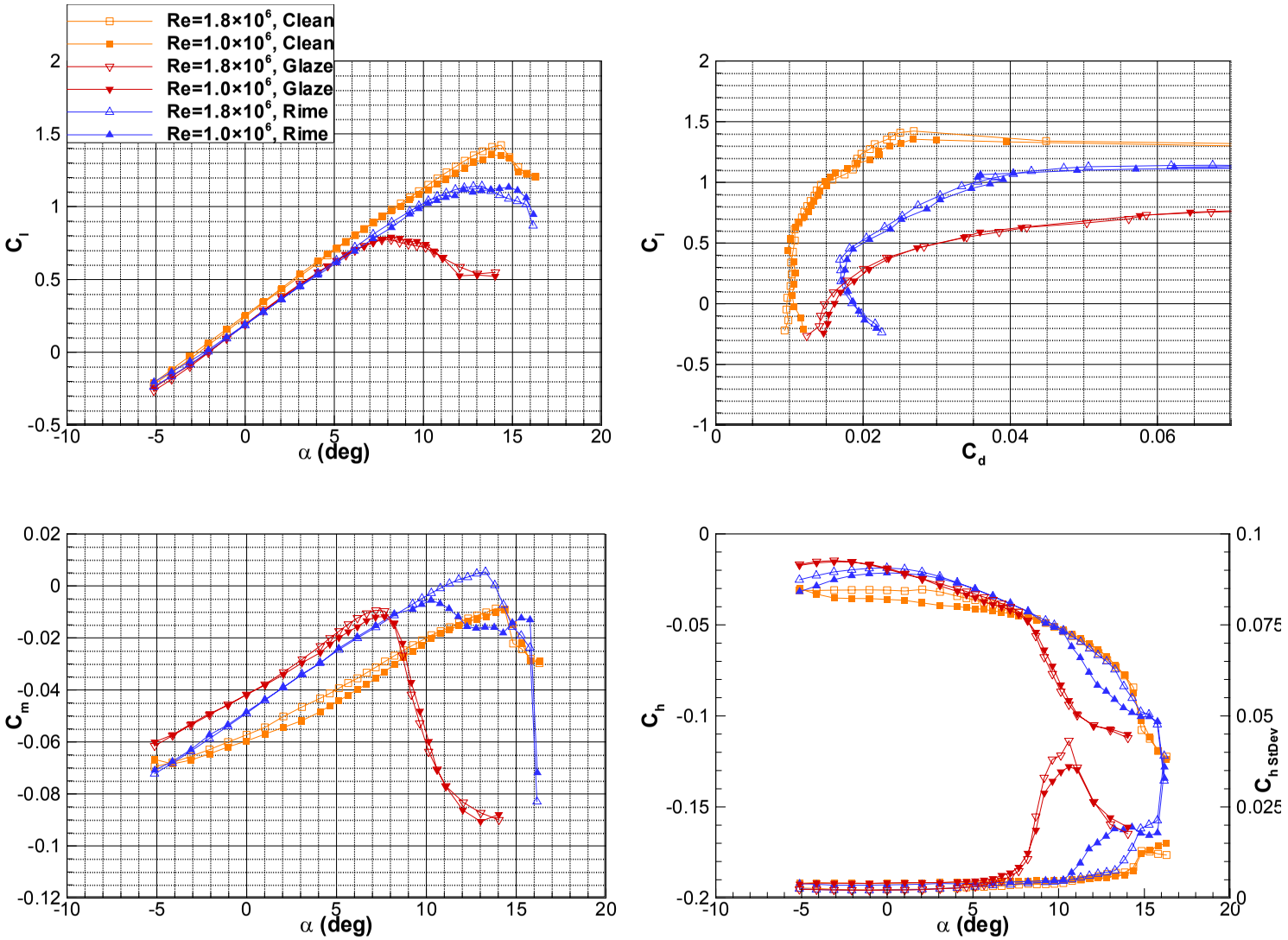

Fig. 3.8 NACA 3415 performance with simulated ice contamination, at flap setting of 0°.

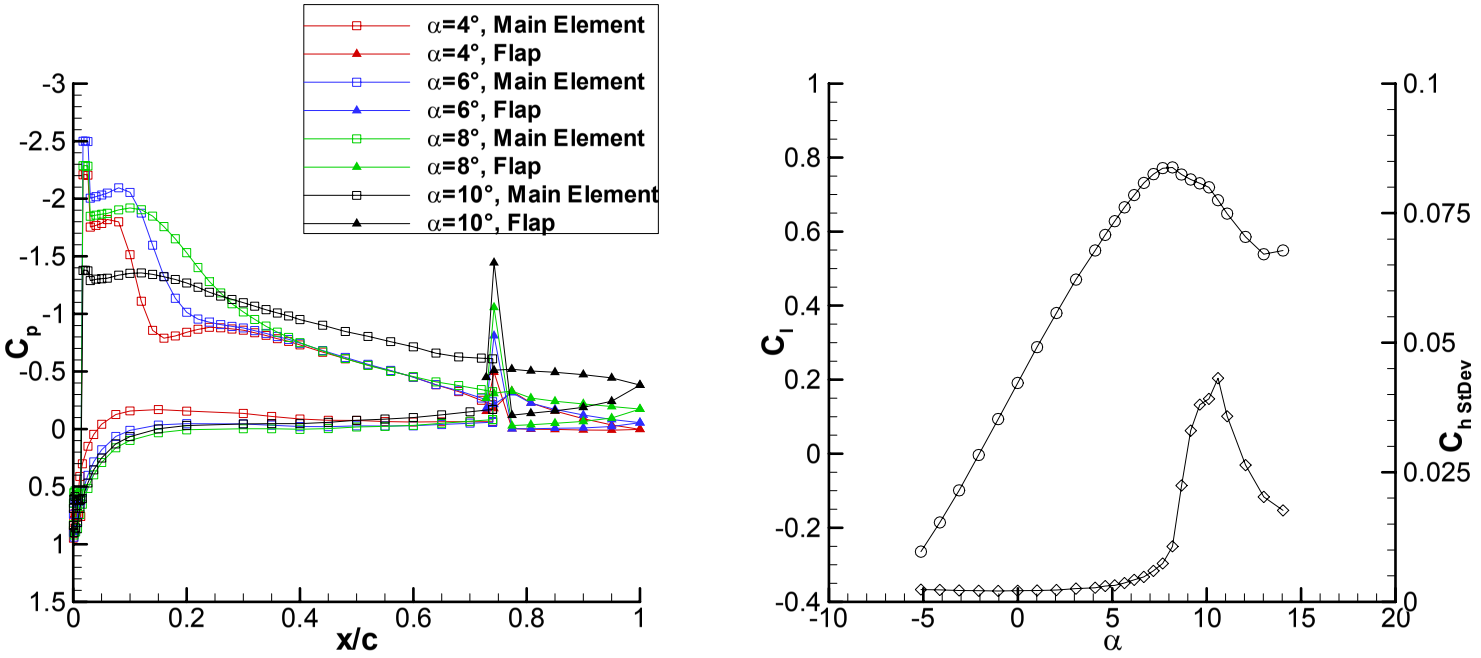

Fig. 3.9 NACA 3415 with simulated glaze ice surface C_p distributions with C_l and $C_{h,StDev}$ comparison for Re = 1.8 × 10^6 and δ_f = 0°.

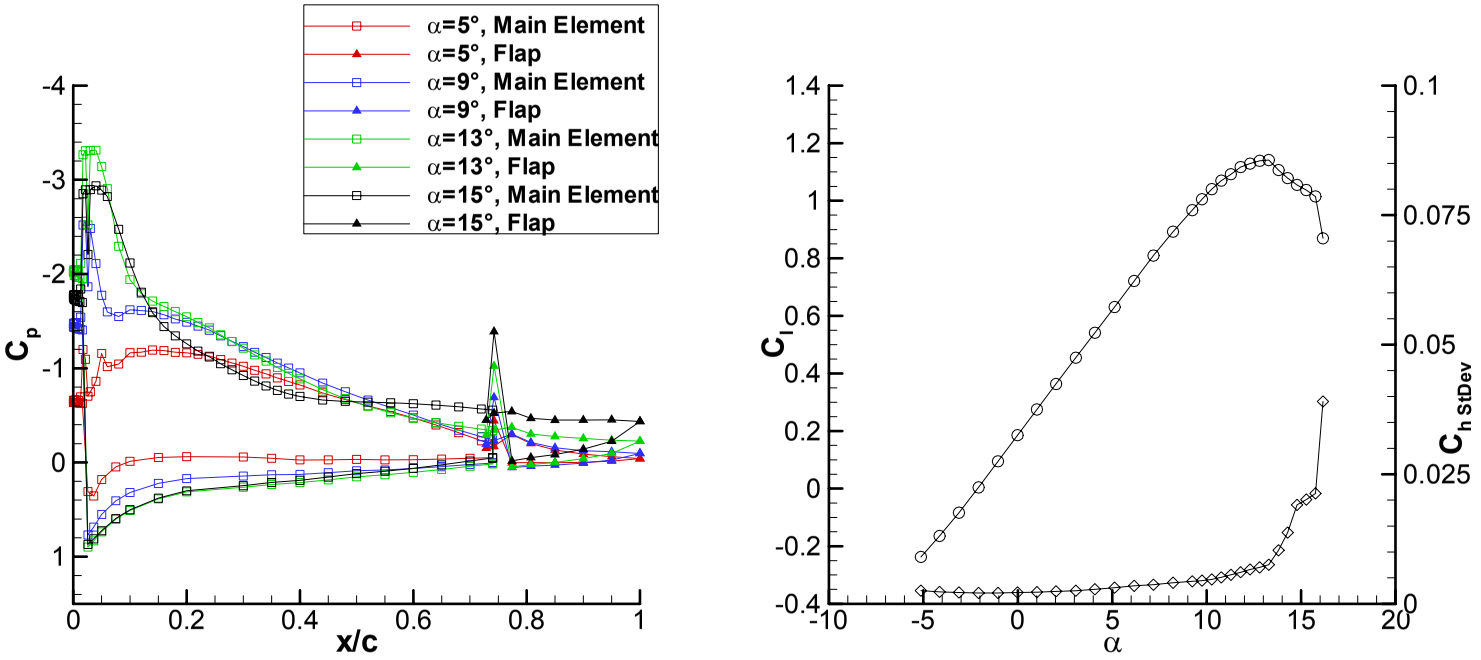

Fig. 3.10 NACA 3415 with simulated rime ice surface C_p distributions with C_l and $C_{h,StDev}$ comparison for Re = 1.8 × 10^6 and δ_f = 0°.

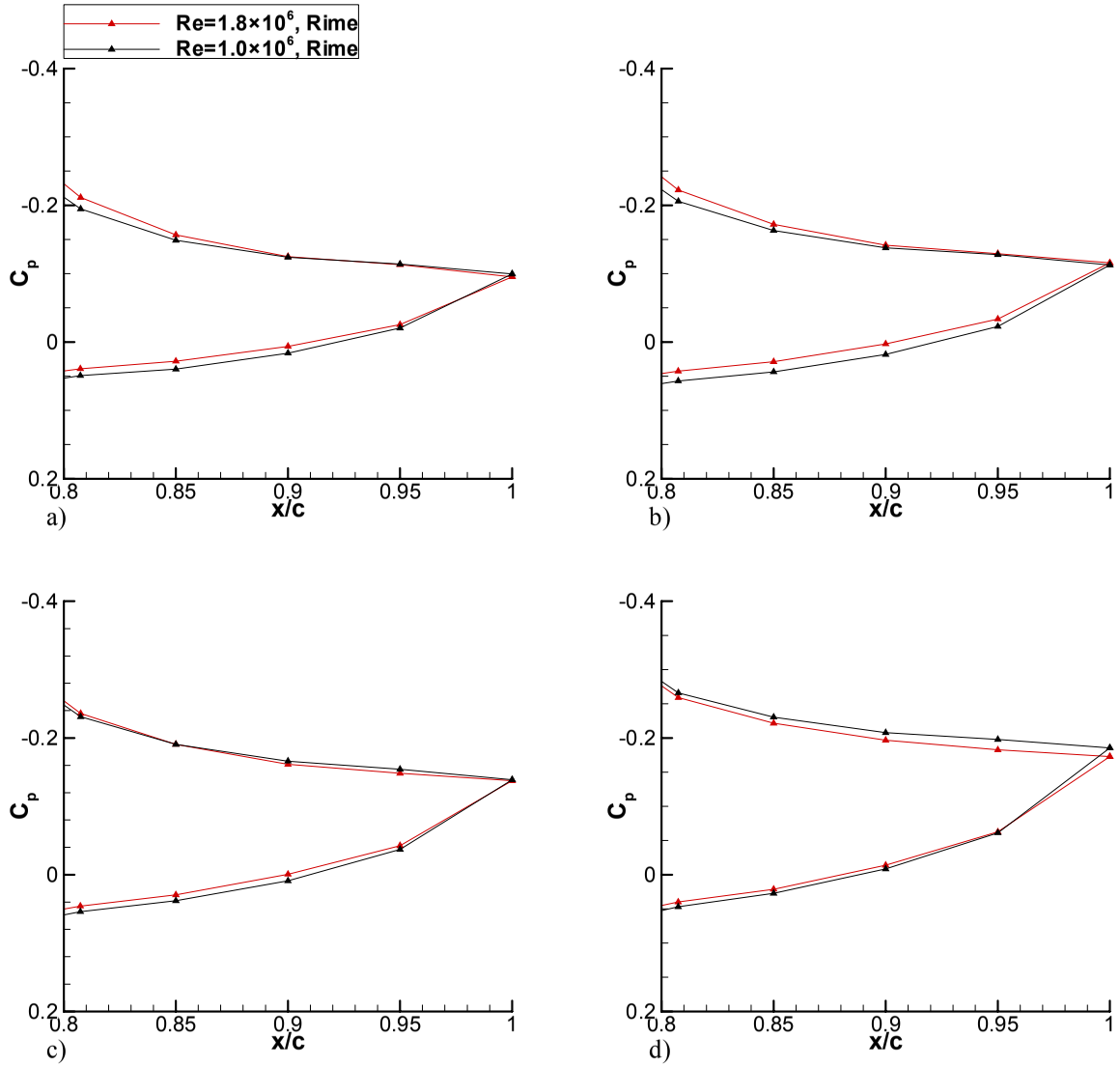

Fig. 3.11 Comparison of trailing-edge C_p distributions for Re = 1.8 × 10^6 and Re = 1.0 × 10^6 at, a) α = 9°; b) α = 10°; c) α = 11°; d) α = 12°.

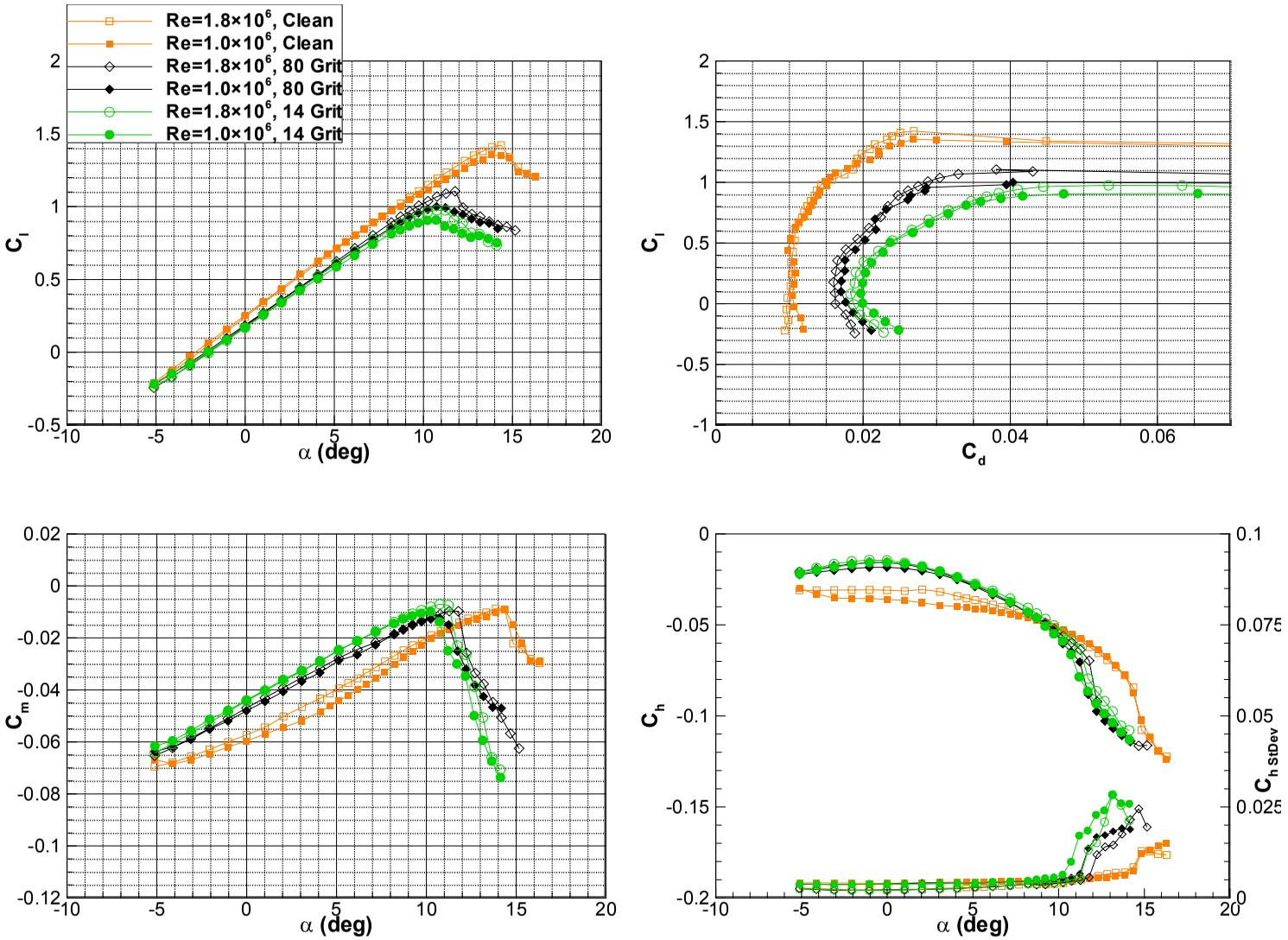

Fig. 3.12 NACA 3415 performance with leading-edge roughness, at flap setting of 0°.

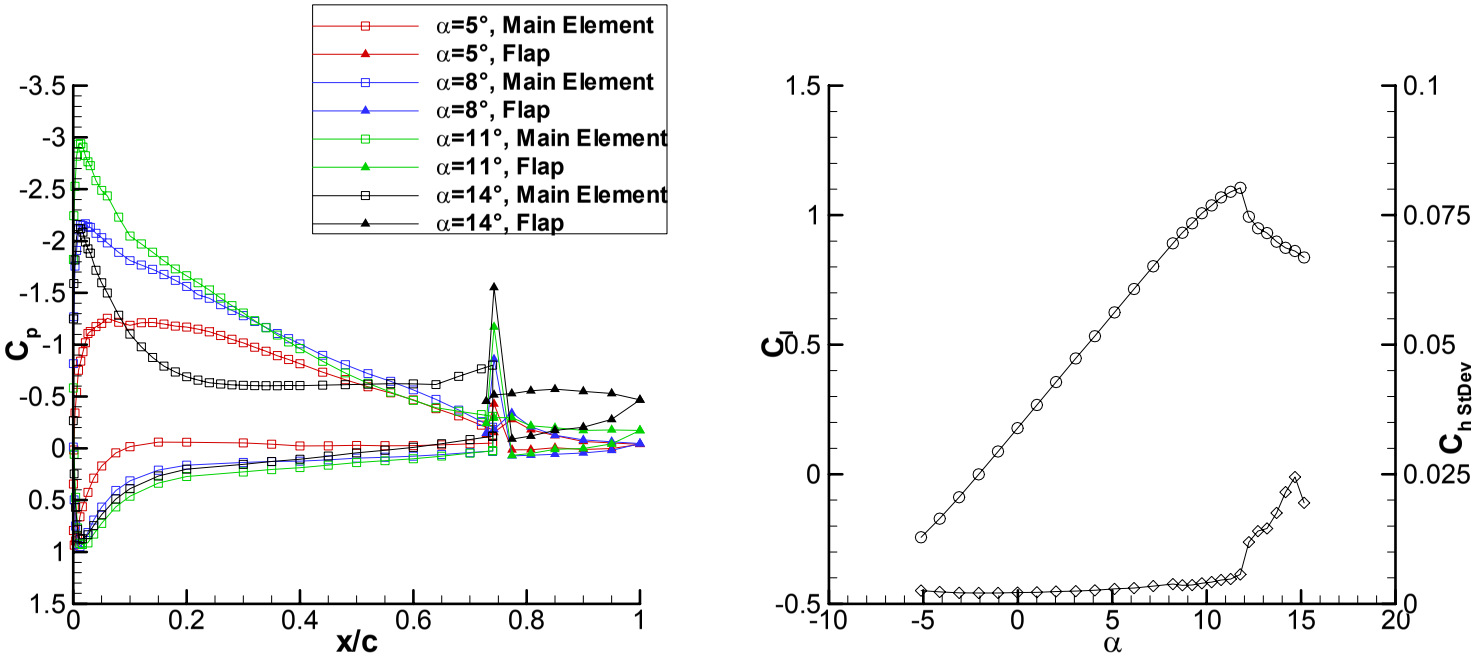

Fig. 3.13 NACA 3415 with 80-grit roughness surface C_p distributions with C_l and $C_{h,StDev}$ comparison for Re = 1.8 × 10^6 and δ_f = 0°.

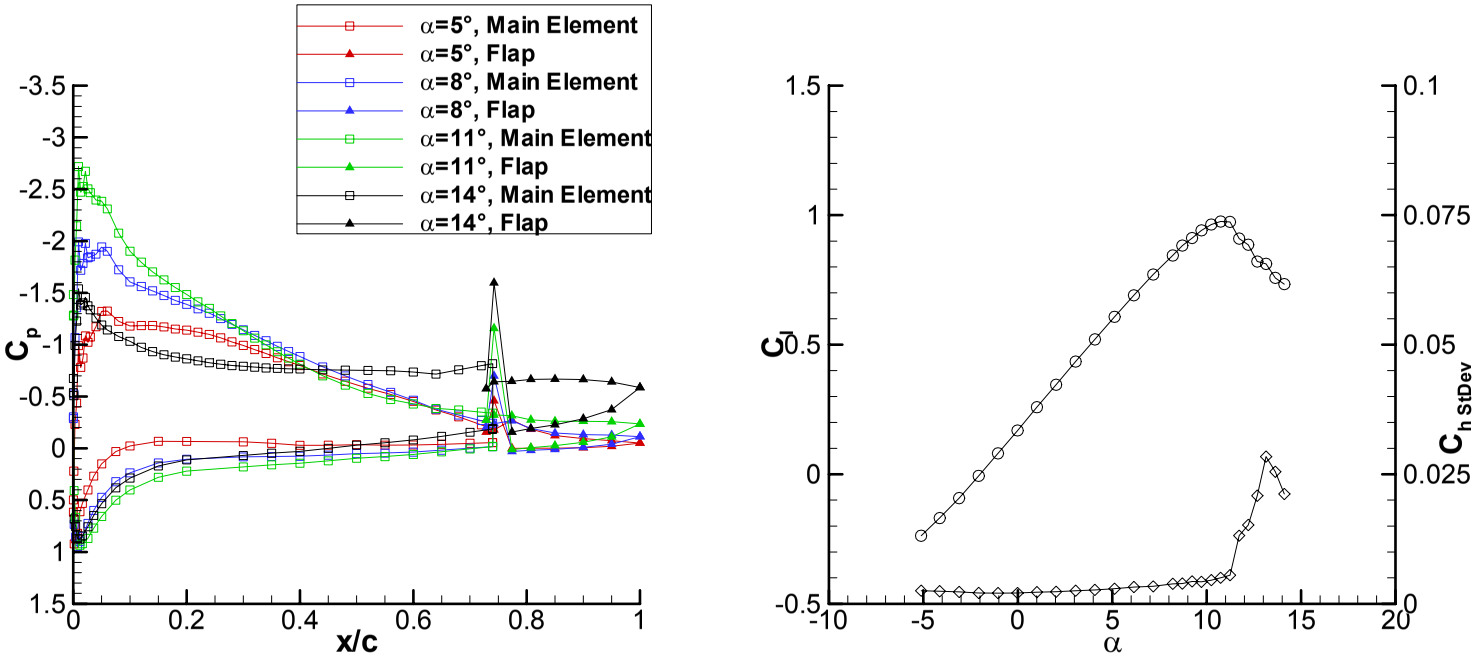

Fig. 3.14 NACA 3415 with 14-grit roughness surface C_p distributions with C_l and $C_{h,StDev}$ comparison for Re = 1.8×10^6 and δ_f = 0°.

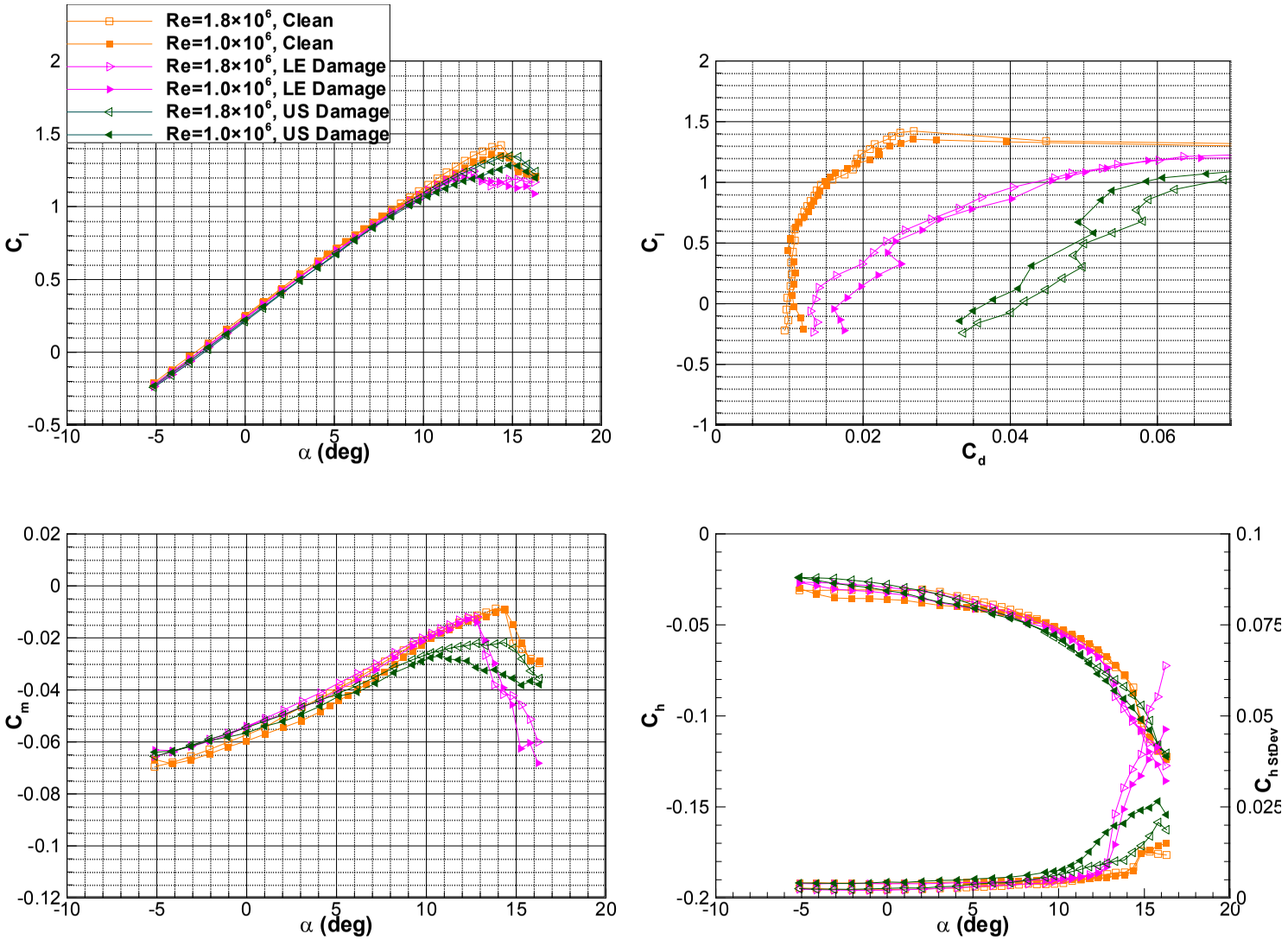

Fig. 3.15 NACA 3415 performance with simulated damage, at flap setting of 0°.

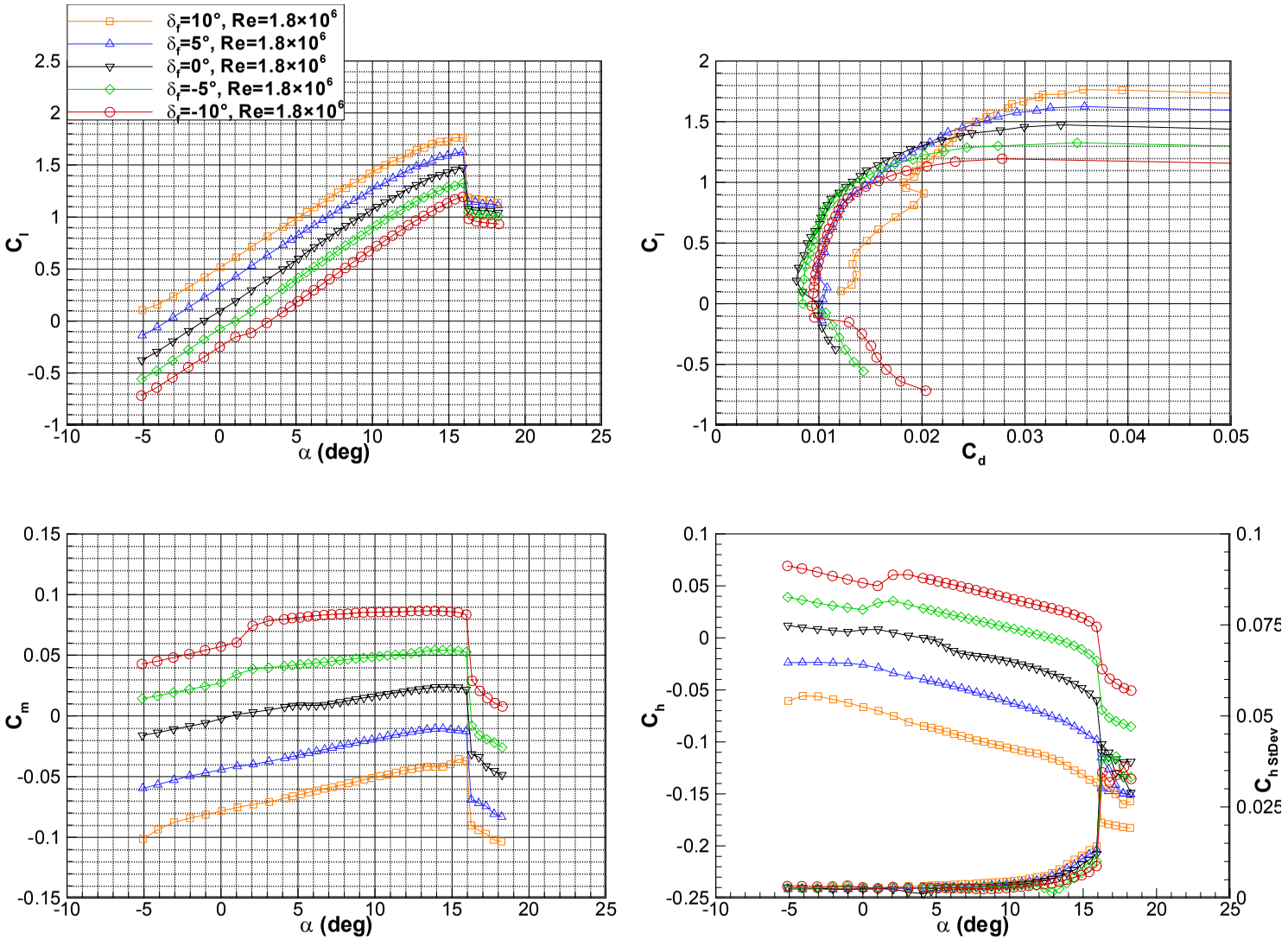

Fig. 3.16 Clean NACA 23012 performance with flap deflections at Re = 1.8 × 10^6.

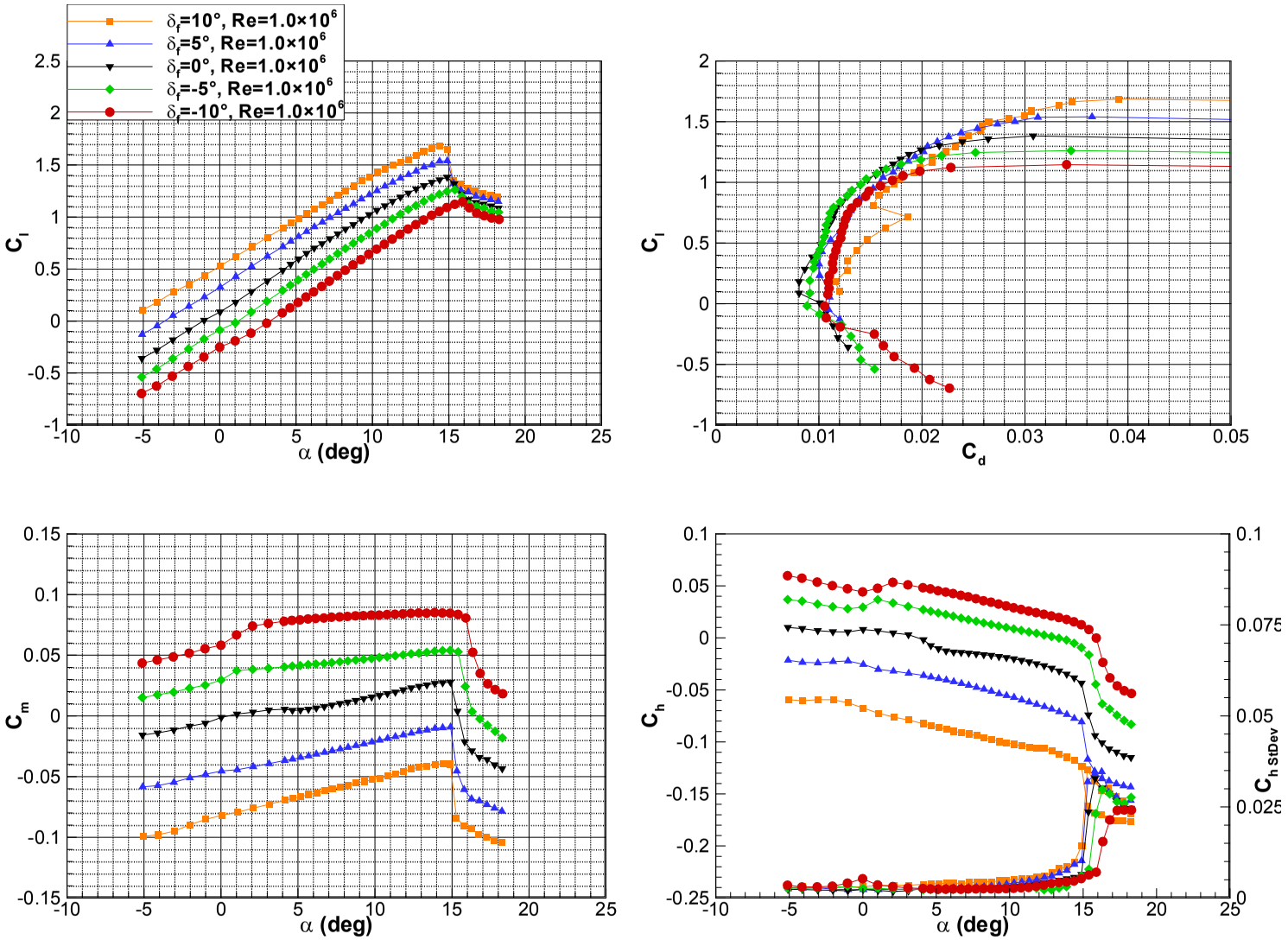

Fig. 3.17 Clean NACA 23012 performance with flap deflections at Re = 1.0 × 10^6.

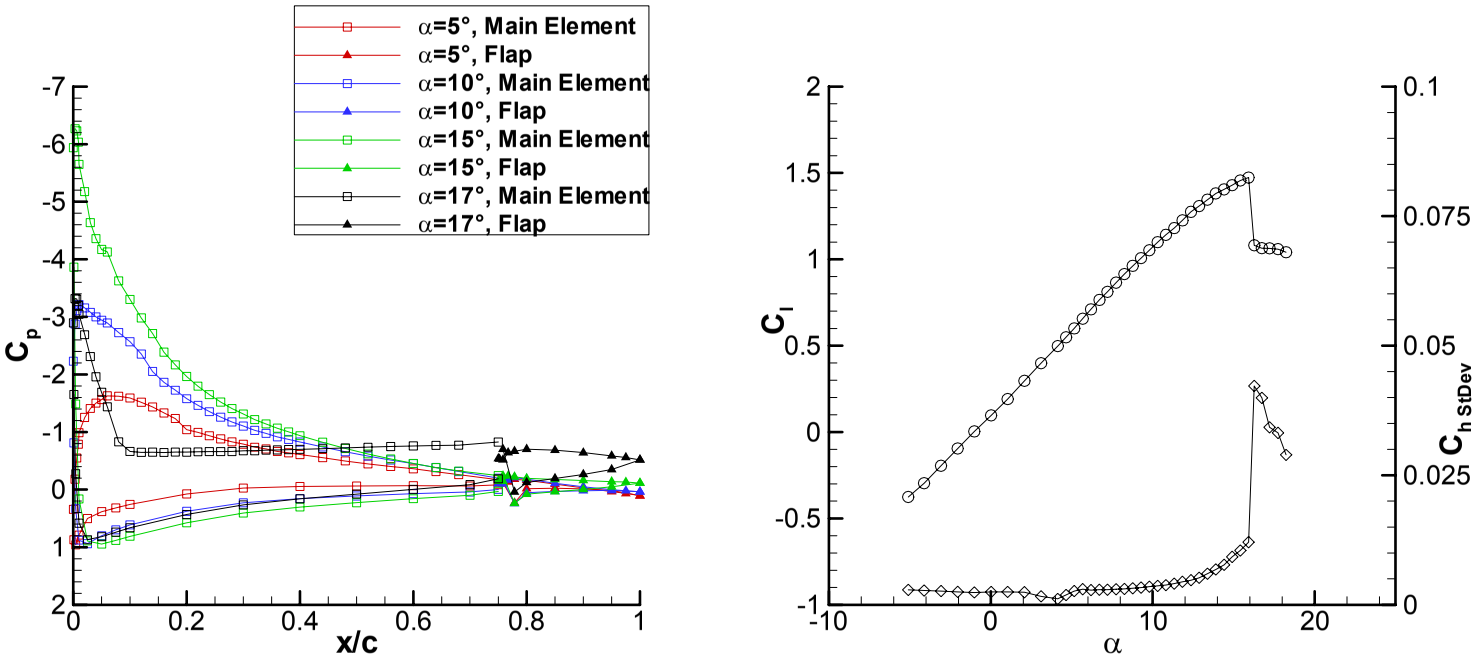

Fig. 3.18 NACA 23012 clean surface C_p distributions with C_l and $C_{h,StDev}$ comparison for Re = 1.8 × 10^6 and $\delta_f = 0°$.

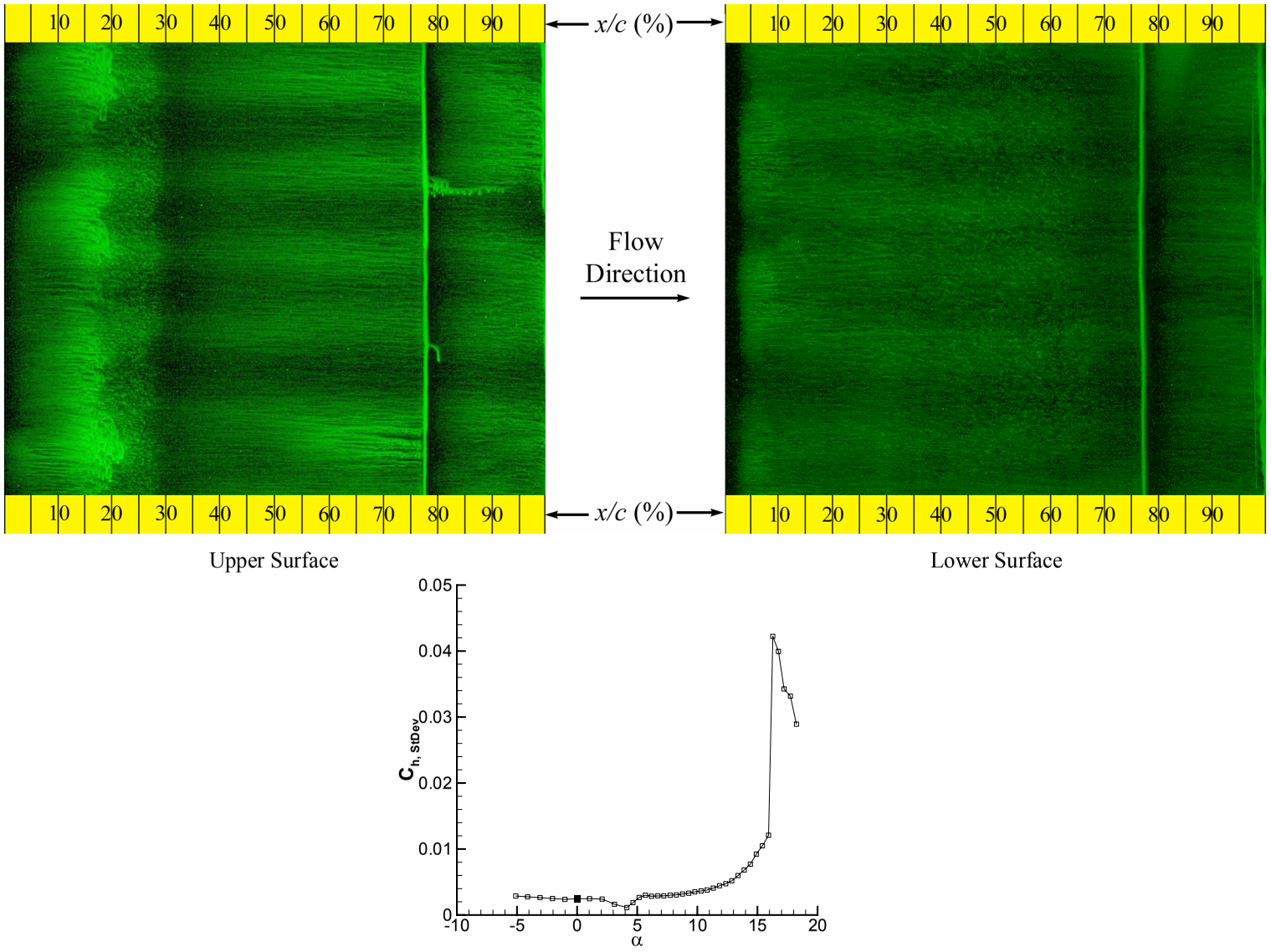

Fig. 3.19 Fluorescent oil-flow visualization of clean NACA 23012 at $\alpha = 0°$, Re = 1.8×10^6 and corresponding $C_{h,StDev}$.

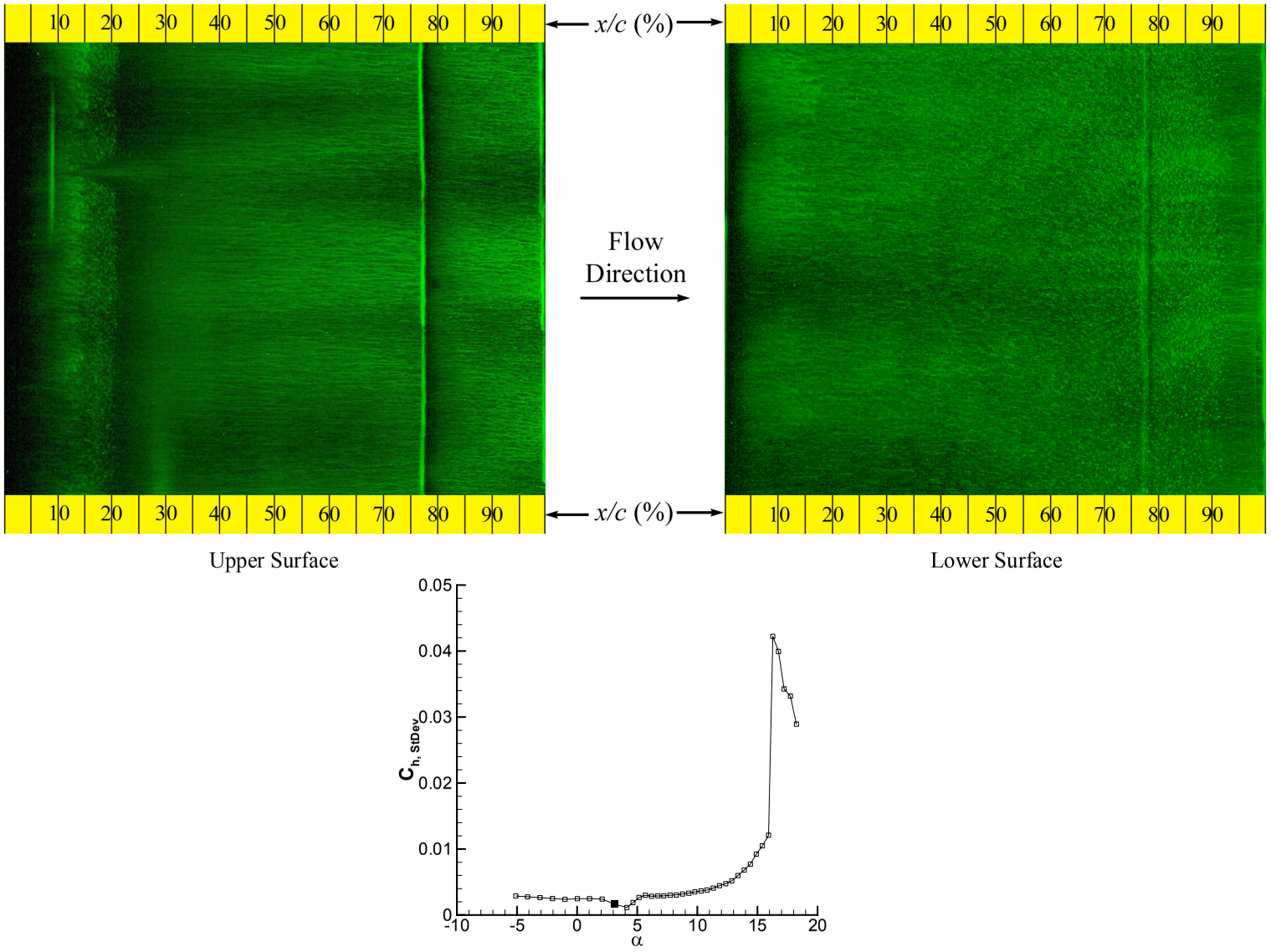

Fig. 3.20 Fluorescent oil-flow visualization of clean NACA 23012 at $\alpha = 3°$, Re = 1.8×10^6 and corresponding $C_{h,StDev}$.

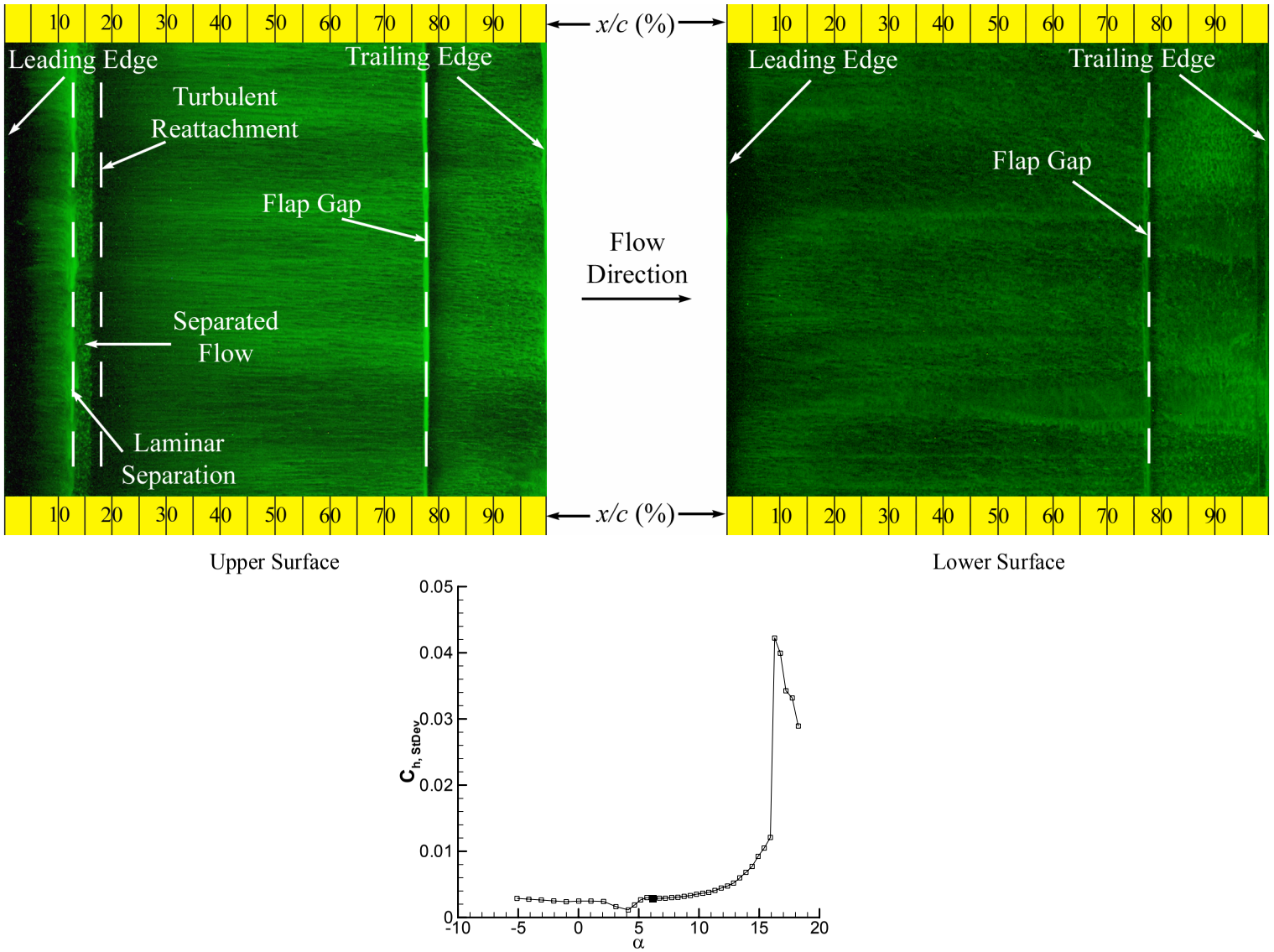

Fig. 3.21 Fluorescent oil-flow visualization of clean NACA 23012 at $\alpha = 6°$, Re = 1.8×10^6 and corresponding $C_{h,StDev}$.

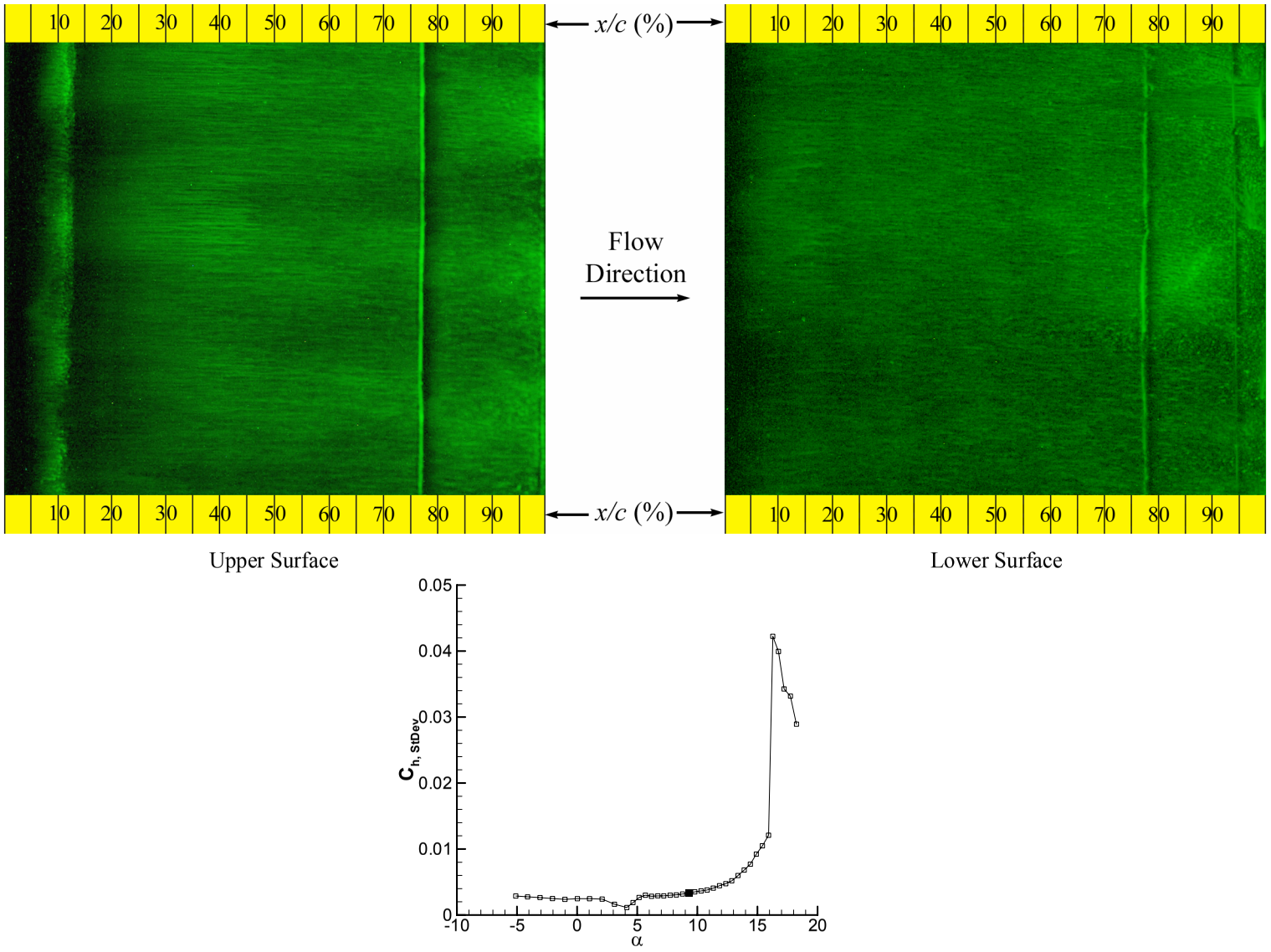

Fig. 3.22 Fluorescent oil-flow visualization of clean NACA 23012 at $\alpha = 9°$, Re = 1.8×10^6 and corresponding $C_{h,StDev}$.

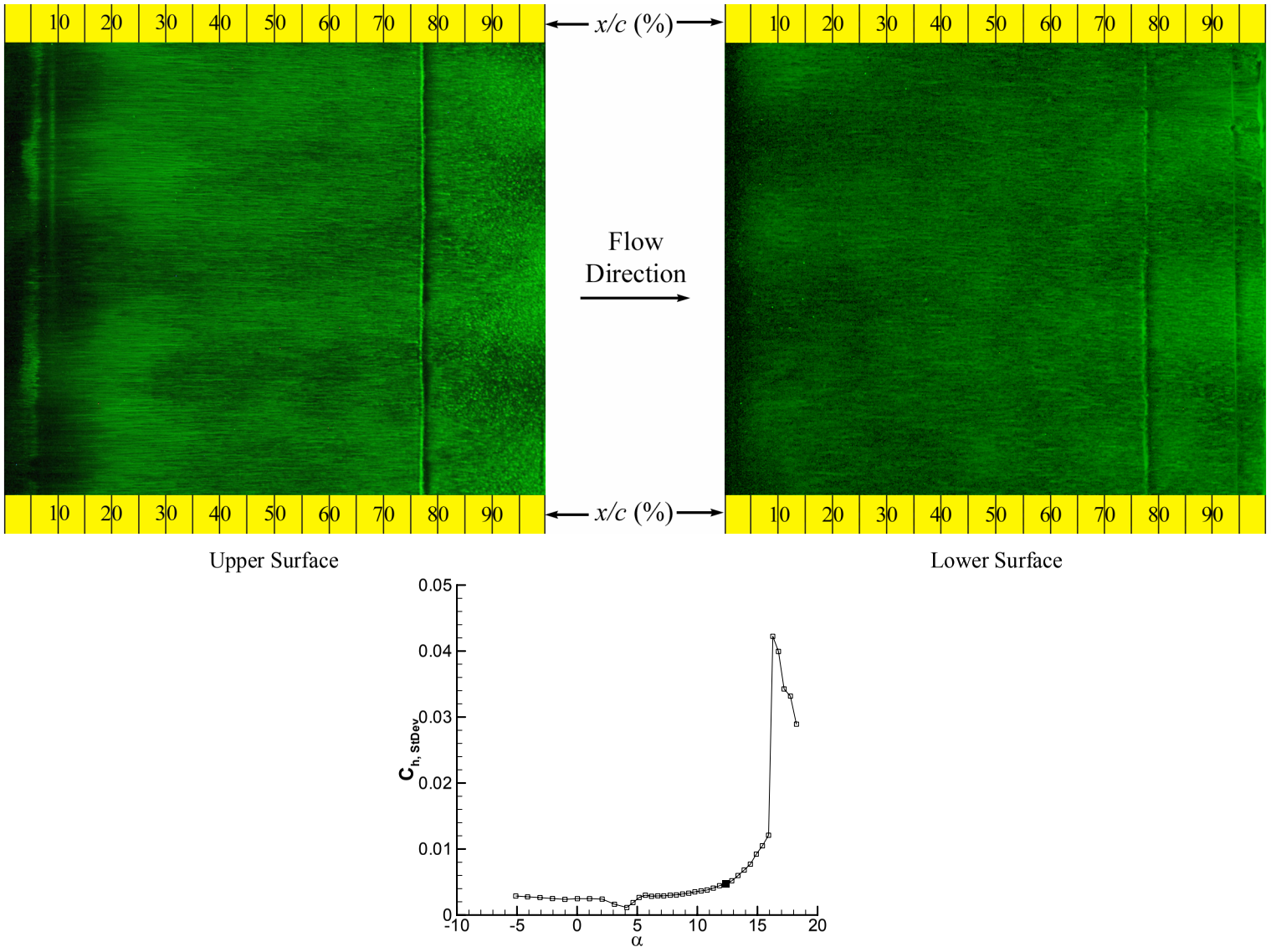

Fig. 3.23 Fluorescent oil-flow visualization of clean NACA 23012 at α = 12°, Re = 1.8 × 10^6 and corresponding $C_{h,StDev}$.

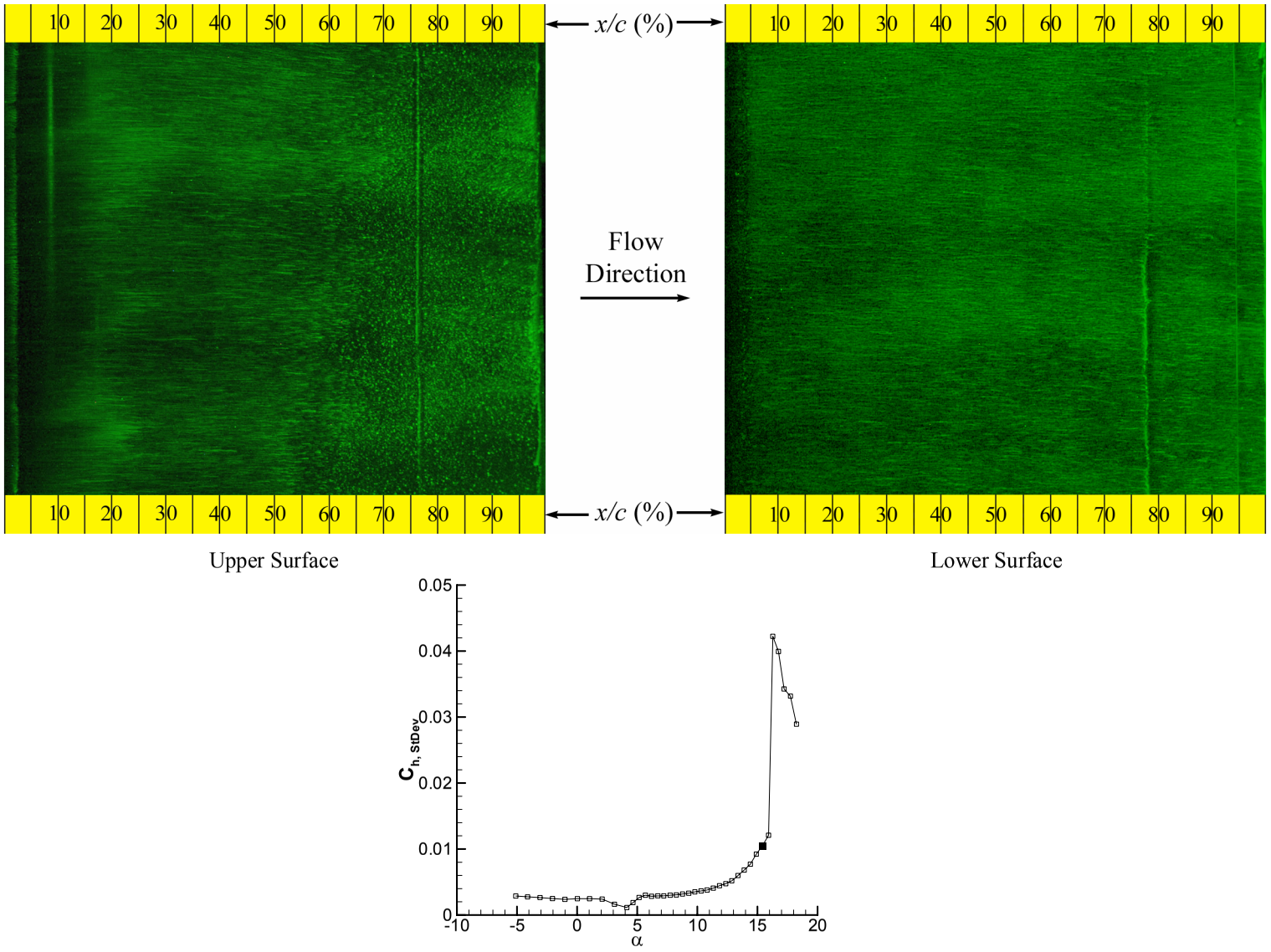

Fig. 3.24 Fluorescent oil-flow visualization of clean NACA 23012 at α = 15°, Re = 1.8 × 10^6 and corresponding $C_{h,StDev}$.

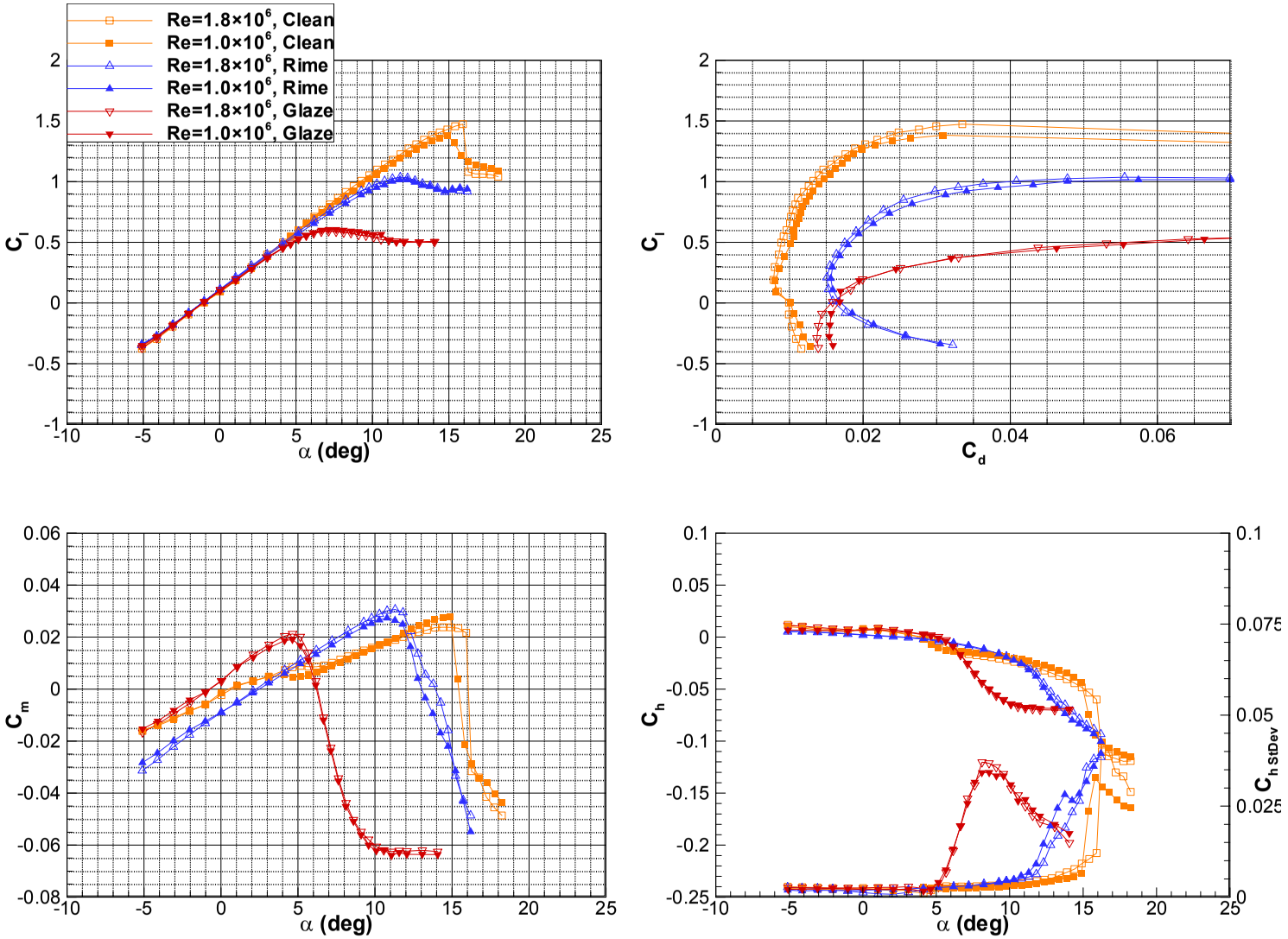

Fig. 3.25 NACA 23012 performance with simulated ice contamination, at flap setting of 0°.

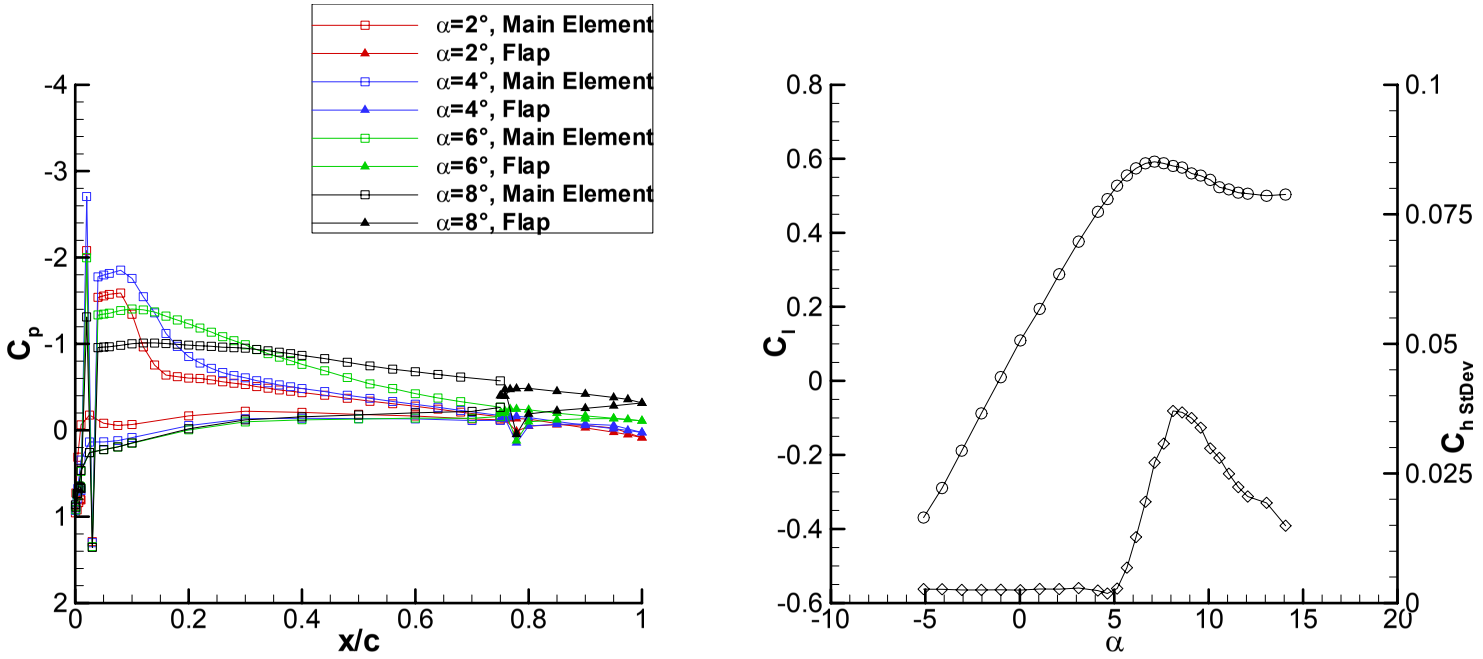

Fig. 3.26 NACA 23012 with simulated glaze ice surface C_p distributions with C_l and $C_{h,StDev}$ comparison for Re = 1.8 × 10^6 and $\delta_f = 0°$.

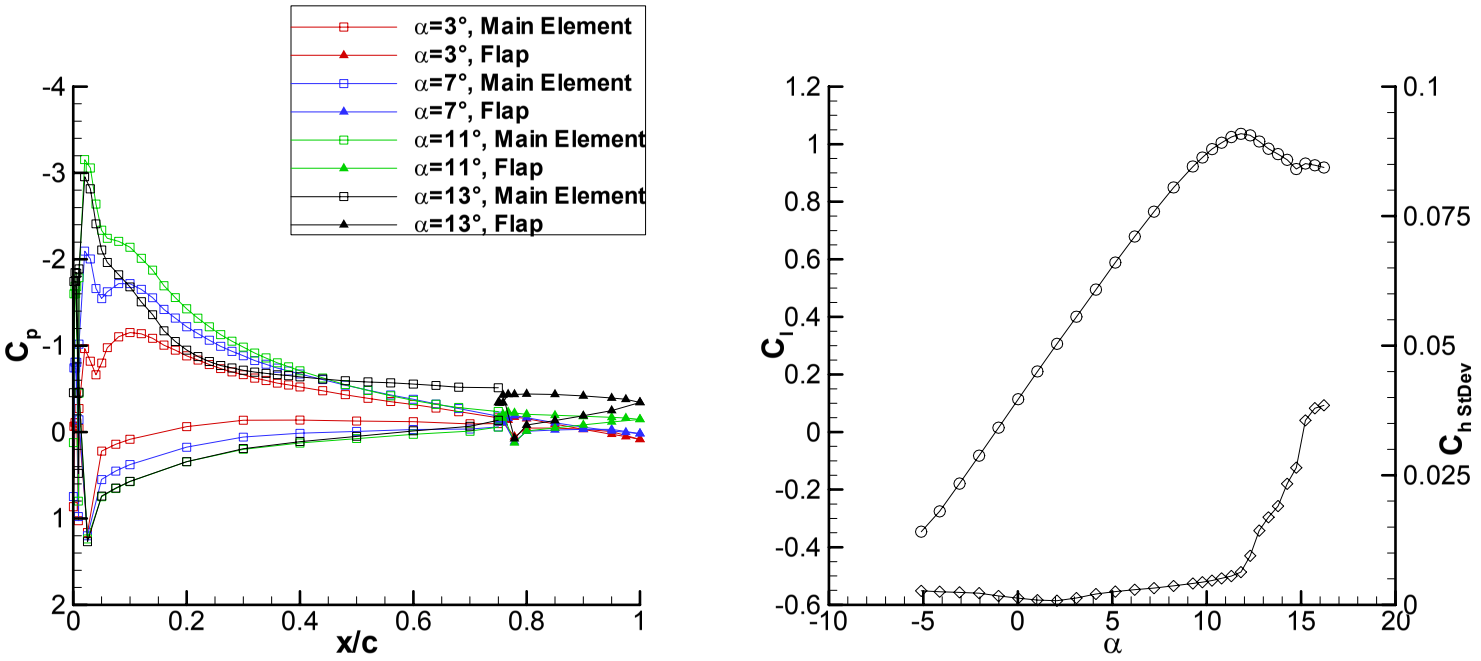

Fig. 3.27 NACA 23012 with simulated rime ice surface C_p distributions with C_l and $C_{h,StDev}$ comparison for Re = 1.8 × 10^6 and $\delta_f = 0°$.

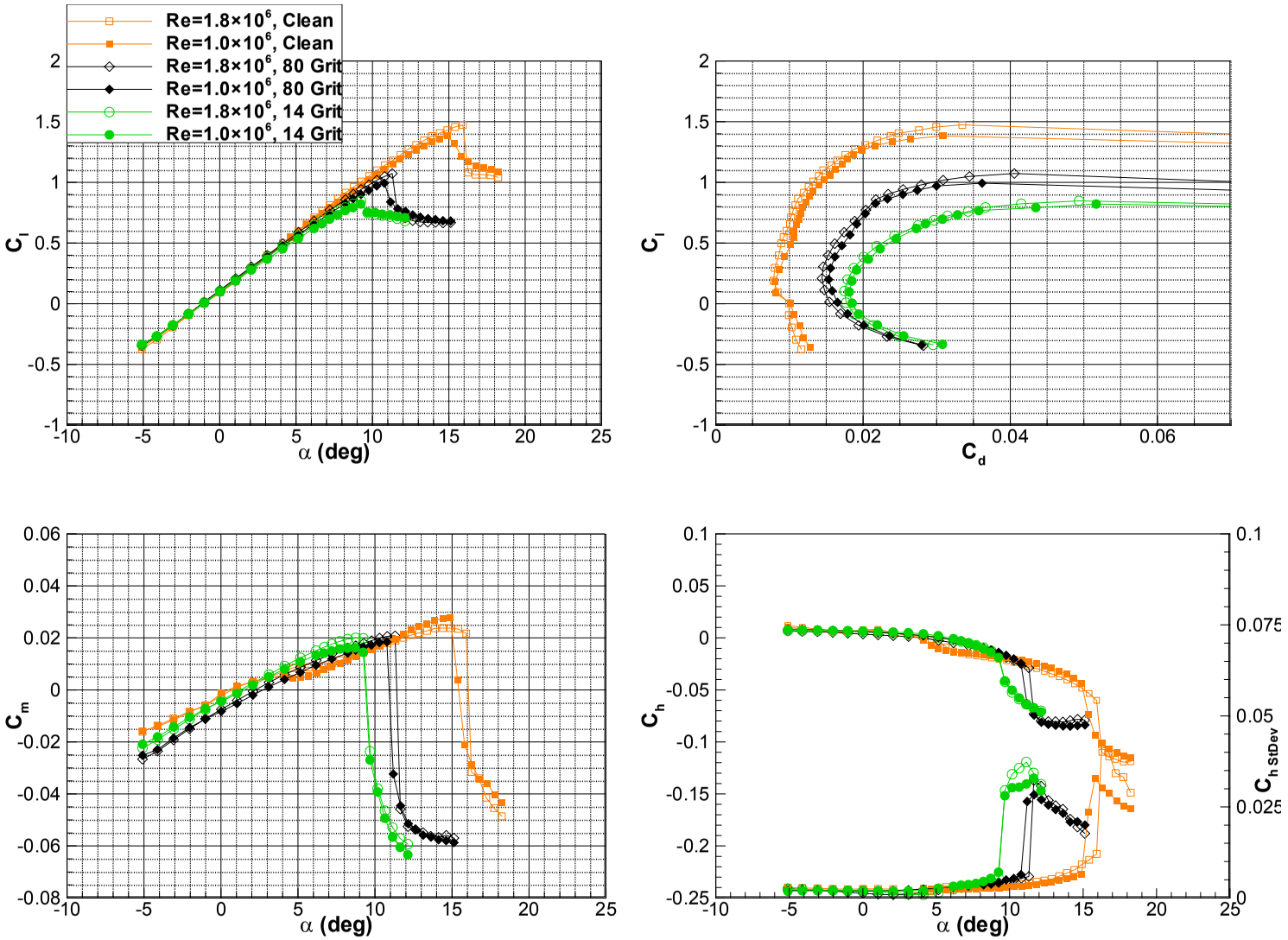

Fig. 3.28 NACA 23012 performance with leading-edge roughness, at flap setting of 0°.

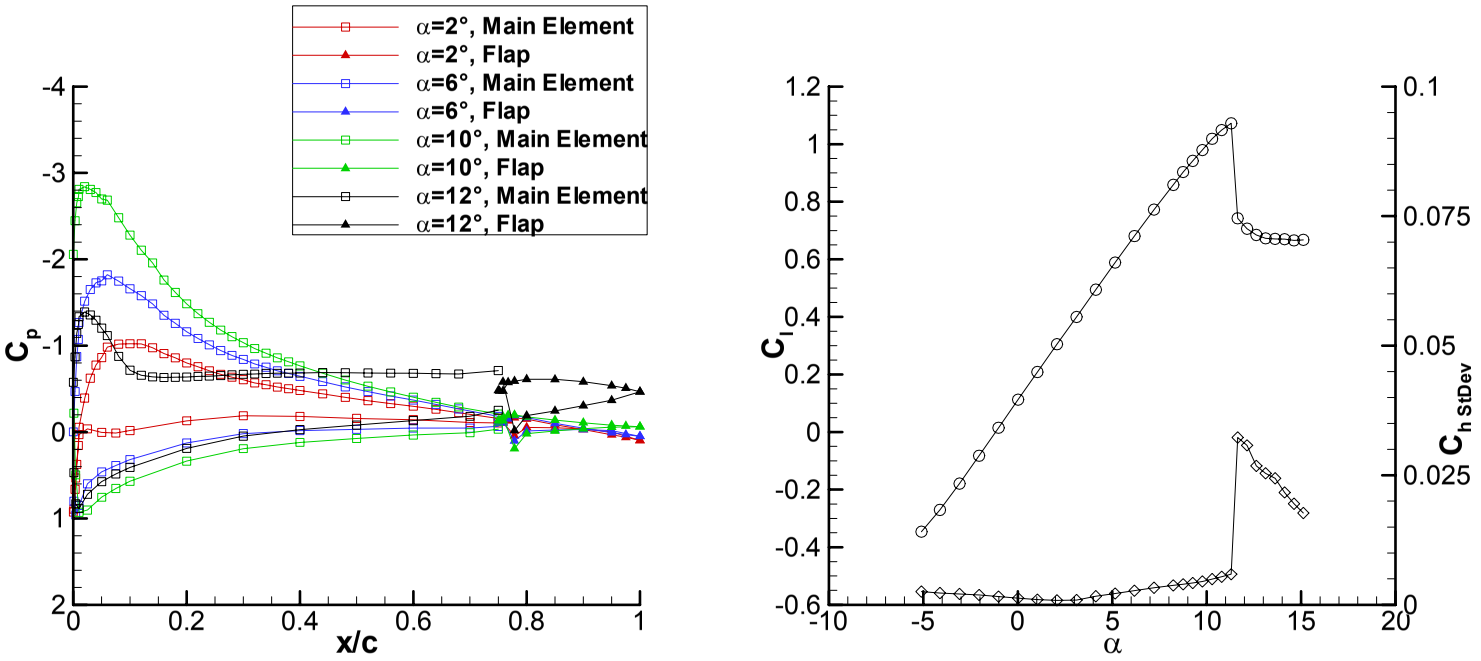

Fig. 3.29 NACA 23012 with 80-grit roughness surface C_p distributions with C_l and $C_{h,StDev}$ comparison for Re = 1.8 × 10^6 and δ_f = 0°.

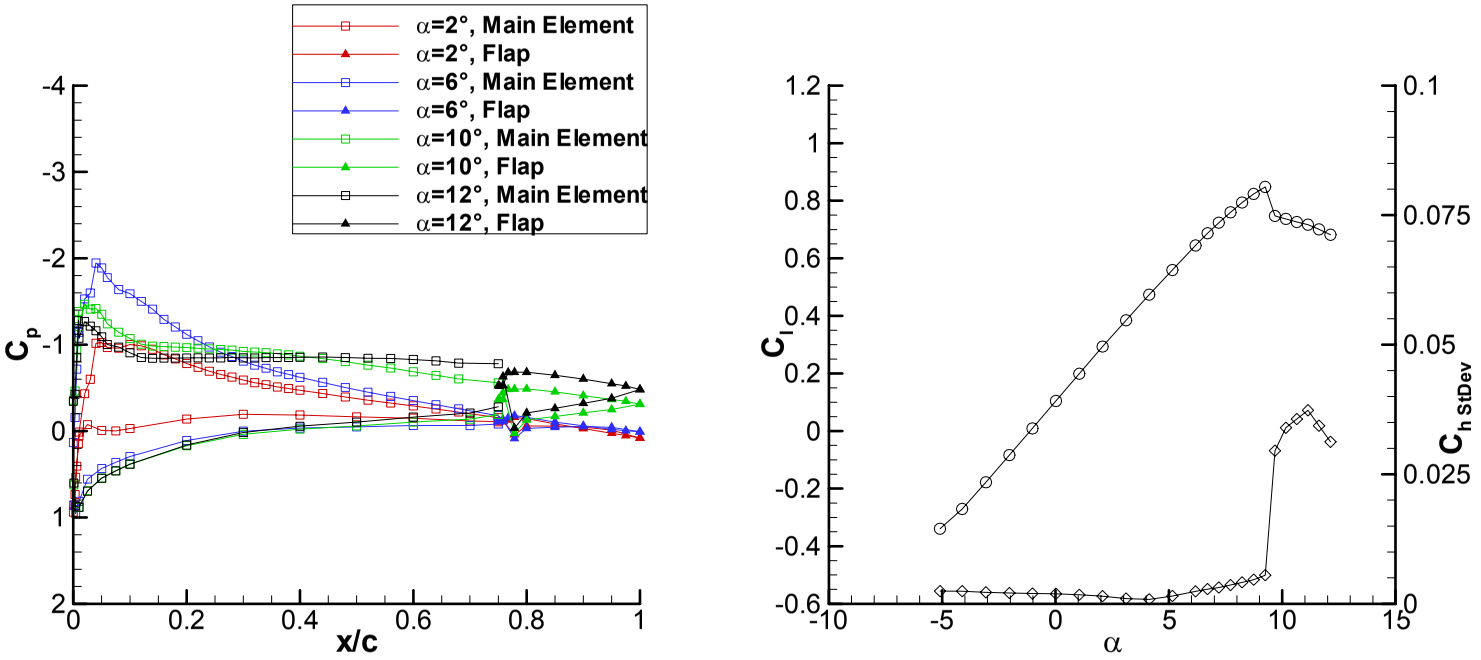

Fig. 3.30 NACA 23012 with 14-grit roughness surface C_p distributions with C_l and $C_{h,StDev}$ comparison for Re = 1.8 × 10^6 and δ_f = 0°.

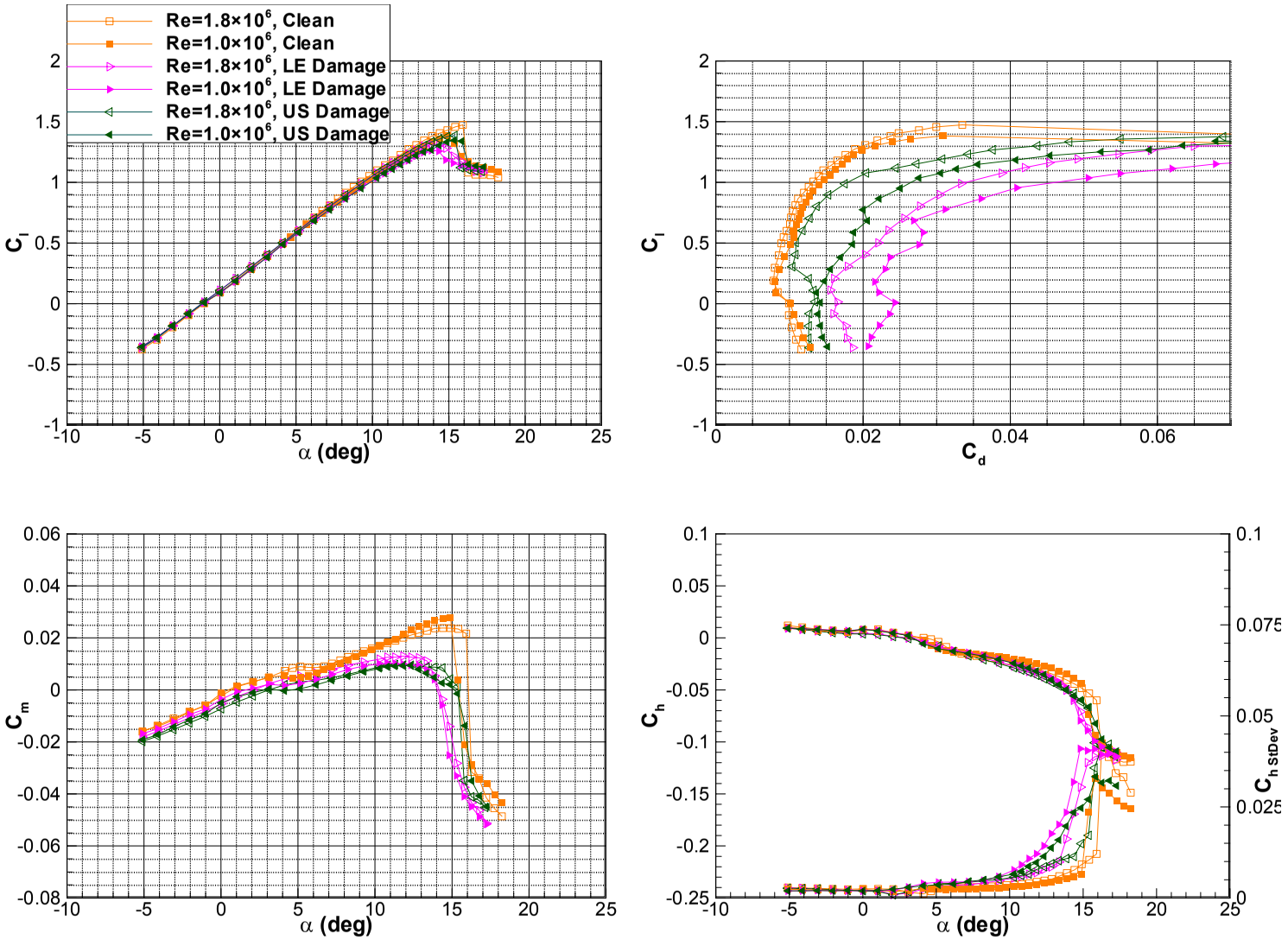

Fig. 3.31 NACA 23012 performance with simulated damage, at flap setting of 0°.

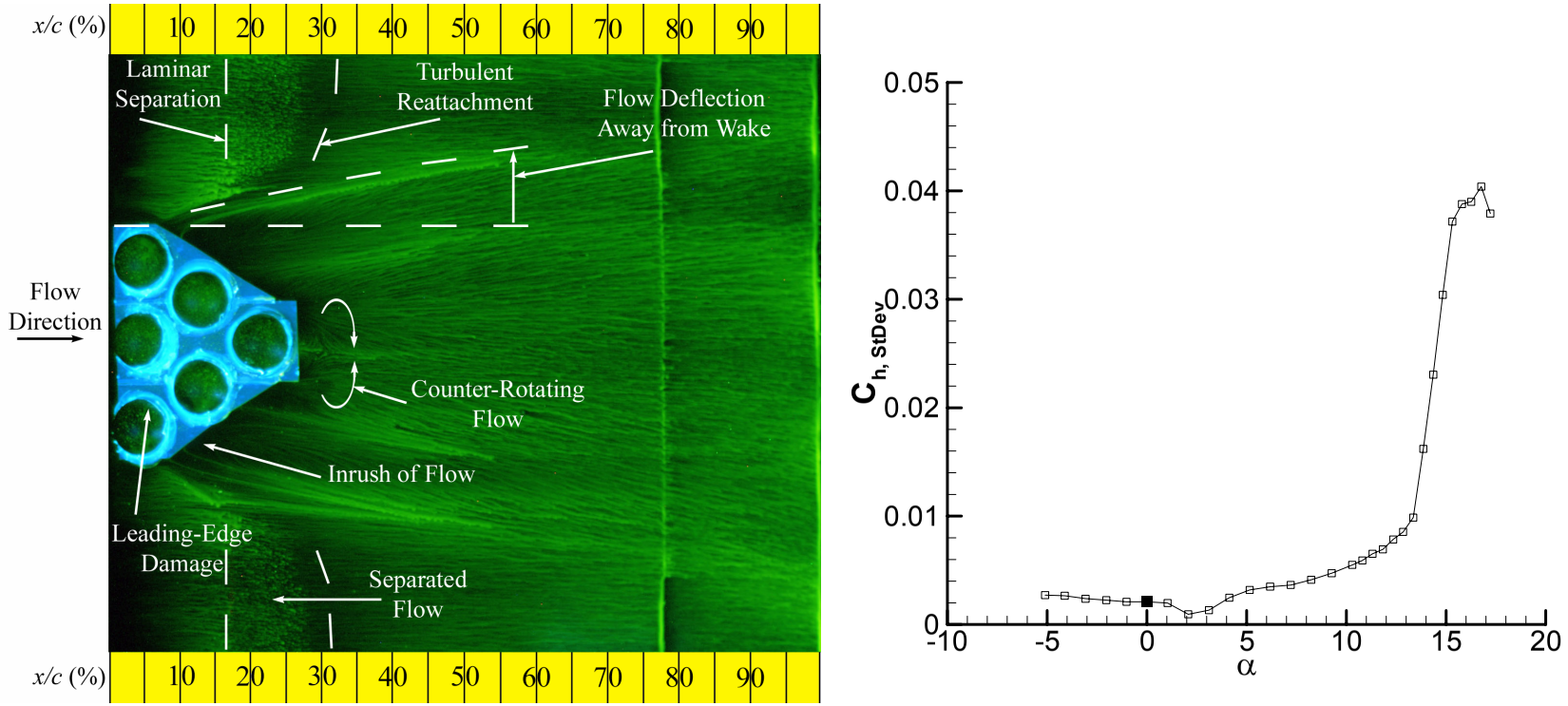

Fig. 3.32 Fluorescent oil-flow visualization of NACA 23012 with simulated leading-edge damage at $\alpha = 0°$, Re = 1.8×10^6 and corresponding $C_{h,StDev}$.

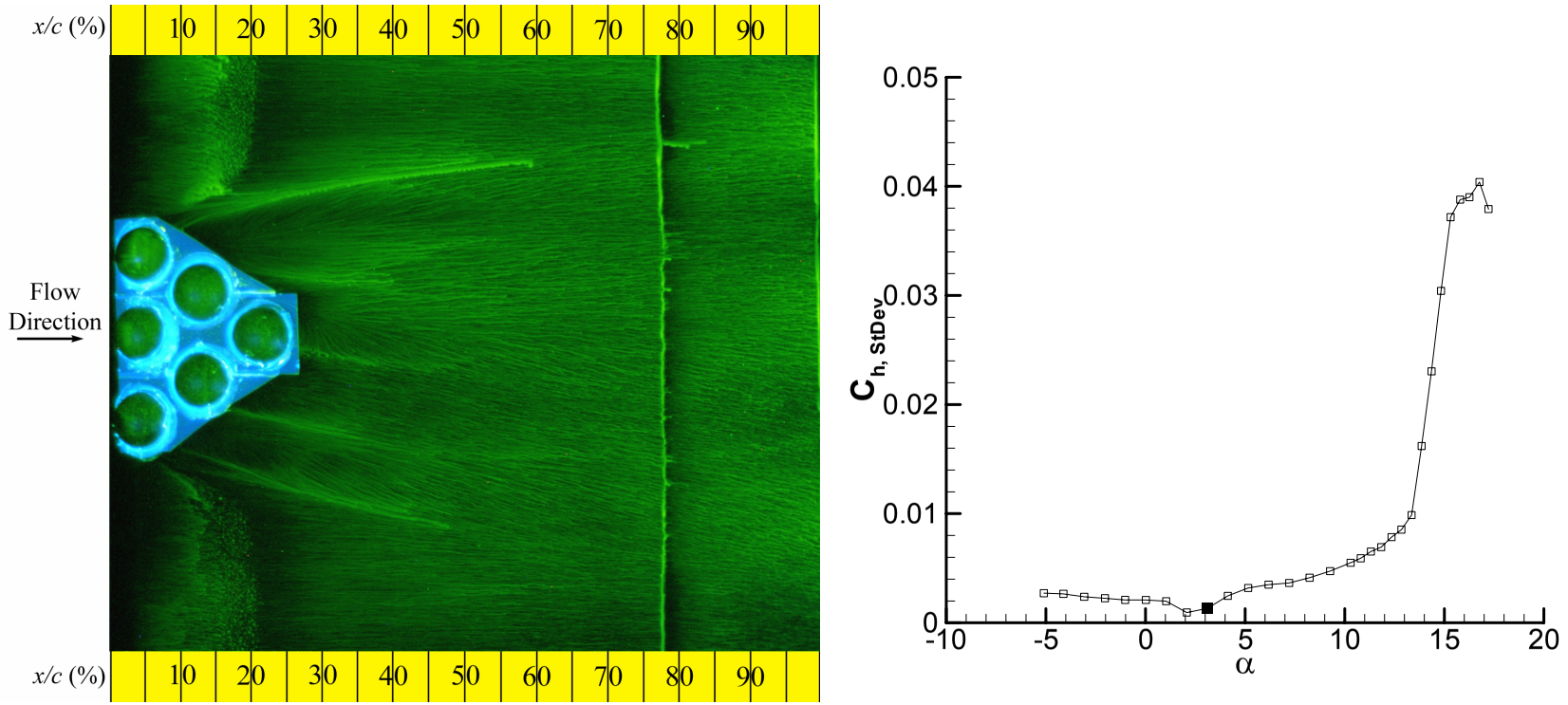

Fig. 3.33 Fluorescent oil-flow visualization of NACA 23012 with simulated leading-edge damage at $\alpha = 3°$, Re = 1.8×10^6 and corresponding $C_{h,StDev}$.

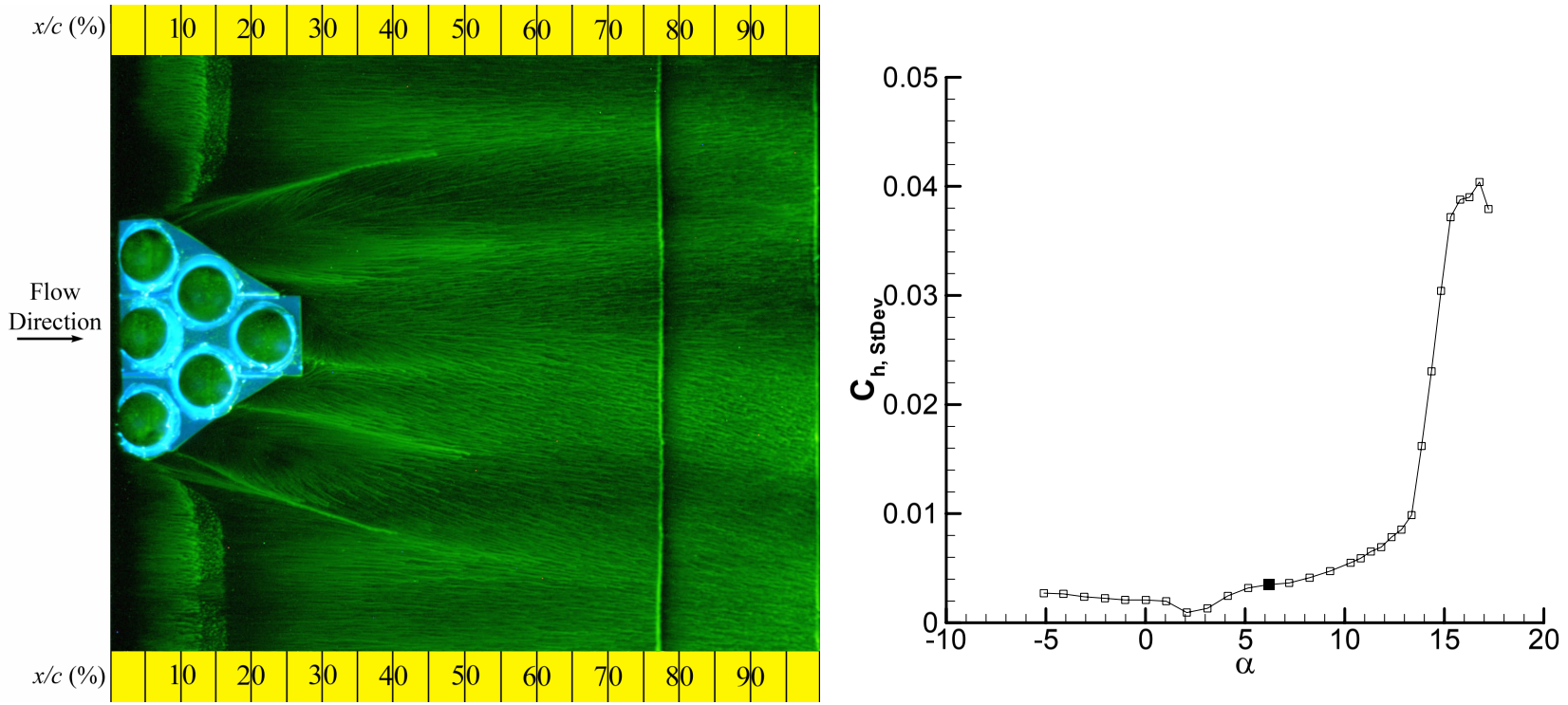

Fig. 3.34 Fluorescent oil-flow visualization of NACA 23012 with simulated leading-edge damage at $\alpha = 6°$, Re = 1.8×10^6 and corresponding $C_{h,StDev}$.

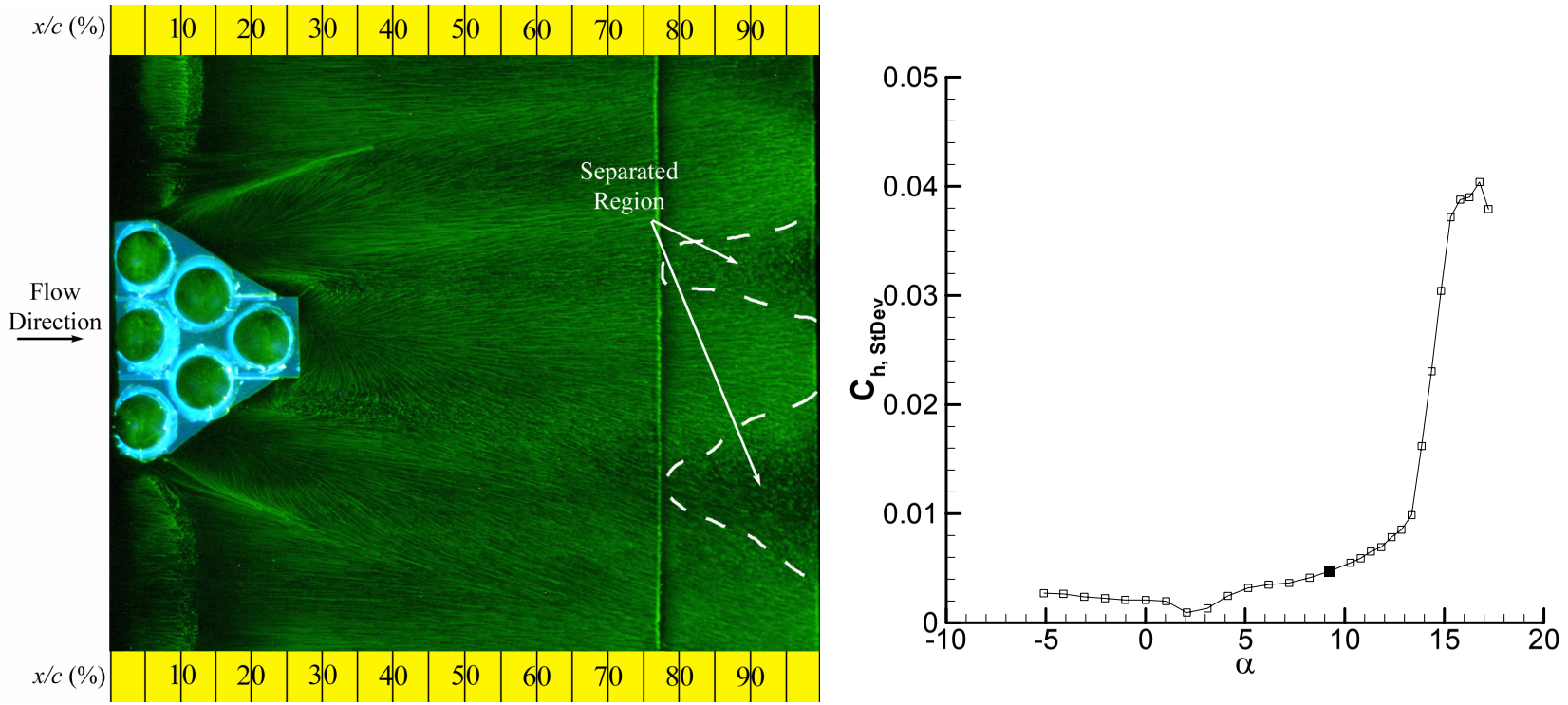

Fig. 3.35 Fluorescent oil-flow visualization of NACA 23012 with simulated leading-edge damage at $\alpha = 9°$, Re = 1.8×10^6 and corresponding $C_{h,StDev}$.

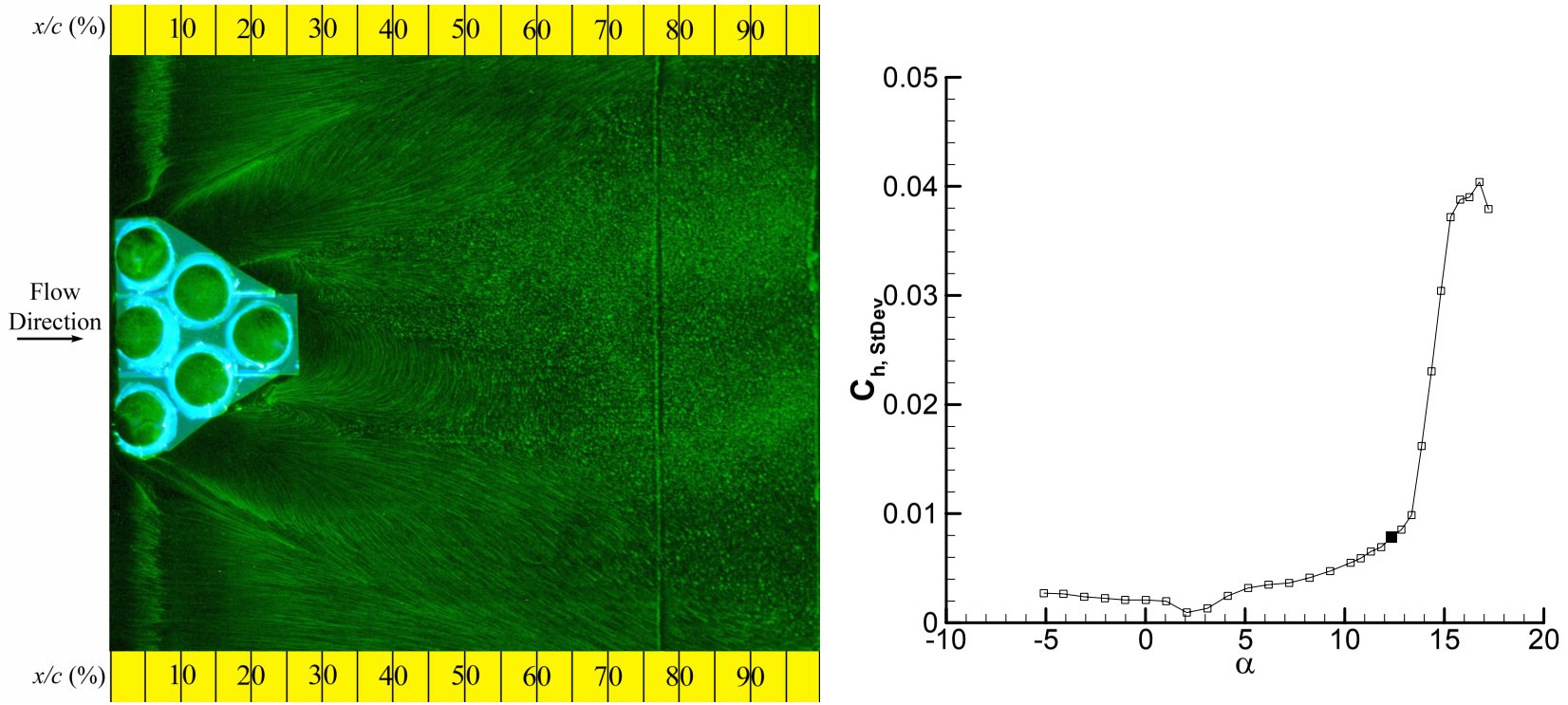

Fig. 3.36 Fluorescent oil-flow visualization of NACA 23012 with simulated leading-edge damage at α = 12°, Re = 1.8 × 10^6 and corresponding $C_{h,StDev}$.

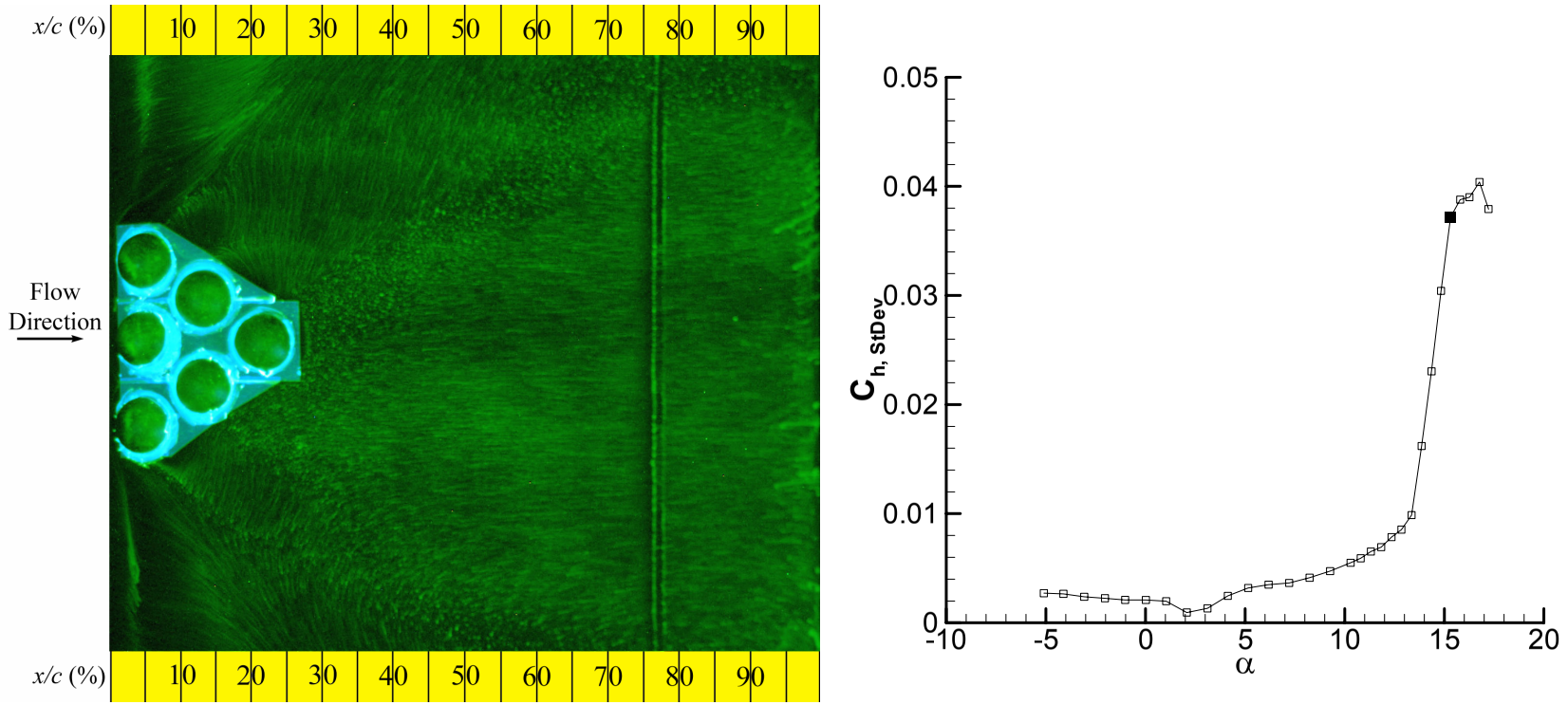

Fig. 3.37 Fluorescent oil-flow visualization of NACA 23012 with simulated leading-edge damage at α = 15°, Re = 1.8 × 10^6 and corresponding $C_{h,StDev}$.

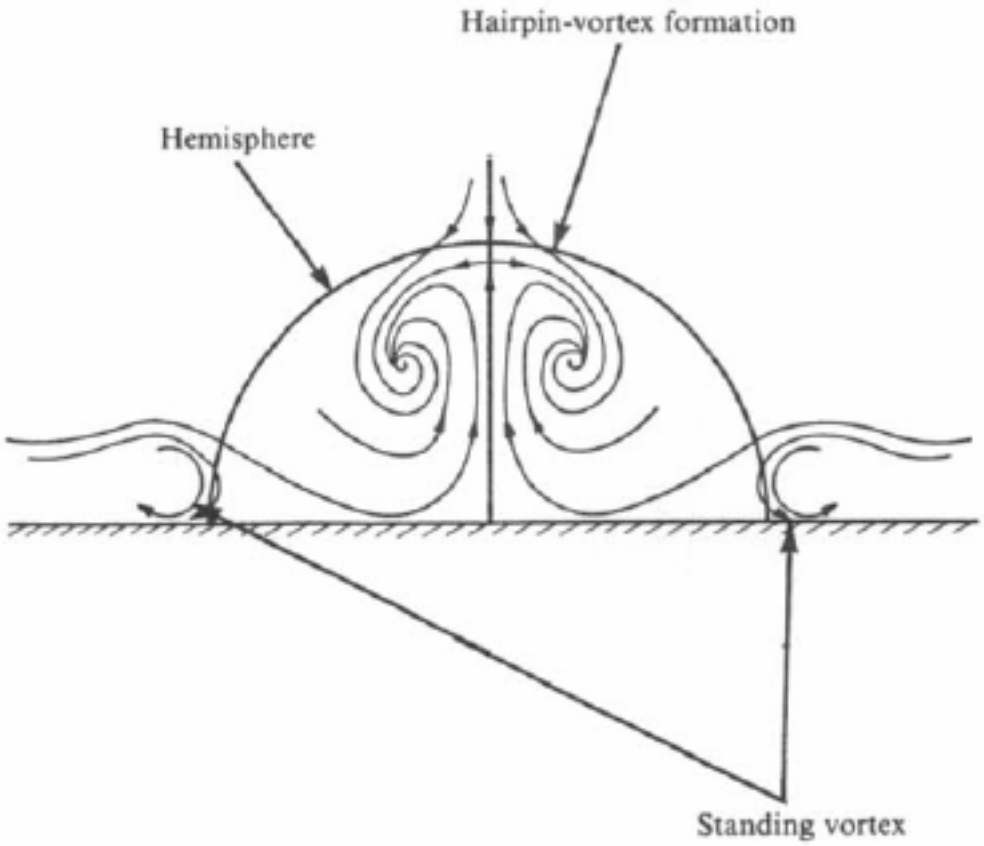

Fig. 3.38 Cross-sectional schematic of flow structures over a hemisphere, after Alcar and Smith.[27]

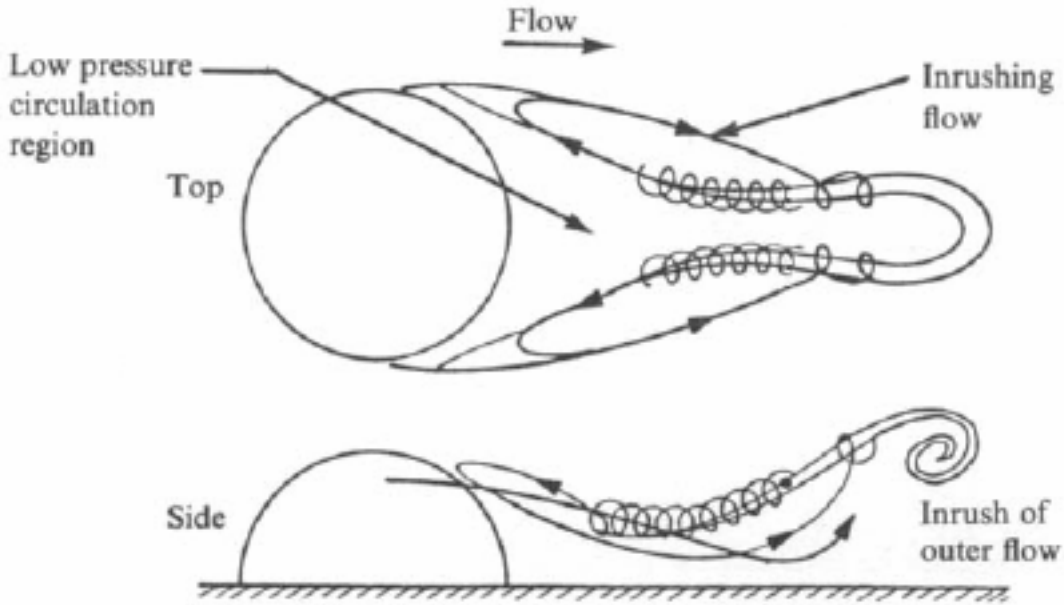

Fig. 3.39 Schematic of flow over a hemisphere showing inrush of outer flow, after Alcar and Smith.[27]

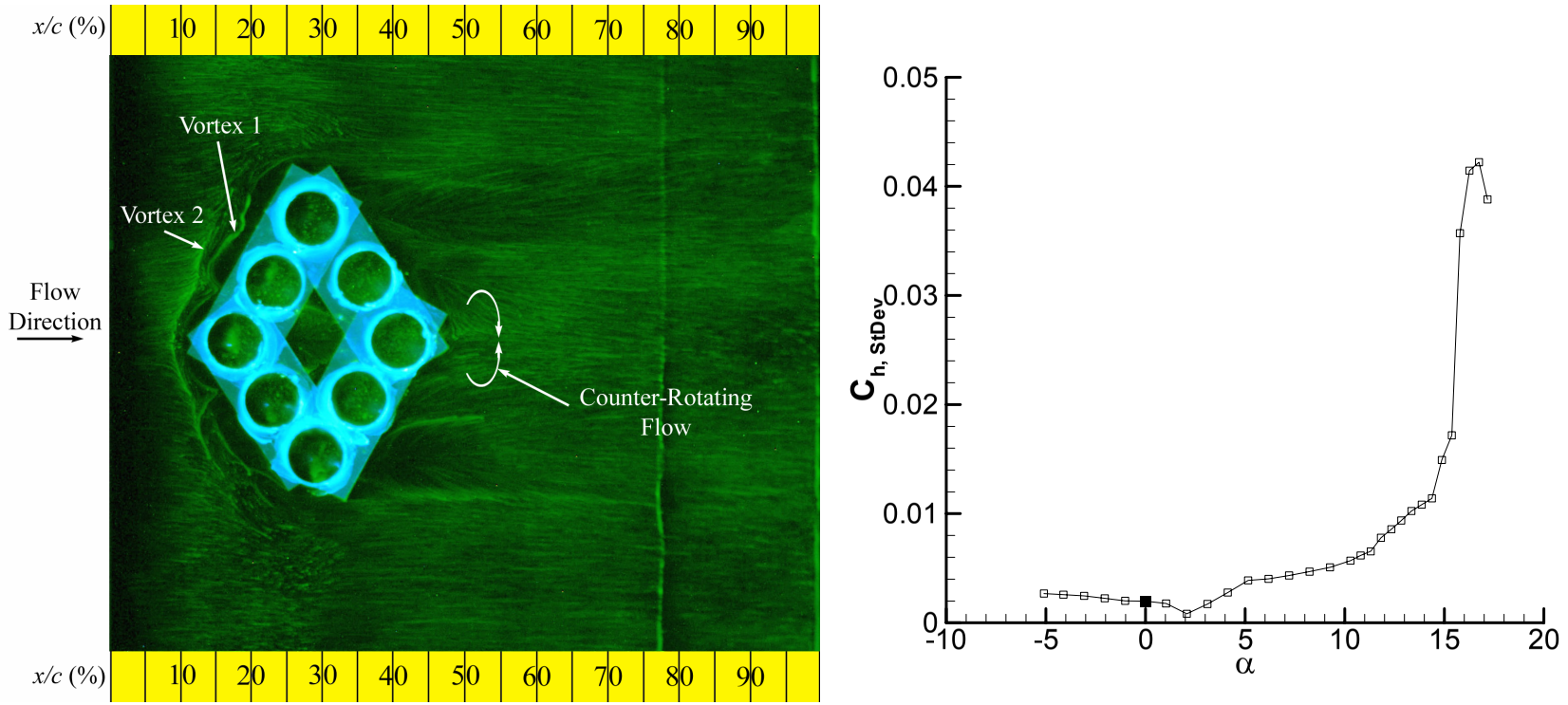

Fig. 3.40 Fluorescent oil-flow visualization of NACA 23012 with simulated upper-surface damage at $\alpha = 0°$, Re = 1.8×10^6 and corresponding $C_{h,StDev}$.

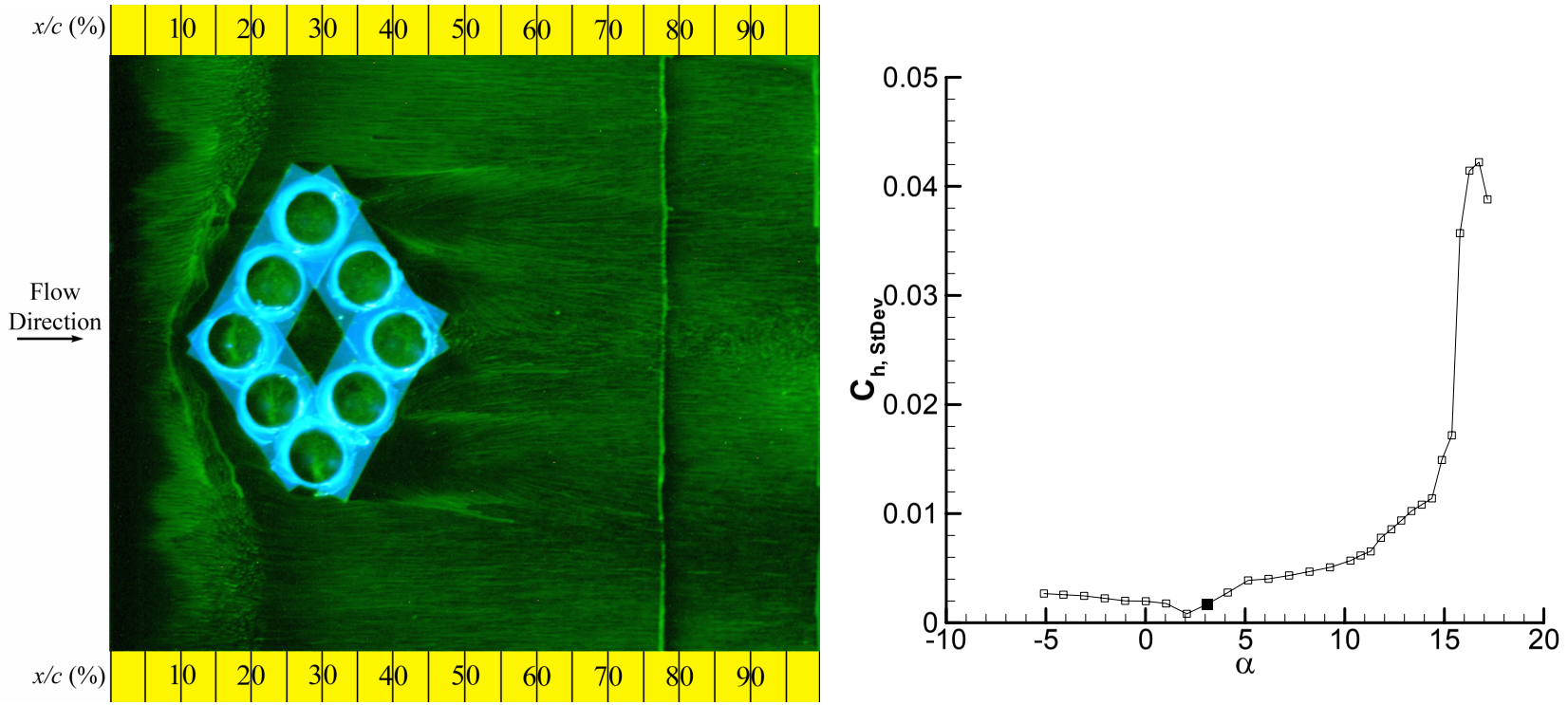

Fig. 3.41 Fluorescent oil-flow visualization of NACA 23012 with simulated upper-surface damage at $\alpha = 3°$, Re = 1.8×10^6 and corresponding $C_{h,StDev}$.

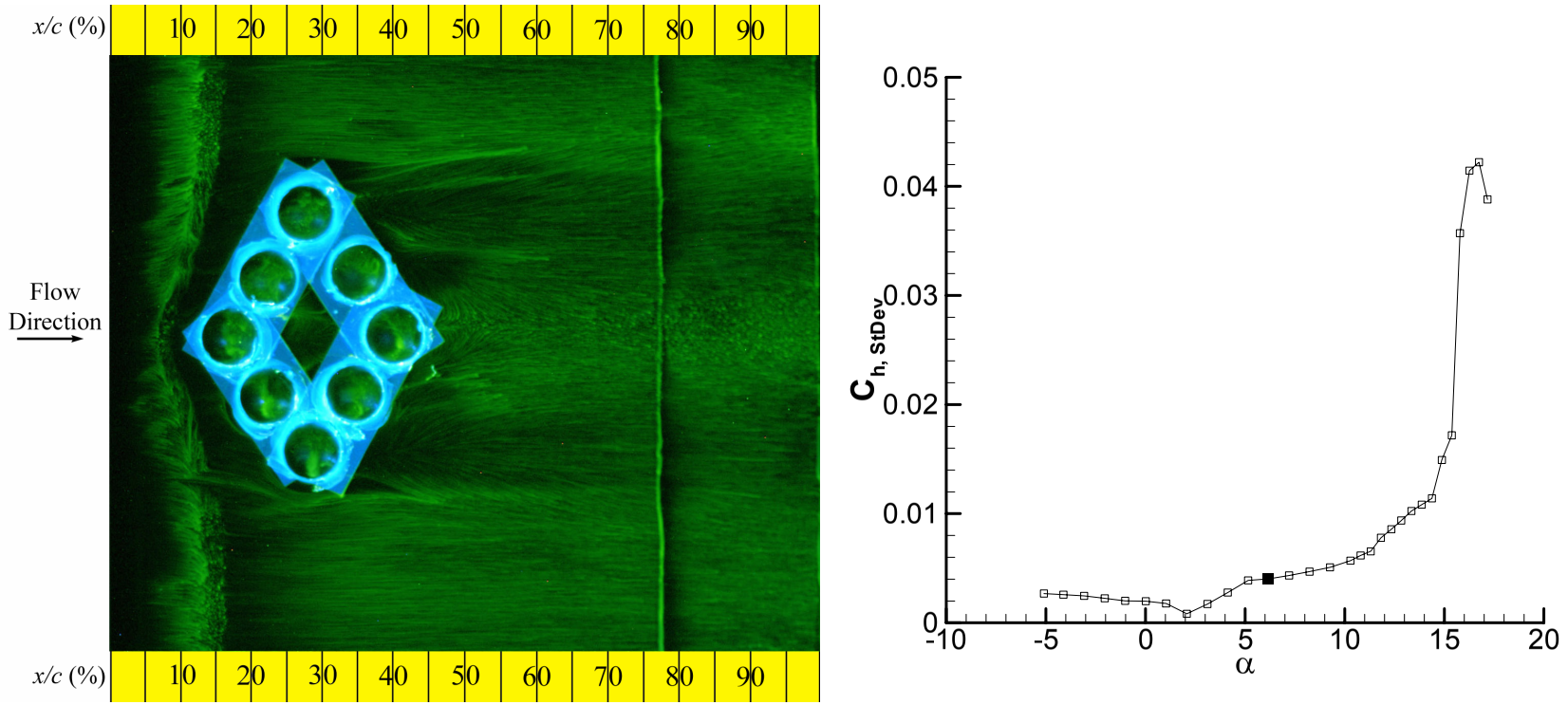

Fig. 3.42 Fluorescent oil-flow visualization of NACA 23012 with simulated upper-surface damage at $\alpha = 6°$, Re = 1.8×10^6 and corresponding $C_{h,StDev}$.

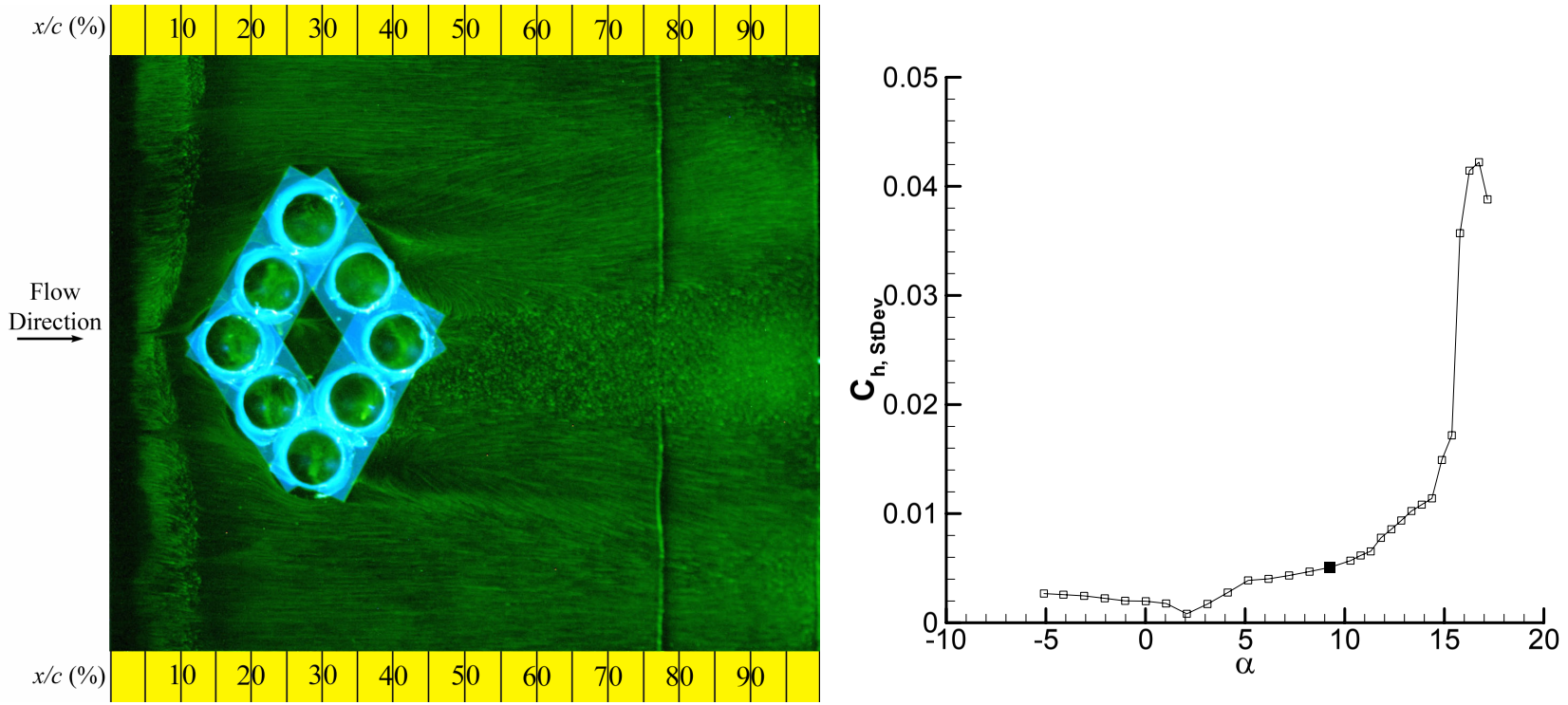

Fig. 3.43 Fluorescent oil-flow visualization of NACA 23012 with simulated upper-surface damage at $\alpha = 9°$, Re = 1.8×10^6 and corresponding $C_{h,StDev}$.

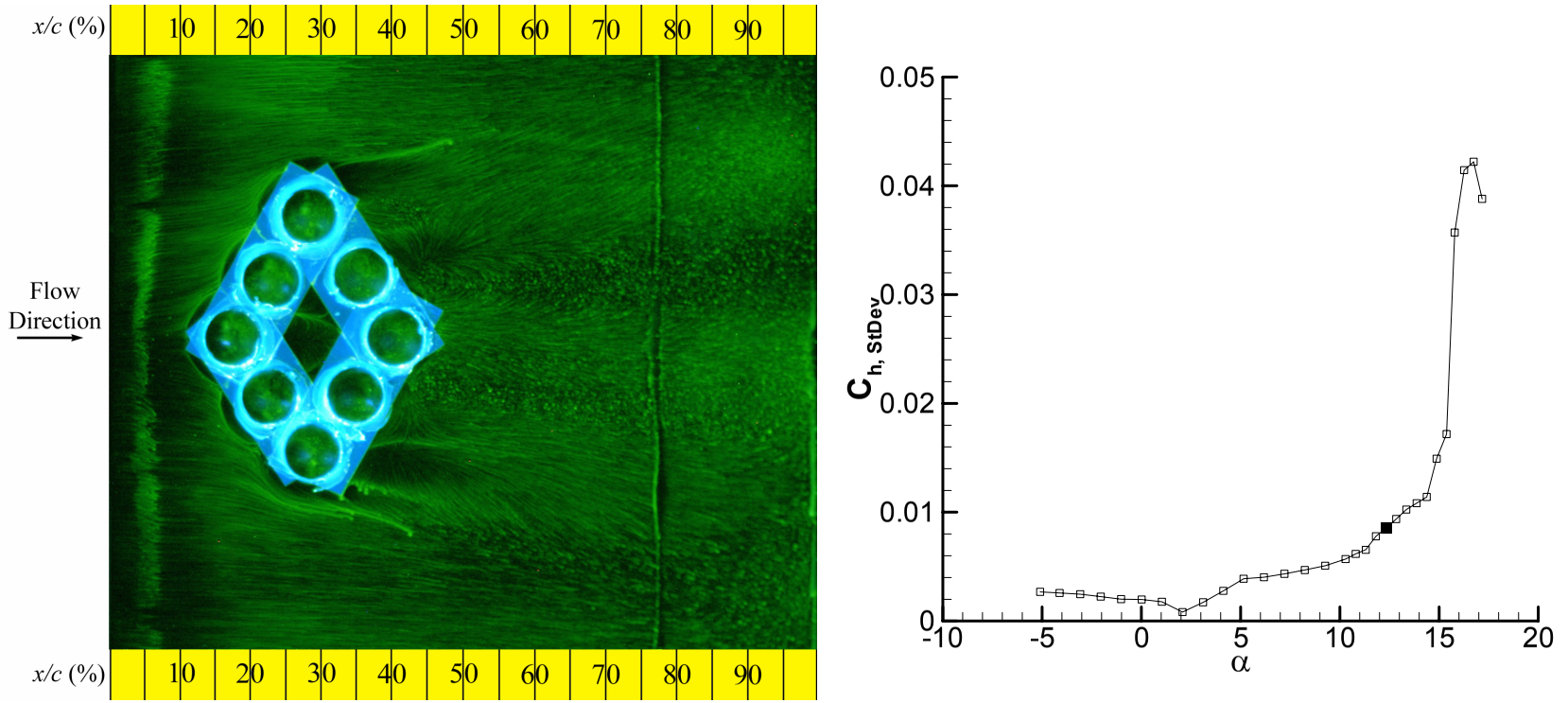

Fig. 3.44 Fluorescent oil-flow visualization of NACA 23012 with simulated upper-surface damage at $\alpha = 12°$, Re = 1.8×10^6 and corresponding $C_{h,StDev}$.

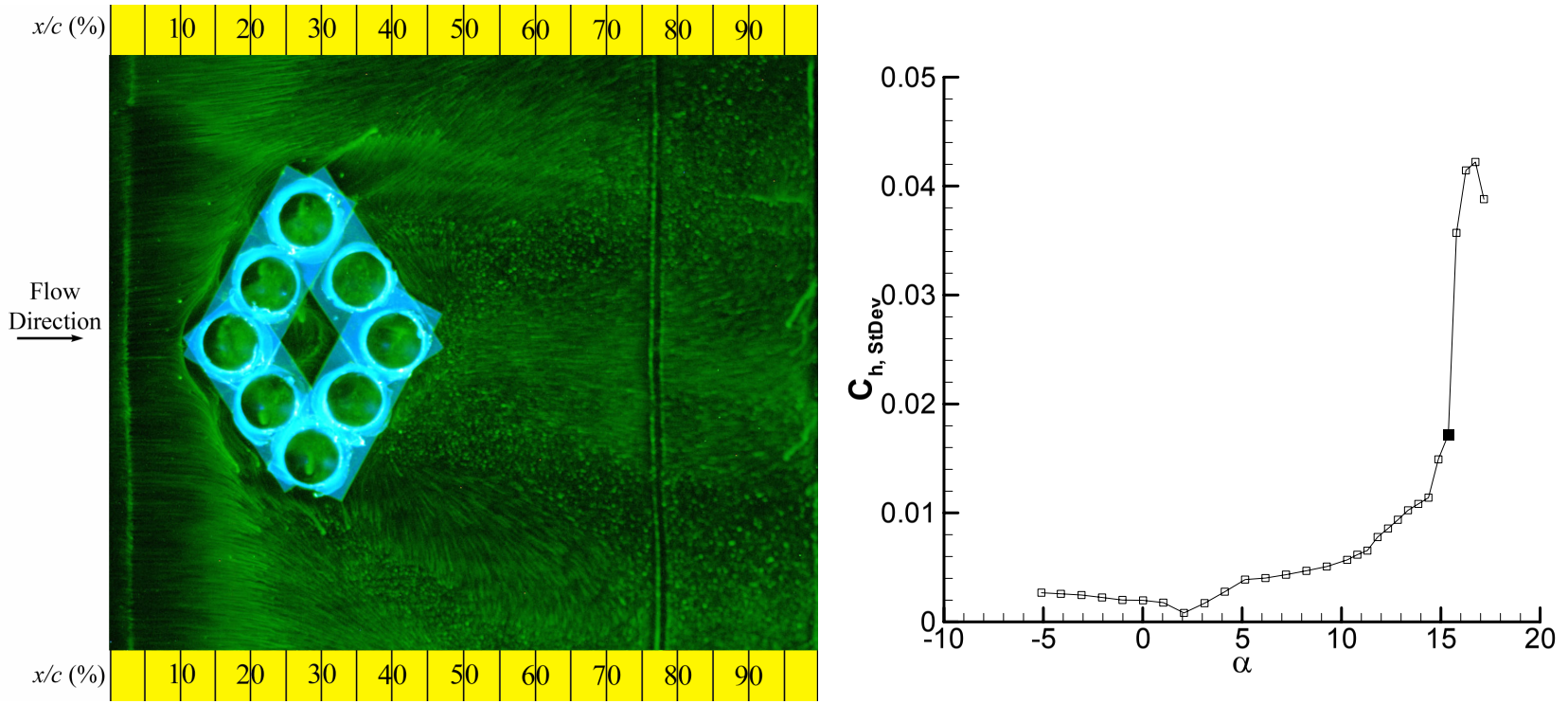

Fig. 3.45 Fluorescent oil-flow visualization of NACA 23012 with simulated upper-surface damage at $\alpha = 15°$, Re = 1.8×10^6 and corresponding $C_{h,StDev}$.

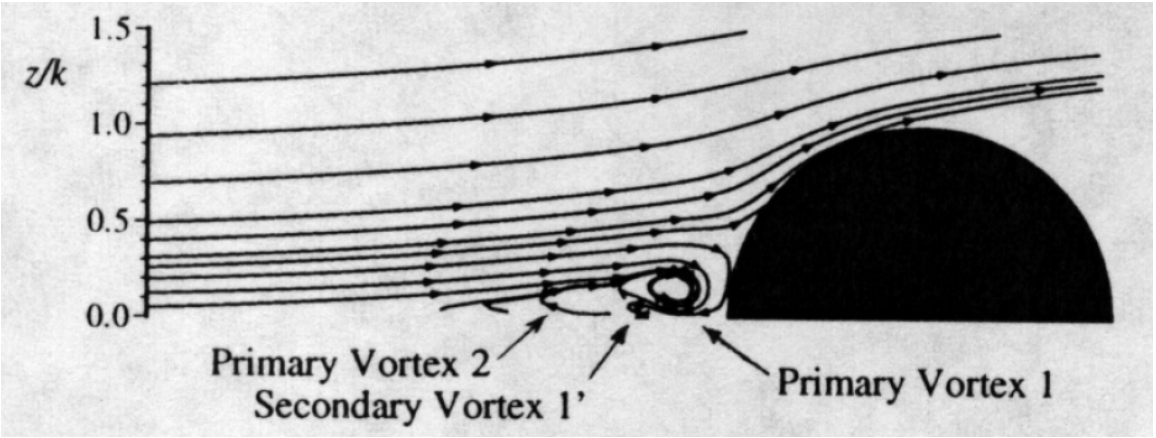

Fig. 3.46 Local flowfield upstream of distributed roughness, after Winkler and Bragg.[31]

Chapter 4

Summary, Conclusions, and Recommendations

4.1 Summary

This experimental investigation was performed on two airfoil models – an NACA 3415 and an NACA 23012. Both models had an 18-inch chord with a 25% simple flap. The models were tested in the Illinois 3-ft × 4-ft low-speed, low-turbulence wind tunnel at Reynolds numbers of 1.8×10^6 and 1.0×10^6. In addition to taking measurements on the clean model, a total of six simulated contamination cases were also tested in an extensive test matrix. These simulated contaminants included: glaze ice, rime ice, moderate leading-edge roughness, severe leading-edge roughness, localized 3D leading-edge damage, and localized 3D upper-surface damage. Steady-state lift, drag, and quarter-chord pitching moment data were taken using surface pressure taps, a traversable wake rake, and a three-component floor balance. Additionally, hinge moment measurements were taken using surface pressure measurements and a hinge balance, which was also used to acquire unsteady hinge moment data. Trends in the steady-state data, unsteady hinge moment data, and flowfield were used to identify the effects of each contamination case on the aerodynamic characteristics of the two airfoil models. A summary of $C_{l,max}$ and α_{stall} for the clean and contaminated cases are given for the NACA 3415 and NACA 23012 in Table 4.1 and Table 4.2, respectively.

Table 4.1 Summary of contamination effects on NACA 3415 at flap setting of 0° and Re = 1.8×10^6.

	$C_{l,max}$	$\Delta C_{l,max}$	α_{stall} (deg)	$\Delta\alpha_{stall}$ (deg)
Clean	1.42	---	14.4	---
Glaze	0.773	-0.65 (45.6%)	8.19	-6.5
Rime	1.14	-0.28 (19.7%)	13.3	-1
80-Grit	1.11	-0.32 (22.3%)	11.8	-2.5
14-Grit	0.976	-0.45 (31.4%)	10.7	-3.5
LE Damage	1.24	-0.18 (12.6%)	12.8	-1.5
US Damage	1.35	-0.08 (5.3%)	14.8	+0.5

Table 4.2 Summary of contamination effects on NACA 23012 at flap setting of 0° and Re = 1.8×10^6.

	$C_{l,max}$	$\Delta C_{l,max}$	α_{stall} (deg)	$\Delta\alpha_{stall}$ (deg)
Clean	1.47	---	15.9	---
Glaze	0.592	-0.88 (59.8%)	7.13	-8.5
Rime	1.04	-0.44 (29.7%)	11.8	-4.0
80-Grit	1.07	-0.40 (27.2%)	11.3	-4.5
14-Grit	0.848	-0.63 (42.4%)	9.25	-6.5
LE Damage	1.31	-0.16 (11.1%)	13.9	-2.0
US Damage	1.39	-0.09 (5.9%)	15.4	-0.5

4.1.1 Clean Airfoil Model

Since the NACA 3415 and NACA 23012 models exhibited different stalling characteristics, the unsteady hinge moment response exhibited different behaviors for both models. The NACA 3415 model experienced a trailing-edge-type stall, which was characterized by separation beginning at the trailing-edge and moving upstream as stall progresses. The resulting $C_{h,StDev}$ response showed a small, steady increase in magnitude prior to stall, and a large

increase in magnitude at stall. This indicated the possibility of sensing stall on a clean airfoil that exhibits trailing-edge-type stall.

The clean NACA 23012 exhibited a leading-edge-type stall, which was characterized by a laminar separation at the leading edge that, as the angle of attack was increased, failed to reattach to the model upper surface. While the $C_{h,StDev}$ response showed no distinct changes prior to stall, the magnitude of increase at stall was larger for the NACA 23012 model than the NACA 3415. This was attributed to the increased amount of energy in the unsteady separated wake on the NACA 23012 due to the extent of the separated region and its natural transition in the separated wake. While the $C_{h,StDev}$ response did not directly support the ability to predict stall of an airfoil, the increased unsteadiness at stall shows promise for alternative methods.

In an attempt to more accurately simulate an aircraft control surface, a trim tab was installed for a series of tests on the NACA 3415 model. The objective of this was to identify whether or not the unsteady hinge moment response was a function of trim tab deflection. Upon inspecting the resulting hinge moment measurements, it was revealed that trim tab deflection did not significantly alter the unsteady hinge moments. While the trim tab deflection did shift the steady-state hinge moment measurements by a constant magnitude, it was revealed that the hinge moment unsteadiness was unchanged with deflection of the trim tab.

4.1.2 Effect of Simulated Ice

The effects of the simulated ice contamination on the NACA 3415 and NACA 23012 were similar between the two models. The simulated glaze ice substantially reduced the maximum lift of both airfoil models (by 45%-60%) and altered the stalling characteristics of both airfoil models. Even though the stalling characteristics of the NACA 3415 and NACA 23012 were different, the presence of the simulated glaze-ice contamination created a more gradual, thin-airfoil-type stalling characteristic for both models. Additionally, the presence of the simulated glaze ice created sizable separation bubbles from the simulated ice accretion. Finally, the addition of the simulated glaze ice caused a large change in the behavior of the $C_{h,StDev}$ response. For both the NACA 3415 and the NACA 23012, the rise in $C_{h,StDev}$ began approximately 3° before the angle of attack corresponding to $C_{l,max}$.

The effect of the simulated rime ice was less severe on both airfoil models than the effects of the simulated glaze ice. The addition of the simulated rime ice reduced the maximum

lift by approximately 20%-30%. Like the simulated glaze ice, the simulated rime ice led to the formation of a small separation bubble on the ice accretion. Also like the simulated glaze ice, the presence of the simulated rime ice led to a more gradual airfoil stalling characteristic for both the NACA 3415 and the NACA 23012 models. However, the $C_{h,StDev}$ response of the simulated rime-ice case did not show the same steady increase before stall that was seen in the simulated glaze-ice case. While small increases in $C_{h,StDev}$ are visible before stall, the most substantial increases in $C_{h,StDev}$ occur after stall for the simulated rime-ice case.

4.1.3 Effect of Roughness

The effects of the two roughness contaminants were very similar between the 80-grit and the 14-grit roughness. The main difference between the results of the 80-grit and 14-grit cases was in severity. Since the 14-grit case provided a larger $(k/c)_{max}$, the resulting degradation in aerodynamic characteristics was greater, as a thicker, less-energetic turbulent boundary layer resulted from a greater roughness height.

The effects of the roughness contamination on the two airfoil models, however, were different. Instead of changing the stalling characteristics of the two airfoils to a common one, as was observed by the simulated ice contamination, the roughness contamination did not significantly change the stalling characteristics of the airfoil models. A trailing-edge-type stall was still observed for the NACA 3415 model and a leading-edge-type stall was still observed for the NACA 23012 with the presence of the roughness. This can also be observed in the $C_{h,StDev}$ responses of both models. For both models, the $C_{h,StDev}$ responses of the roughness cases appear to follow the $C_{h,StDev}$ response of the clean case, up until 1°-2° before stall where a slight increase in the slope of $C_{h,StDev}$ can be seen for the NACA 3415.

4.1.4 Effect of Simulated Damage

The effects of the 3D simulated damage cases were quite different from the 2D simulated contamination cases tested. As described previously, since the extent of the protrusions were localized to one spanwise region of the models, and since the lift and hinge moment coefficients were calculated using the entire span of the models, the simulated 3D damage cases do not appear to significantly alter the lifting characteristics of the two airfoil models. Between these

two simulated damage cases, the maximum lift coefficients were reduced by approximately 5%-13%.

Even though the lift was not significantly affected by the presence of the simulated damage, the localized regions of separation that resulted from the simulated damage configurations were observed in the $C_{h,StDev}$ response. Significant deviation of the simulated damage $C_{h,StDev}$ from the clean $C_{h,StDev}$ was observed between 1° to 5° prior to stall for the NACA 3415. Also, significant deviation of the simulated damage $C_{h,StDev}$ from the clean $C_{h,StDev}$ was observed between 6° to 7° prior to stall for the NACA 23012. Generally speaking, the simulated leading-edge damage case produced higher magnitudes of $C_{h,StDev}$ response, and the simulated upper-surface damage case produced an elevation of $C_{h,StDev}$ above the clean case over a longer angle-of-attack range.

4.2 Conclusions

1. Unsteady hinge moment was independent of trim tab deflection. The deflection of the trim tab caused small changes in C_l and C_d, and caused larger changes in C_m and C_h. However, since the large increase in $C_{h,StDev}$ at α_{stall} is caused by separated flow over the flap, deflecting the trim tab did not significantly alter the magnitude of $C_{h,StDev}$ or the angle of attack where the nonlinear increase in $C_{h,StDev}$ occurs.
2. Boundary-layer separation was the driving cause of changes in $C_{h,StDev}$. Inspection of flowfield information from C_p distribution and fluorescent-oil flow visualization, it was clear that large increases in $C_{h,StDev}$ and regions of separated flow over the flap were correlated. It was presumed that the unsteadiness associated with the separated flow led to unsteady changes in pressure over the flap, increasing the unsteadiness measured in the hinge moment.
3. The 3D simulated damage contamination cases led to small (5% to 13%) reductions in $C_{l,max}$, while still providing responses in $C_{h,StDev}$ consistent with the 2D contamination cases. The region of separated flow downstream of the simulated 3D damage caused elevated levels in $C_{h,StDev}$, while the regions outside of the wake of the simulated damage were not significantly affected by the protuberances, allowing for minimal changes in the lifting characteristics of the model.

4. The $C_{h,StDev}$ response of an airfoil was dependent on its stall type. Airfoils that exhibited trailing-edge-type stalls had a $C_{h,StDev}$ that increased with angle of attack prior to stall more gradually than that of airfoils that exhibited leading-edge-type stalls.
5. The hinge moment was sensitive to separated flows. This was shown by correlating regions of separation over the flap of both airfoil models, determined from C_p distribution or fluorescent-oil flow visualization, with increases in $C_{h,StDev}$. Thus, it may be feasible to predict separation using the unsteadiness of hinge moment measurements.[32]

4.3 Recommendations

In order to expand upon the work performed in this study, recommendations are given based upon some of the results observed in this study.

1. In order to better understand the effects of a localized contaminant, much like the 3D simulated damage cases presented here, a test should be completed in a 3D environment. This would include the use of a wing with multiple control surfaces.
2. Additional airfoil models should be tested and their hinge moments measured. Thus the stalling characteristics of the leading-edge and trailing-edge stall types could be compared to one with thin-airfoil-type stalling characteristics.
3. Roughness should be added to the simulated glaze-ice shape or the simulated damage hemispheres, and the effect on the unsteadiness in the hinge moment measured. While this may not significantly change the lifting characteristics of a model, the induced transition due to the roughness could change the $C_{h,StDev}$ response.
4. Additional shapes and contamination configurations should be tested, broadening the scope of contaminants ever further.
5. Simulated ice shapes and simulated damage hemispheres should have pressure taps that align with those on the model in order to allow for smooth, undistorted C_p data to be measured.
6. High-sensitivity, miniature pressure transducers should be used to obtain unsteady pressure data. These data could be used to correlate convection of large vortical structures downstream with $C_{h,StDev}$, relate flow separation upstream to $C_{h,StDev}$, and

provide the ability to perform frequency analysis with little interference from structural frequency modes.

Appendix A

Uncertainty Analysis

Since no experimental investigation is without error, an uncertainty analysis was performed in order to estimate the potential error present in this investigation. While this analysis did not provide the absolute error present in this experiment, it did provide a good approximation for the uncertainty of the data obtained. In an effort to avoid unnecessary complications, some equations used to determine the uncertainty of the data were simplified. This did not significantly alter the resulting outcome of uncertainty. In this study, the uncertainties were calculated using the second-power equation found in Kline and McClintock[33], which was further outlined in Coleman and Steel.[34] These equations used to determine the uncertainty of the data did not take into account the uncertainties associated with the wind tunnel corrections outlined in Section 2.1.8.

In order to calculate the uncertainty of a general result (R), it was first assumed that R is a function of several measured values ($x_1, x_2, x_3, \ldots, x_n$), as seen in Eq. A.1. The resulting experimental uncertainty of R (U_R) can be expressed by Eq. A.2.

$$R = R(x_1, x_2, x_3, \ldots, x_n) \tag{A.1}$$

$$U_R = \sqrt{\left(\frac{\partial R}{\partial x_1}U_{x_1}\right)^2 + \left(\frac{\partial R}{\partial x_2}U_{x_2}\right)^2 + \left(\frac{\partial R}{\partial x_3}U_{x_3}\right)^2 + \ldots + \left(\frac{\partial R}{\partial x_n}U_{x_n}\right)^2} \tag{A.2}$$

An alternative expression of Eq. A.1 for R is provided in Eq. A.3. In this equation, k is a constant, and exponents (a, b, c, …) can be either positive or negative. By applying this alternative relation, Eq. A.2 becomes Eq. A.4.

$$R = kx_1^a x_2^b x_3^c \ldots \tag{A.3}$$

$$\frac{U_r}{R} = \sqrt{a^2\left(\frac{U_{x_1}}{x_1}\right)^2 + b^2\left(\frac{U_{x_2}}{x_2}\right)^2 + c^2\left(\frac{U_{x_3}}{x_3}\right)^2 + \ldots} \tag{A.4}$$

When multiple uncertainties needed to be combined in order to form a single uncertainty result, the root-sum-square (RSS) method was employed. The RSS uncertainty ($U_{x,RSS}$) was calculated using the equation,

$$U_{x,RSS} = \sqrt{\left(x_1^2 + x_2^2 + x_3^2 + \ldots + x_n^2\right)} \tag{A.5}$$

A summary of uncertainties of the calculated performance characteristics used in this study can be found in Section A.5.

A.1 Force Balance Uncertainty

The performance coefficients obtained from the three-component balance measurements were calculated using Eqs. 2.11, 2.12, and 2.13, as noted in Section 2.1.4. Placing the variables from these three equations in the form of Eq. A.4, the results were Eqs. A.6, A.7, and A.8.

$$\frac{U_{C_l}}{C_l} = \sqrt{\left(\frac{U_L}{L}\right)^2 + \left(\frac{U_{q_\infty}}{q_\infty}\right)^2 + \left(\frac{U_b}{b}\right)^2 + \left(\frac{U_c}{c}\right)^2} \tag{A.6}$$

$$\frac{U_{C_d}}{C_d} = \sqrt{\left(\frac{U_D}{D}\right)^2 + \left(\frac{U_{q_\infty}}{q_\infty}\right)^2 + \left(\frac{U_b}{b}\right)^2 + \left(\frac{U_c}{c}\right)^2} \tag{A.7}$$

$$\frac{U_{C_m}}{C_m} = \sqrt{\left(\frac{U_{M_{c/4}}}{M_{c/4}}\right)^2 + \left(\frac{U_{q_\infty}}{q_\infty}\right)^2 + \left(\frac{U_b}{b}\right)^2 + 4\left(\frac{U_c}{c}\right)^2} \tag{A.8}$$

Before solving these three equations, it was necessary to first calculate the uncertainties for the lift, drag, and quarter-chord pitching moment. The variables from Eqs. 2.8, 2.9, and 2.10 were put into the form of Eq. A.2. This resulted in the uncertainties for lift, drag, and quarter-chord pitching moment, calculated in Eqs. A.9, A.10, and A.11, respectively.

$$U_L = \sqrt{\left(U_{F_N}\cos\alpha\right)^2 + \left(-U_{F_A}\sin\alpha\right)^2 + \left(-DU_\infty\right)^2} \tag{A.9}$$

$$U_D = \sqrt{\left(U_{F_N}\sin\alpha\right)^2 + \left(U_{F_A}\cos\alpha\right)^2 + \left(LU_\infty\right)^2} \tag{A.10}$$

$$U_{M_{c/4}} = \sqrt{U_M^2 + \left(x_{offset}U_{F_N}\right)^2 + \left(y_{offset}U_{F_A}\right)^2 + \left(-F_N U_{x_{offset}}\right)^2 + \left(F_A U_{y_{offset}}\right)^2} \tag{A.11}$$

The values of the axial force, normal force, and pitching moment uncertainties of the three-component balance were provided by the manufacturer, being 0.02%, 0.03%, and 0.15%, respectively, of the full-scale value. The resulting absolute uncertainty values of the axial force, normal force, and moment for the balance were 0.09 lbs, 0.027 lbs, and 0.0675 ft-lbs, respectively. Additionally, the angle of attack could be determined to within 0.02 degrees and it was assumed that the chord and span could be measured to within 0.02-inch uncertainty. q_∞ was measured using the PSI system.

A.2 Flap Hinge Balance Uncertainty

The uncertainty of the hinge balance was calculated in a very similar fashion to those of the three-component balance. The variables from Eq. 2.16 from Section 2.1.5 were substituted into Eq. A.4. This led to an equation for relative uncertainty of the hinge moment coefficient of,

$$\frac{U_{C_h}}{C_h} = \sqrt{\left(\frac{U_H}{H}\right)^2 + \left(\frac{U_{q_\infty}}{q_\infty}\right)^2 + \left(\frac{U_b}{b}\right)^2 + 4\left(\frac{U_{c_f}}{c_f}\right)^2} \tag{A.12}$$

Uncertainty in the hinge moment (U_H) was caused by both the operating uncertainty as well as the calibration uncertainty,

$$\frac{U_H}{H} = \sqrt{\left(\frac{U_{H_{Oper}}}{H_{Oper}}\right)^2 + \left(\frac{U_{H_{Cal}}}{H_{Cal}}\right)^2} \tag{A.13}$$

The load cell relative uncertainty ($U_{F,LC}/F_{LC}$) was provided by the manufacturer as 0.15% of the full-scale value. Since the full-scale force measured by the load cell was 50 lbs, the resulting absolute uncertainty of the load cell was 0.075 lbs. The resulting operating uncertainty was calculated as,

$$\frac{U_{H_{Oper}}}{H_{Oper}} = \sqrt{\left(\frac{U_{F_{LC}}}{F_{LC}}\right)^2 + \left(\frac{U_{d_h}}{d_h}\right)^2} \tag{A.14}$$

It was assumed that the moment arm from the flap spar to the load cell could be measured to within 0.02 inches. Since the length of the clamp arm was 2.97 inches, this resulted in a relative uncertainty for d_h of 0.67%.

The hinge moment calibration uncertainty was determined by incorporating the uncertainties associated with the weight applied during calibration and the moment arm distance,

$$\frac{U_{H_{cal}}}{H_{Cal}} = \sqrt{\left(\frac{U_{F_h}}{F_h}\right)^2 + \left(\frac{U_{d_h}}{d_h}\right)^2} \tag{A.15}$$

The calibration hinge moment arm was 6.875 inches and was assumed to be measured to within 0.02 inches, leading to a relative uncertainty of 0.29%. The force supplied by the weights was determined by placing the weights on a scale system comprised of an Ohaus Defender base plate and an Ohaus CD11 indicator. The scale system was able to measure the force applied by the weights within ± 0.005 lbs. Using this method, it was determined that all of the weights supplied forces of their prescribed values ± 0.005 lbs. Thus, the total relative uncertainty of the forces used in the calibration was calculated using,

$$\frac{U_{F_h}}{F_h} = \sqrt{\left(\frac{U_{F_1}}{F_1}\right)^2 + \left(\frac{U_{F_2}}{F_2}\right)^2 + \left(\frac{U_{F_3}}{F_3}\right)^2 + \left(\frac{U_{F_4}}{F_4}\right)^2} \tag{A.16}$$

The uncertainty of $F_{1,\ldots,4}$ was 0.005, and F_1, F_2, F_3, and F_4 were 5 lbs, 10 lbs, 15 lbs, and 20 lbs, respectively.

A.3 Pressure System Uncertainty

The uncertainty of the pressure measurement system derived from two main sources. The first uncertainty was associated with the conversion of the pneumatic pressures into analog signals. These uncertainties were dependent on the ESP unit's properties, and were provided by the manufacturer. The ± 5.0 psid unit had an accuracy of 0.07% the full-scale value, leading to an absolute uncertainty of ± 0.0035 psid. The ± 1.0 psid and ± 0.35 psid units had accuracies of 0.1% the full-scale value, leading to absolute uncertainties of ± 0.001 psid and ± 0.00035 psid, respectively.

The other uncertainty was associated with the calibration of the pressure system. These calibrations were used to determine coefficients used to convert analog signals from the PSI system to measured pressure values. The calibration uncertainty was dependent on the PCU used to calibrate the ESP unit. The 5.0 psid PCU was used for the ± 5.0 psid ESP unit and the ± 1.0 psid ESP units, and the 1.0 psid PCU was used for the ± 0.35 ESP units. Both PCUs had accuracies of 0.02% of full-scale, leading to absolute uncertainties of ± 0.001 psid associated with the 5.0 psid PCU, and ± 0.0002 psid associated with the 1.0 psid PCU. Since q_∞ was measured using a ± 1.0 psid ESP unit, the uncertainty associated with q_∞ was the total uncertainty of the ± 1.0 psid ESP unit. A summary of the uncertainties of the ESP units can be found in Table A.1.

Table A.1 ESP Unit Uncertainty.

ESP UNIT	UNIT UNCERTAINTY	CALIBRATION UNCERTAINTY	TOTAL UNCERTAINTY
± 5.0	± 0.0035	± 0.0010	± 0.0036
± 1.0	± 0.0010	± 0.0010	± 0.0014
± 0.35	± 0.00035	± 0.0002	± 0.0004

Using the Eqs. 2.32, 2.33, and 2.34 from Section 2.1.6 and the relation in Eq. A.2, the uncertainties for the lift coefficient, quarter-chord pitching moment coefficient, and hinge moment coefficient can be expressed as Eqs. A.17, A.18, and A.19, respectively.

$$U_{C_l} = \sqrt{\left(\frac{\partial C_l}{\partial L'} U_{L'}\right)^2 + \left(\frac{\partial C_l}{\partial q_\infty} U_{q_\infty}\right)^2 + \left(\frac{\partial C_l}{\partial c} U_c\right)^2} \tag{A.17}$$

$$U_{C_m} = \sqrt{\left(\frac{\partial C_m}{\partial M'_{c/4}} U_{M'_{c/4}}\right)^2 + \left(\frac{\partial C_m}{\partial q_\infty} U_{q_\infty}\right)^2 + \left(\frac{\partial C_m}{\partial c} U_c\right)^2} \tag{A.18}$$

$$U_{C_h} = \sqrt{\left(\frac{\partial C_h}{\partial H'} U_{H'}\right)^2 + \left(\frac{\partial C_h}{\partial q_\infty} U_{q_\infty}\right)^2 + \left(\frac{\partial C_h}{\partial c_f} U_{c_f}\right)^2} \tag{A.19}$$

In order to calculate the lift uncertainty, the lift per unit span was split up into its normal and axial components. By combining and expanding Eqs. 2.25 and 2.26, the expressions for the normal force per unit span and axial force per unit span were calculated using Eqs. A.20 and A.21, respectively.

$$F_{N'} = \frac{1}{2}\left[P_1(x_2 - x_1) + \sum_{i=2}^{n-1} P_i(x_{i+1} - x_{i-1}) + P_n(x_n - x_{n-1})\right] \tag{A.20}$$

$$F_{A'} = \frac{1}{2}\left[P_1(y_2 - y_1) + \sum_{i=2}^{n-1} P_i(y_{i+1} - y_{i-1}) + P_n(y_n - y_{n-1})\right] \tag{A.21}$$

Using these full forms of normal force per unit span and axial force per unit span and substituting them into Eq. 2.27, a full form of lift per unit span resulted,

$$\begin{aligned} L' = {} & \frac{1}{2}\cos\alpha\left[P_1(x_2 - x_1) + \sum_{i=2}^{n-1} P_i(x_{i+1} - x_{i-1}) + P_n(x_n - x_{n-1})\right] \\ & - \frac{1}{2}\sin\alpha\left[P_1(y_2 - y_1) + \sum_{i=2}^{n-1} P_i(y_{i+1} - y_{i-1}) + P_n(y_n - y_{n-1})\right] \end{aligned} \tag{A.22}$$

Using this equation, the uncertainty of lift per unit span for the pressure measurements was,

$$U_{L'} = \sqrt{\left(\frac{\partial L'}{\partial \alpha} U_\alpha\right)^2 + \sum_{i=1}^{n}\left(\frac{\partial L'}{\partial P_i} U_{P_i}\right)^2} \tag{A.23}$$

Taking the partial derivative with respect to angle of attack of Eq. A.22 resulted in Eq. A.24, and the partial derivative with respect to pressure of Eq. A.22 resulted in Eq. A.25.

$$\frac{\partial L'}{\partial \alpha} = -\frac{1}{2}\sin\alpha\left[P_1(x_2 - x_1) + \sum_{i=2}^{n-1} P_i(x_{i+1} - x_{i-1}) + P_n(x_n - x_{n-1})\right] - \frac{1}{2}\cos\alpha\left[P_1(y_2 - y_1) + \sum_{i=2}^{n-1} P_i(y_{i+1} - y_{i-1}) + P_n(y_n - y_{n-1})\right] \tag{A.24}$$

$$\begin{aligned}
\frac{\partial L'}{\partial p_1} &= \frac{1}{2}\cos\alpha(x_2 - x_1) - \frac{1}{2}\sin\alpha(y_1 - y_2) \\
\frac{\partial L'}{\partial p_i} &= \frac{1}{2}\cos\alpha(x_{i+1} - x_{i-1}) - \frac{1}{2}\sin\alpha(y_{i-1} - y_{i+1}); \quad i = 2, n-1 \\
\frac{\partial L'}{\partial p_n} &= \frac{1}{2}\cos\alpha(x_N - x_{N-1}) - \frac{1}{2}\sin\alpha(y_{n-1} - y_n)
\end{aligned} \tag{A.25}$$

Much like the equation for lift per unit span, Eq. 2.29, which corresponds to the quarter-chord pitching moment per unit span, could be expanded using Eqs. 2.23 and 2.24,

$$\begin{aligned}
M'_{c/4} = \frac{1}{4}\Big[&P_1(x_1^2 - x_2^2 - 2x_1x_{c/4} + 2x_2x_{c/4} + y_1^2 - y_2^2) \\
&+ \sum_{i=2}^{n-1}\Big[P_i(x_{i-1}^2 - x_{i+1}^2 - 2x_{i-1}x_{c/4} + 2x_{i+1}x_{c/4} + y_{i-1}^2 - y_{i+1}^2)\Big] \\
&+ P_n(x_{n-1}^2 - x_n^2 - 2x_{n-1}x_{c/4} + 2x_nx_{c/4} + y_{n-1}^2 - y_n^2)\Big]
\end{aligned} \tag{A.26}$$

This resulted in an uncertainty calculation for the quarter-chord pitching moment per unit span,

$$U_{M'_{c/4}} = \sqrt{\sum_{i=1}^{n}\left(\frac{\partial M'_{c/4}}{\partial P_i}U_{P_i}\right)^2} \tag{A.27}$$

The expanded form of hinge moment per unit span was calculated in the same fashion as the quarter-chord pitching moment per unit span calculation in Eq. A.26. By using the expression for hinge moment per unit span in Eq. 2.31 and expanding according to Eqs. 2.23 and 2.24, the expanded expression for hinge moment per unit span became,

$$
\begin{aligned}
H' = \frac{1}{4}\Big[& P_1(x_1^2 - x_2^2 - 2x_1x_h + 2x_2x_h + y_1^2 - y_2^2 - 2y_1y_h + 2y_2y_h) \\
& + \sum_{i=2}^{n_{flap}-1}\Big[P_i\left(x_{i-1}^2 - x_{i+1}^2 - 2x_{i-1}x_h + 2x_{i+1}x_h + y_{i-1}^2 - y_{i+1}^2 - 2y_{i-1}y_h + 2y_{i+1}y_h\right)\Big] \\
& + P_{n_{flap}}(x_{n_{flap}-1}^2 - x_{n_{flap}}^2 - 2x_{n_{flap}-1}x_h + 2x_{n_{flap}}x_h + y_{n_{flap}-1}^2 - y_{n_{flap}}^2 - 2y_{n_{flap}-1}y_h \\
& + 2y_{n_{flap}}y_h)\Big]
\end{aligned}
\tag{A.28}
$$

This resulted in an uncertainty for the hinge moment per unit span as,

$$
U_{H'} = \sqrt{\sum_{i=1}^{n_{flap}}\left(\frac{\partial H'}{\partial P_i}U_{P_i}\right)^2}
\tag{A.29}
$$

A.4 Wake Drag Uncertainty

An expanded form for the wake drag per unit span was calculated by combining Eqs. 2.45 and 2.46,

$$
\begin{aligned}
D' = \sum_{i=1}^{n_{rake}}\Big[& \sqrt{q_\infty^2 - q_\infty(P_{0,\infty} - P_{0,w_i})} + \sqrt{q_\infty^2 - q_\infty(P_{0,\infty} - P_{0,w_{i+1}})} \\
& - 2q_\infty + 2P_{0,\infty} - P_{0,w_i} - P_{0,w_{i+1}}\Big](y_{i+1} - y_i)
\end{aligned}
\tag{A.30}
$$

In order to obtain the wake drag coefficient, Eq. A.30 was simply nondimensionalized by dividing the wake drag per unit span by q_∞ and c,

$$
\begin{aligned}
C_d = \frac{1}{q_\infty c}\sum_{i=1}^{n_{rake}}\Big[& \sqrt{q_\infty^2 - q_\infty(P_{0,\infty} - P_{0,w_i})} + \sqrt{q_\infty^2 - q_\infty(P_{0,\infty} - P_{0,w_{i+1}})} \\
& - 2q_\infty + 2P_{0,\infty} - P_{0,w_i} - P_{0,w_{i+1}}\Big](y_{i+1} - y_i)
\end{aligned}
\tag{A.31}
$$

Since the measured pressures used in Eq. A.31 were all referenced to P_{atm}, the quantity ($2P_{0,\infty} - P_{0,w(i)} - P_{0,w(i+1)}$) could be calculated directly using measured values,

$$
2P_{0,\infty} - P_{0,w_i} - P_{0,w_{i+1}} = 2\left(P_{0,\infty} - P_{atm}\right) - \left(P_{0,w_i} - P_{atm}\right) - \left(P_{0,w_{i+1}} - P_{atm}\right)
\tag{A.32}
$$

Thus, the uncertainty in drag coefficient obtained from the wake survey system was defined as,

$$U_{C_d} = \sqrt{\left(\frac{\partial C_d}{\partial c}U_c\right)^2 + \left(\frac{\partial C_d}{\partial q_\infty}U_{q_\infty}\right)^2 + \left(\frac{\partial C_d}{\partial P_{0,\infty}}U_{P_{0,\infty}}\right)^2 + \sum_{i=1}^{n_{rake-1}}\left(\frac{\partial C_d}{\partial P_{0,w(i)}}U_{P_{0,w_i}}\right)^2} \quad \text{(A.33)}$$

Taking the partial derivatives of Eq. A.31 with respect to c, q_∞, $P_{0,\infty}$, and $P_{0,w(i)}$ results in Eqs. A.34, A.35, A.36, and A.37. These four partial derivatives can be substituted into Eq. A.33 to solve for the uncertainty of the drag coefficient.

$$\frac{\partial C_d}{\partial c} = -\frac{1}{q_\infty c^2}\sum_{i=1}^{n_{rake}}\left[\sqrt{q_\infty^2 - q_\infty(P_{0,\infty} - P_{0,w_i})} + \sqrt{q_\infty^2 - q_\infty(P_{0,\infty} - P_{0,w_{i+1}})} - 2q_\infty + 2P_{0,\infty} - P_{0,w_i} - P_{0,w_{i+1}}\right](y_{i+1} - y_i) \quad \text{(A.34)}$$

$$\frac{\partial C_d}{\partial q_\infty} = -\frac{1}{q_\infty^2 c}\sum_{i=1}^{n_{rake}}\left[\sqrt{q_\infty^2 - q_\infty(P_{0,\infty} - P_{0,w_i})} + \sqrt{q_\infty^2 - q_\infty(P_{0,\infty} - P_{0,w_{i+1}})} - 2q_\infty + 2P_{0,\infty} - P_{0,w_i} - P_{0,w_{i+1}}\right](y_{i+1} - y_i) + \frac{1}{q_\infty c}\sum_{i=1}^{n_{rake}}\left[\frac{2q_\infty - \left(P_{0,\infty} - P_{0,w_i}\right)}{2\sqrt{q_\infty^2 - q_\infty\left(P_{0,\infty} - P_{0,w_i}\right)}} + \frac{2q_\infty - \left(P_{0,\infty} - P_{0,w_{+1i}}\right)}{2\sqrt{q_\infty^2 - q_\infty\left(P_{0,\infty} - P_{0,w_{i+1}}\right)}}\right](y_{i+1} - y_i) \quad \text{(A.35)}$$

$$\frac{\partial C_d}{\partial P_{0,\infty}} = \frac{1}{q_\infty c}\sum_{i=1}^{n_{rake}}\left[2 - \frac{q_\infty}{2\sqrt{q_\infty^2 - q_\infty\left(P_{0,\infty} - P_{0,w_i}\right)}} - \frac{q_\infty}{2\sqrt{q_\infty^2 - q_\infty\left(P_{0,\infty} - P_{0,w_{i+1}}\right)}}\right](y_{i+1} - y_i) \quad \text{(A.36)}$$

$$\frac{\partial C_d}{\partial P_{0,w_i}} = \frac{1}{q_\infty c}\left[\frac{q_\infty}{2\sqrt{q_\infty^2 - q_\infty\left(P_{0,\infty} - P_{0,w_i}\right)}} - 1\right](y_{i+1} - y_i) \quad \text{(A.37)}$$

A.5 Sample Uncertainties

Sample uncertainties are provided in Table A.2 and Table A.3. These uncertainties were evaluated for the NACA 3415 with glaze-ice case at Re = 1.8×10^6 with $\delta_f = 0°$ and $\alpha = 5°$. This case was selected because it provided one of the highest sets of uncertainty estimates of all the tests run, representing worst-case results.

Table A.2 Balance performance coefficient uncertainties.

COEFFICIENT	MEASURED VALUE	ABSOLUTE UNCERTAINTY	RELATIVE UNCERTAINTY (%)
C_l	0.6721	± 0.003179	0.47
C_d	0.0491	± 0.000359	0.73
C_m	-0.0231	± 0.000322	1.39
C_h	-0.0354	± 0.000548	1.55

Table A.3 Pressure system performance coefficient uncertainties.

COEFFICIENT	MEASURED VALUE	ABSOLUTE UNCERTAINTY	RELATIVE UNCERTAINTY (%)
C_l	0.6437	± 0.001662	0.26
C_d	0.0443	± 0.000561	1.27
C_m	-0.0243	± 0.000478	1.97
C_h	-0.0369	± 0.001070	2.90

References

[1] National Transportation Safety Board. 2009. *U.S. Air Carrier Operations, Calendar Year 2005*. Annual Review of Aircraft Accident Data NTSB/ARC-09/01. Washington, DC.

[2] National Transportation Safety Board. 2009. *Annual Review of General Aviation Accident Data 2005*. Publication Type NTSB/ARG-09/01. Washington, DC.

[3] National Aeronautics ans Space Administration. 2008. "Aircraft Icing Training," NASA Glenn Research Center.

[4] Lynch, F.T., Khodadoust, A., "Effects of Ice Accretions on Aircraft Aerodynamics," *Progress in Aerospace Sciences*, Vol. 37, No. 8, 2001, pp. 669-767.

[5] Bragg, M.B., Broeren, A.P., Blumenthal, L., "Iced-Airfoil Aerodynamics," *Progress in Aerospace Sciences*, Vol. 41, No. 5, 2005, pp. 323-362.

[6] Busch, G.T., Broeren, A.P., and Bragg M.B., "Aerodynamic Simulation of a Horn-ice Accretion on a Subscale Model," AIAA-2007-0087, *45th AIAA Aerospace Sciences Meeting and Exhibit,* Reno, NV, Jan. 2007.

[7] Luers, J. and Haines, P., "Heavy Rain Influence on Airplane Accidents," *AIAA Journal of Aircraft,* Vol. 20, No. 2, 1983, pp. 187-191.

[8] Shah, G.H., "Aerodynamic Effects and Modeling of Damage to Transport Aircraft," AIAA-2008-6203, *AIAA Atmospheric Flight Mechanics Conference and Exhibit,* Honolulu, HI, Aug. 2008.

[9] Gormley, M., "Looking at Lift With SW Plus," *Business and Commercial Aviation*, January 1993.

[10] "New System Offers Real Time Aerodynamic Performance Monitoring," *Air Safety Week*. March 1999.

[11] Gurbacki, H.M. and Bragg, M.B., "Sensing Aircraft Effects by Flap Hinge Moment Measurements," AIAA-99-3149, *17th Applied Aerodynamics Conference,* Norfolk, VA, Jun. 1999.

[12] "Aircraft Surface Contamination Sensing System Using Control Surface Hinge Moment Measurements," M.B. Bragg and H. M. Gurbacki, patent # 6,140,942, October 31, 2000.

[13] Trunov, O.K. and Ingelman-Sundberg, M., "On the Problem of Horizontal Tail Stall Due to Ice," The Swedish-Soviet Working Group on Scientific-Technical Cooperation in the Field of Flight Safety, Report No. JR-3, 1985.

[14] National Transportation Safety Board. 22 October 1996. *Probable Cause, Regist. Number N401AM*. National Transportation Safety Board Aviation Accident Database and Synopses. Washington, DC.

[15] Anderson, J.D., *Introduction to Flight*. McGraw-Hill Book Company, New York, 2007.

[16] Jones, B. M., "Measurement of Profile Drag by the Pitot-Traverse Method," Tech. Rep. 1688, British Aeronautical Research Council Reports & Memoranda, 1936.

[17] Schlichting, H., *Boundary-Layer Theory*, McGraw-Hill Book Company, New York, 1979.

[18] Lee, S., "Effects of Supercooled Large Droplet Icing on Airfoil Aerodynamics," Ph.D. Dissertation, University of Illinois at Urbana-Champaign, 2001.

[19] Barlow, J. B., W.H. Rae, J., and Pope, A., *Low-Speed Wind Tunnel Testing*, John Wiley & Sons, Inc., NY, 3rd ed., 1999.

[20] Whalen, E.A., Broeren, A.P., and Bragg M.B., "Aerodynamics of Scaled Runback Ice Accretions," *AIAA Journal of Aircraft,* Vol. 45, No. 3, 2008, pp. 591-603.

[21] Lee, S., Bragg M.B., "Experimental Investigation of Simulated Large-Droplet Ice Shapes on Airfoil Aerodynamics," *AIAA Journal of Aircraft,* Vol. 36, No. 5, 1999, pp. 844-855.

[22] Broeren, A.P., Bragg, M.B. et al., "Effect of High-Fidelity Ice Accretion Simulations on the Performance of a Full-Scale Airfoil Model," AIAA-2008-434, *46th AIAA Aerospace Sciences Meeting and Exhibit,* Reno, NV, Jan. 2008.

[23] Busch, G.T., Broeren, A.P., and Bragg, M.B., "Aerodynamic Fidelity of Sub-scale Two-Dimensional Ice Accretion Simulations," AIAA-2008-7062, *26th AIAA Applied Aerodynamics Conference,* Honolulu, HI, Aug. 2008.

[24] Broeren, A.P. and Bragg, M.B., "Effect of Airfoil Geometry on Performance with Simulated Intercycle Ice Accretions," *AIAA Journal of Aircraft*, Vol. 42, No. 1, 2005, pp. 121-130; also AIAA Paper 2003-0728, Jan. 2003.

[25] Busch, G.T., "Ice Accretion Aerodynamic Simulation on a Subscale Model," M.S. Thesis, University of Illinois at Urbana-Champaign, 2004.

[26] Jacobs, J. J., "Iced Airfoil Separation Bubble Measurements by Particle Image Velocimetry," Ph.D. Dissertation, University of Illinois at Urbana-Champaign, 2007.

[27] Alcar, M. S., and Smith, C. R., "A Study of Hairpin Vortices in a Laminar Boundary Layer," *Journal of Fluid Mechanics*, Vol. 175, 1987, pp. 1-41.

[28] Whalen, E.A., Broeren, A.P., Bragg, M.B., and Lee, S., "Characteristics of Runback Ice Accretion on Airfoils and their Aerodynamic Effects," AIAA-2005-1065, *43rd Aerospace Science Meeting and Exhibit,* Reno, NV, Jan. 2005.

[29] McCollough, G. B. and Gault, D. E., "Examples of Three Representative Types of Airfoil-Section Stall at Low Speed," NACA TN 2502, Sept. 1951.

[30] Drela, M., "XFOIL 6.96 User Primer," MIT Aero & Astro Engineering, Nov. 30, 2001.

[31] Winkler, J. F. and Bragg, M.B., "Local Flowfield About Large Distributed Roughness in the Initial Ice Accretion Process," AIAA-96-0868, *34th Aerospace Science Meeting and Exhibit,* Reno, NV, Jan. 1996.

[32] Ansell, P. J., Bragg, M. B., and Kerho, M. F., "Envelope Protection System Using Flap Hinge Moment Measurements," AIAA-2010-4225, *28th Applied Aerodynamics Conference*, Chicago, IL, June 2010.

[33] Kline, S. and McClintock, F. A., "Describing Uncertainty in Single-Sample Experiments," Mechanical Engineering, Vol. 75, 1953, pp. 3–8.

[34] Coleman, H. W. and W.G. Steel, J., Experimentation and Uncertainty Analysis for Engineers, Wiley-Interscience, NY, 1989.